Influence of magnetic fields on cathodic growth of phases in acidic sulphate and acidic copper sulphate systems

A thesis submitted to the University of Dublin, Trinity College

in application for the degree of Doctor of Philosophy

by

Dámaris Fernández Donoso

School of Physics

Trinity College Dublin

July 2011

Declaration

This thesis is submitted by the undersigned for examination for the degree Doctor of Philosophy at the University of Dublin. It has not been submitted as an exercise for a degree at any other University or other degree-giving institution.

This thesis, apart from the advice, assistance and joint effort mentioned in the acknowledgements and in the text, is entirely my own work.

I, the undersigned, agree that Trinity College Library may lend or copy this thesis upon request.

To my people, without whom this makes no sense:

Leia and Natalia, my life's Navigatoria,

Nancy, my starting point; Juan, the sparks; Gerardo, the wind.

"Miracles are perfectly accountable: we just need to simultaneously compute infinite variables."

– Siramad

Summary

Industrial processes involving copper electrolysis are important in modern society. In these processes copper ions contained in aqueous solution are crystallized onto a cathode by the passage of current. Copper industry faces several challenges regarding high power consumption, growth morphology of the final product as well as the space and time used to achieve a certain production rate, known as 'space-time yield'.

The challenges stem from limitations on the mass transport of species between the bulk solution and the reacting surface of the electrodes involved. A second cathodic process in these systems is the formation of hydrogen gas from water electrolysis. This reaction may occur as a side reaction during copper metallization at high currents. All these reasons prevent the use of high deposition rates during industrial processing.

Magnetic fields are known to enhance mass transport-limited reactions via magnetoconvective phenomena. This work allows further understanding of the influence of fields on growth of cathodic solid and gas phases from the liquid, for acidic sulphate and acidic copper sulphate systems when mass transport limitation is relevant. The interaction of gravity is considered as a source of convection as well.

The study is divided in four main sections: electrochemical characterization, growth of solid copper alone, growth of hydrogen gas alone, and finally growth of solid copper simultaneously with a gas phase transformation (involving oxygen or hydrogen gas).

For the general characterization of the electrochemical response under fields, a 3-order of magnitude copper concentration range was used. Enhanced deposition currents corresponded to the expected values.

Sources of signal instability associated with scaling of current density, related to the real reaction area were identified.

Copper growth modes were studied considering the interplay of natural and magnetoconvection. Under mass transport limitation, magnetoconvection enhances morphology changing it from dendritic to nodular but remains in 3D growth. Under mixed control, the characteristic lateral growth does not change; however convective flow shapes deposit profiles. Under activation control with aerated electrolytes, the rate of diffusion-limited oxygen reduction reaction is magnetically enhanced, in detriment of deposit coverage. Galvanostatic growth allows shifts of around 0.5 V with fields from 0.5 to 5 T. This means that power consumption can be reduced from ~2 kWh/kg to 1.4 kWh/kg of produced cathode. Associated with the overpotential shift, a change in growth mode to planar deposits is achieved. Accordingly, profile and roughness are more homogeneous with increasing fields.

The study of field influence on growth of hydrogen bubbles considered the interplay of upthrust force. The fields influence rate and direction of the evolving bubble stream depending on field intensity and direction relative to gravity. Swarms of small hydrogen bubbles were produced when Lorentz force acts perpendicular to upthrust or when Lorentz force adds to upthrust. Single hydrogen bubbles as big as 900 μm in diameter were produced when Lorentz force opposed upthrust and when Lorentz force acted azimuthally. In the latter case, secondary flow due to vortex around single bubbles stabilize them, allowing longer growth time before departure.

When hydrogen co-reduces with copper, hydrogen reaction is affected by the field in different manners depending on the system's ability to change the j/j_L ratio. For galvanostatic conditions, cell overpotential is reduced and hydrogen side reaction is inhibited.

Acknowledgements

First of all, thanks to my supervisor Professor Michael Coey, to whom I am deeply grateful for deciding to open the gates of science for me, and then bringing me forward when I did not find the way. I feel honoured for having the chance to work in this environment: Trinity College and CRANN are nice places for doing science. Here, new ideas seldom find an obstacle to be tried. Actually, the only scarce resource here is time to do more things. Second, to Professor Walther Schwarzacher, who has witnessed and friendly participated of the process all these years. Dr. Peter Dunne, Dr.Zhu Diao and Ms. Milèna Martine, who gave time and effort in parts of the experimental work of this thesis, thank to you all, I have learned a lot from you.

The Group D, with people who've been there for very long and also many others who have accompanied us for shorter periods, is just great. I like the group. People are always ready to help "right here, right now" which is a huge thing. Special mentions to Venky, Plamen and Adriele, who I met many years ago when I came here as a summer student. It is nice to be a witness of your process of forming a family and career. Karsten, the undeniable example of efficiency, who matches perfectly fine kindness and directness, thanks. Now I know that at some point I must visit your country and have a full picture of the Karstenish-way-of-life.

To my dear che Lorena, for your energy and Latin American español, a relieving back to my roots in any tiring day. To Ciaran, for your intuitive timing of things. Realising when is very important, sometimes more important than knowing what, especially in team work. To Kaan, Huseyin K. And Huseyin T., thanks for sharing knowledge and interesting stories, it's been nice realizing the many things in common between our cultures. Thanks to Jiafeng, such a nice person, HongXu,

YongChang and all the Chinese guys , your bodily politeness remains still a pleasurable puzzle to me.

The Intel gang, lead by Chris, Peter and Gavin, embodying such nice Hi-Tech & organizational culture background, you guys certainly are "INTEL-inside" walking icons. For the newer, Kaan and Remy, transformation is happening, we can tell; soon you'll go ♬dum-dum-dum-dum♬, surely! It's nice to work nearby and learn from you.

Mike Finneran, Des Keany, John Kelly, what would we do without you?! Thanks for, besides doing great-great work, spreading always fun.

Special thanks to Chris and Claudia Murray, for their crucial presence during all this process. From professional to business to friendship to neighbours to family, you cover the entire spectrum with sterling performance. You deserve all the best. I wish long-lasting, deep happiness for you and your kids.

Finally, deep thanks to all the people who, with perspective or not, decided to play a challenging role. A mountain climber needs training walls. Thanks for displaying such energy into it. And double thanks to those who after a while decided it was time to facilitate, for such change of mind requires admirable braveness.

Table of Contents

I. Introduction and literature overview **1**

I.1 Motivation 1

I.2 Reactions occurring in industrial copper production 2

I.3 Electrochemical formation of bulk phases 4

I.4 Overpotential – current relationship 10

I.5 Current distribution, mass transport and the role of convection 14

I.6 Magnetohydrodynamics and electrochemistry 19

I.6.1 Field effect on the electrochemical response 20

I.6.2 Field effect on phase growth 21

I.6.2.1 Solid phase: Copper 21

I.6.2.2 Gas phase: Hydrogen 21

I.6.2.3 Growth of solid in presence of gas phases 22

I.7 Overview of the following chapters 24

II. Experimental methods **25**

II.1 Magnetic and electrochemical devices 26

II.1.1 Magnetoelectrochemical cell 26

II.1.2 Electrochemical devices 29

II.1.3 Magnetic devices 32

II.2 Characterization techniques 35

III. Magnetic field effect on the electrochemical response **45**

III.1 Effect of concentration and field intensity 46

III.2 Effect of gravity 52

III.3 Effect of electrode area 53

III.4 Discussion and summary 60

IV. Magnetic field effect on growth of metallic copper **62**

IV.1 Deposition under potentiostatic control 63
IV.1.1 Mixed control conditions 63
IV.1.2 Diffusion control conditions 70
IV.2 Deposition under galvanostatic control 77
IV.3 Discussion and summary 83

V. Magnetic field effect on growth of Hydrogen bubbles **85**

V.1 Electrochemical investigation of gas evolving electrodes 86
V.1.1 Fluctuations of the measured signal 87
V.1.1.1 General aspects 87
V.1.1.2 Noise modulation with electrode size 90
V.1.1.3 Formation of single bubbles 92
V.1.1.4 Waveform and stages of bubble growth 96
V.1.2 Electrochemical noise analysis and structure of power spectra density 103
V.1.3 Summary 107
V.2 Physicochemical conditions and bubble size 109
V.2.1 Substrate nature 109
V.2.2 Concentration of surfactant sodium dodecyl sulphate, SDS 111
V.2.3 Ionic strength 114
V.2.4 Concentration of Ethylene Glycol, EG. 117
V.2.5 Summary 121
V.3 Magnetic field effect on growth of single hydrogen bubbles 124
V.3.1 Lorentz and upthrust forces 124

V.3.2 Lorentz force acting horizontally 126
V.3.3 Lorentz force acting vertically 131
V.3.4 Lorentz force acting azimuthally 134
V.3.5 Summary 143
V.4 Discussion and summary of the chapter 144

VI. Magnetic field effect on growth of metallic copper with secondary gas phase reaction 150
VI.1 Copper and dissolved oxygen 151
VI.2 Copper and hydrogen 157
VI.2.1 Cu-H co-reduction under no field 157
VI.2.2 Cu-H co-reduction under magnetic fields 160
VI.2.2.1 System forced to maintain $j/j_L > 1$ 160
VI.2.2.2 System allowed to change the j/j_L ratio 166
VI.3 Summary 172

VII. Conclusions and further work 174
VI.1 Conclusions 174
VI.2 Further work 177

VIII. References 179

List of figures

Chapter I

Figure 1.1: Scheme of an electrolytic cell showing the product species at the cathode and anode for the reactions involved in copper electrowinning (EW). 4

Figure 1.2: Summarized Pourbaix diagram (potential – pH) for the system Cu – H_2O at 25° C [2], where reactions relevant for copper electrolysis are highlighted. The cathodic reactions occur within the yellow area, while the anodic reactions occur within the green area. 5

Figure 1.3: (a) Free energy variation (ΔG) of a system as a result of the volume and surface energies contribution (ΔG_V and ΔG_S), indicating the critical radius r*. (b) Reduction of the critical radius r* as a function of overpotential η [7]. 7

Figure 1.4: (a) Concentration of a species being consumed at the reacting surface, as a function of distance and time, (b) linearized concentration gradient, according to Nernst, Eq. (1.6). 9

Figure 1.5: Scheme representing the overpotential – current relationship. 11

Figure 1.6: (a) Scheme showing the general case of current-potential relationship for a metallization process, showing: linear (1), exponential (2), mixed control (3) and mass transport limited (4) regions. These are related to growth modes at the right-hand side of the scheme [3]. (b) An example of polarization curves for copper electrowinning, relating current density with the corresponding cathodic and anodic overpotentials. 13

Figure 1.7: Scheme showing the relation between roughness amplitude (x) and diffusion layer thickness (δ), related to the relative limited current density on peaks and valleys. (a) Macro-roughness, (b) micro-roughness and (c) variable conditions. 17

Chapter II

Figure 2.1: Scheme of the magnetoelectrochemical cell used. 28

Figure 2.2: Scheme of (a) quartz crystal working electrode, and (b) flow in a rotating disk electrode. 31

Figure 2.3: (a) Scheme of an electromagnet. (b) Picture showing the equipment setup used in most of the experiments with horizontal fields up to 1.5 Tesla. 33

Figure 2.4: (a) Scheme of a cryocooler–cooled superconducting magnet. (b) Picture of the superconducting magnet used in this study, and the annexe equipment setup. 34

Figure 2.5: (a) Scheme of the beam interaction with a sample. (b) SEM-FIB Strata 235, one of the tools used. 37

Figure 2.6: The cantilever principle, showing the basic principle of profilometry, with detection of the sensor tip movement by: (a) capacitance measurement, and (b) laser deflection. 39

Figure 2.7: Dektak stylus profilometer used during this investigation. (a) View of the profilometry chamber, (b) view of the equipment setup, with its pneumatic optical table and controlling units. 40

Figure 2.8: (a) Scheme of the functioning principle of a scanning white light interferometer. (b) Picture of the device used. 42

Figure 2.9: High speed camera, macro lens, fiber optic light source with diffusion plate and planar backlight, used to follow the growth of bubbles. 43

Chapter III

Figure 3.1: (a) Linear sweep voltammograms showing copper deposition from acid copper sulphate electrolytes on Cu substrates at 0 T and 1.5 T. The family of curves show the effect of copper concentration on the current. (b) Field-induced enhancement of the limiting current at $\eta = 0.5$ V, as a function of electrolyte concentration, for 0.5 T and 1.5 T. 48

Figure 3.2: (a) Effect of magnetic fields up to 5 Tesla on cathodic voltammograms from a 0.3 M $CuSO_4$ electrolyte. (b) Corresponding changes in current density values as a function of field intensity and electrolyte concentration, following the power law described by the empirical relation $\Delta \boldsymbol{j}_L \propto \boldsymbol{B}^{1/3} C_0^{\,4/3}$. Fields applied from 0.5 to 5 Tesla. 50

Figure 3.3: Shifts in the absolute value of cathodic current density as a function of electrolyte concentration, for diverse overpotentials, when a field of 1.5 T is applied. 51

Figure 3.4: Effect of gravity (in terms of electrode position) on the values of the limiting current density obtained when fields up to 5 Tesla were applied vertically. 52

Figure 3.5: Changes in limiting current values as a function of electrode size and flux density. 54

Figure 3.6: (a) Current evolution over time for 0, 0.5 and 1.5 Tesla. (b) Corresponding charge passed. Electrolyte 0.3 M $CuSO_4$. 54

Figure 3.7: Cathodic linear sweep voltammograms showing the effect of convection on the measured current density for a concentrated electrolyte containing 0.5 M Cu^{2+}. The effect of gravity is considered by changing the electrode position: (a) horizontal facing up, (b) vertical, and (c) horizontal facing down. The effect of angular velocity for a rotating disk electrode is seen in (d). 56

Figure 3.8: Cyclic voltammograms performed at 2 V s^{-1} using microelectrodes of 50 μm in diameter, to show the magnetic field effect on the reactions occurring at different Cu^{2+} concentrations. Field applied is 1.3 T. 59

Chapter IV

Figure 4.1: Macrograph of samples grown potentiostatically from a 0.3 M $CuSO_4$ electrolyte, at η = -200 mV for 300 seconds, at 0 and 4 T. No evident change is observed. The electrode diameter is 0.8 cm. 64

Figure 4.2: Comparative images showing the topology analysis of the same sample, made by (a) AFM and (b) SWLI techniques. Electrolyte 0.3 M $CuSO_4$, η = -200 mV, t = 300 s. 65

Figure 4.3: Topographic characterization scanning white light interferometry of samples grown potentiostatically from a 0.3 M $CuSO_4$ electrolyte, at η = -200 mV for 300 seconds, at 0 and 1.5 T. 66

Figure 4.4: Profiles and morphology of samples grown potentiostatically from a 0.3 M $CuSO_4$ electrolyte, at η = -200 mV for 300 seconds, under magnetic fields up to 4 T. The directions of Lorentz and natural convection forces across the vertical electrode surface are sketched, and the magnetic field influence on the deposit profiles in their direction is shown. 68

Figure 4.5: SEM images showing no evident change in the growth mode when samples are obtained potentiostatically at the mixed control region, under magnetic fields, neither on the left edge (where a peak associated with Lorentz force) or on the centre of the sample. 69

Figure 4.6: Morphology observed by scanning electron microscopy, for samples potentiostatically grown from a 0.3 M $CuSO_4$ electrolyte during 300 seconds, at 0 and 4 T. Overpotentials applied correspond to the zones of diffusion, mixed and activation control (-550, -200 and -40 mV, respectively). 71

Figure 4.7: Scanning electron microscopy images showing the inhibition of dendrite formation at early growth stage, induced by magnetic field. Deposits were obtained after 25 seconds of deposition at η = -550 mV. The electrolyte used was 0.3 M $CuSO_4$. 72

Figure 4.8: Macrographs showing magnetically induced improvement on deposit morphology, including edge effects, as a function of electrolyte concentration and field intensity. The electrode diameter is 0.8 cm. Spongy, powdery deposits typical of mass transport limitation are suppressed under magnetic fields throughout the whole electrode. In particular, the edges exhibit a much compact growth. 72

Figure 4.9: Profiles and morphology of samples grown potentiostatically from a 0.3 M $CuSO_4$ electrolyte, at η = -400 mV for 300 seconds, under magnetic fields up to 4 T. The directions of Lorentz and natural convection forces across the vertical electrode surface are sketched. 74

Figure 4.10: AFM characterization showing the magnetic field induced reduction of roughness for samples grown after a 2-second potential pulse at diffusion-limited overpotential (η = -400 mV). The electrolyte used was 0.3 M $CuSO_4$. 76

Figure 4.11: Profile measurements of deposits obtained under galvanostatic control from a 0.3 M $CuSO_4$ electrolyte at vertical electrodes under vertical fields up to 5 T. The applied current is j = -60 mA cm^{-2}. Fixed time of deposition is 25 and 2500 seconds. 78

Figure 4.12: AFM images showing the effect of magnetic fields on the particle size and shape of copper deposits obtained under galvanostatic control at j = -60 mA cm^{-2} from a 0.3 M $CuSO_4$ electrolyte. Deposition times are 10, 15, 30 and 60 seconds. 79

Figure 4.13: SEM images corresponding to samples grown during 30 seconds of deposition at j = -60 mA cm^{-2} from a 0.3 M $CuSO_4$ electrolyte in different fields. A change in growth mode is seen when magnetic fields are applied. 80

Figure 4.14: Surface roughness obtained from AFM measurements at 15 seconds of deposition at j = -60 mA cm^{-2} from a 0.3 M $CuSO_4$ electrolyte. 81

Figure 4.15: Effect of magnetic fields up to 5 T on roughness for samples galvanostatically obtained control at j = -60 mA cm^{-2}, as a function of deposition time. Electrolyte: 0.3 M $CuSO_4$. 82

Figure 4.16: Overpotential shift due to magnetoconvection, when $j/j_{L\,(B=0)}$ = 1, changes to $j/j_{L\,(B\neq0)} < 1$, between 0.25 to 0.6. 82

Chapter V

Figure 5.1: Cyclic voltammetry at 0.2 V s^{-1} showing the effect of vertical magnetic fields up to 5 T when a Cu electrode of 5.4 mm in diameter is vertically immersed in a 1.2 M H_2SO_4 electrolyte. The insets show the electrode considering the direction of the current and magnetic field, as well as the Lorentz and upthrust forces. 89

Figure 5.2: Time sequences (chronoamperometry) measured potentiostatically at $\eta = -1.0$ V for a 5400 μm electrode in the conditions of figure 5.1. 89

Figure 5.3: Time sequences for hydrogen evolution at Cu microelectrode of 125 μm in diameter, potentiostatically controlled at η = -1.0 V. Electrolyte is 1.2 M H_2SO_4. 90

Figure 5.4: Characteristic information that can be extracted from overpotential oscillations during galvanostatic formation of single bubbles at gas evolving electrodes. Pt substrate, $\phi = 125$ μm, $j = 20$ A·cm^{-2}.. 91

Figure 5.5: Relation between overpotential oscillation and growth-detachment cycle of a single bubble, grown galvanostatically at $j = 10$ A·cm^{-2} over a Pt microelectrode of $\phi = 125$ μm. 93

Figure 5.6: (a) Dependence of release frequency and bubble size on current density for ranges (b) Vogt's model showing the dependence of gas efficiency on the current density, taken from [9]. 95

Figure 5.7: Overpotential fluctuation associated to the growth of a single bubble of hydrogen on a Pt microelectrode of 125 μm in diameter, facing upwards. The bubble size, oscillation amplitude and release frequency change with the applied current density j. (a) $j = 10$ A·cm^{-2}, $f = 1.8$ Hz, and (b) $j = 20$ A·cm^{-2}, $f = 1.1$ Hz. 98

Figure 5.8: Scheme relating bubble size and ohmic contribution to the overpotential oscillation. The blue areas indicate the least resistance pathway between solution and substrate. In (a) the thin gas layer is nearly-equally resistive in all its volume. In (b) only the volume near the three-phase point maintains a similar access pathway, so the reacting volume is diminished. In (c), (d) and (e) the stretching bubble refreshes solution into the three-phase point, increasing the reacting volume. 99

Figure 5.9: Shapes of overpotential oscillations in the time sequence, associated with IR contribution of the sitting bubble. In order to show how reproducible these results are, each graph shows two sets of data, corresponding to different runs in identical conditions. The maximum oscillation amplitude η_λ is related to the time of maximum coverage $t_{\theta_{max}}$. The time of detachment t_{detach} and of maximum bubble size $t_{\emptyset_{max}}$ however, not necessarily coincide with $t_{\theta_{max}}$. In (a) the bubble detaches when reaches maximum size and substrate coverage. In (b) detachment is initiated at $t_{\theta_{max}}$ but occurs later at t_{detach}, when the bubble has reached its maximum size. In (c) and (d), from the waveform shapes, it is inferred a more complex detachment process, with probably a longer stretching stage in (c) and liberation of smaller side bubbles in (d). 102

Figure 5.10: Power spectra density (PSD) for the overpotential signals taken at different applied current densities, and focusing in the range below 100 Hz, which shows relevant information. A plateau related to the IR contribution is followed by a main peak which marks the frequency of bubbles release, and a $1/f^2$ roll-off indicating a coalescence process. The plateau and main peak values are related to bubble size, and determined by current density. Higher current produce larger bubbles which produce larger ohmic resistance, observed as a higher plateau, and are released at longer $1/f$ periods. 105

Figure 5.11: Scheme of coalescing process at the inner rim of the bubble. 106

Figure 5.12: Effect of substrate materials Cu and Pt on the frequency of bubble release. Vertical ϕ = 125 mm electrodes under j = 10 A·cm^{-2}. 110

Figure 5.13: Variation of frequency of release with change of surface tension, by additions of sodium dodecyl sulphate. 112

Figure 5.14: (a) Changes of average bubble size as a function of SDS concentration. (b) Interfacial area per unit time produced in relation to the surface tension of the solution. (c) Corresponding gas/liquid surface tension. 113

Figure 5.15: Changes of average bubble size for electrolytes of different composition. The average size of bubbles and the corresponding interfacial area produced per time unit is plotted as a function of the ionic strength of each electrolyte, according to Table 5.1. The associated properties of surface tension and conductivity are also plotted. Clearly, conductivity has little or no effect on bubble size compared to surface tension. 116

Figure 5.16: Transition from evolution of single-bubbles to streams by addition of ethylene glycol to the electrolyte. 119

Figure 5.17: Changes in bubble formation due to additions of ethylene glycol (EG). The upper panels show the changes in average bubble size and interfacial area produced per unit time as a function of EG concentration. The lower panels show the corresponding gas/liquid surface tension and viscosity. 120

Figure 5.18: Chart showing the degree of bubble coalescence in relation to surface tension values, for different compositions of the electrolyte. The ionic strength, content of ethylene glycol and sodium dodecyl sulfate were considered, and are aligned in relation to their corresponding values of interfacial tension. 123

Figure 5.19: Possible position combinations of magnetic field and electrode surface for freely-evolving bubbles. 125

Figure 5.20: The field effect on overpotential oscillations indicating reduction of bubble size for the configuration $B_H \parallel S_H$. Pt microelectrode, 1.2 M H_2SO_4 electrolyte. 127

Figure 5.21: Reduction of bubble size by effect of a magnetic field in configuration $B_H \parallel S_H$, same as in Figure 5.20. This effect is independent of field polarity. 127

Figure 5.22: Transition from periodic single bubbling to aperiodic regime in the $B_V \parallel S_V$ configuration. A copper 125 μm microelectrode was maintained at j = 3.5 A cm^{-2}. Periodicity of bubbles release is found up to 1.5 T; at 3 and 4 T small streams of bubbles evolve, with sporadic release of one big bubble. At 5 T only streams of small bubbles are released with no periodicity. 129

Figure 5.23: Electrochemical noise spectra at low frequency range for the conditions of figure 5.22, with $B_V \parallel S_V$ configuration, showing transition from periodic to aperiodic bubbling. The periodicity in (a) and (b) is indicated by the main peak, which broadens progressively in (c) and (d) until it the spectrum is flattened in (e) 130

Figure 5.24: Reduction or increase of bubble size depending on field polarity, for $B_H \parallel S_V$ configuration showing (a) the overpotential oscillations and images of the bubbles release, and (b) corresponding changes in power spectra density for both polarities of the field. A current density of 20 A cm^{-2} was applied to a Cu vertical microelectrode, the fields applied were 0 and ± 1.5 T.The residence time is modified by the action a convective force pointing up or downwards. The oscillation patterns change accordingly, and the PSD structure varies in the low frequency range, exhibiting a two-step plateau when IR component prevails. 132

Figure 5.25: Field effect on electrochemical noise spectra, for the $B_H \parallel S_V$ configuration with Lorentz force acting downwards. A copper microelectrode of 125 μm in diameter was used at constant current density of 3.5 A cm^{-2}. 133

Figure 5.26: Dependence of the frequency of bubble release with Lorentz force magnitude for $B_H \parallel S_V$ configuration, when it opposes gravity. 133

Figure 5.27: Overpotential oscillations and its relation to bubble size for fields directed perpendicular to the electrode surface for $B \perp S$ configurations. (a) Time sequences for fields up to 5 T with $B_V \perp S_H$ configurations are shown for Cu microelectrode. The corresponding bubble size and release frequency are plotted in (b). $j = 5$ Acm^{-2} . 135

Figure 5.28: Overpotential oscillations and its relation to bubble size for fields directed perpendicular to the electrode surface for $B \perp S$ configurations. (a) Time sequences for fields up to 5 T with $B_V \perp S_H$ configurations are shown for a Pt microelectrode. The corresponding bubble size and release frequency are plotted in (b). $j = 20$ Acm^{-2} . 136

Figure 5.29: Time sequences at 0 and 1.5 T with $B_H \perp S_V$ configurations for a Pt microelectrode. The corresponding images indicating bubble size are seen on the right panel. 137

Figure 5.30: Motion track images showing rotational flow for the $B_V \perp S_H$ configuration. PVC particles are used to track the flow. Vertical field applied is 0.44 T. 138

Figure 5.31: Motion tracking image showing rotational for the $B_H \perp S_V$ configuration. Horizontal field applied is 1.5 T. PVC particles are used to track the flow. A two-cell vortex is identified, with an outer swirling away motion feeding an inlet flow backwards to the electrode. The inlet flow is tracked by following numbers 1 to 6. 140

Figure 5.32: Scheme of a two-celled vortex structure due to the Lorentz-induced rotational motion around one single bubble for B $\perp$ S configurations 142

Figure 5.33: Chart summarizing the field and current effect on the transition from single to multiple bubbles. Conditions which determine coalescence in these cases are related to the residence time and solute (dissolved gas) redistribution. 144

Chapter VI

Figure 6.1: Variation on current density during copper electrodeposition at overpotential η = -40 mV, corresponding to the activation control zone for copper reduction, when a field of 1.5 Tesla is applied. Electrolyte corresponds to 0.1 M $CuSO_4$ electrolyte (a) naturally aerated, or (b) argon bubbled. 152

Figure 6.2: Profiles and morphology of samples grown from a 0.3 M $CuSO_4$ electrolyte, at η = -40 mV during 300 seconds, under magnetic fields up to 4 Tesla. The upper panel shows the profiles in the (*yx*) plane, showing the action of the Lorentz force. The lower panel shows the vertical profiles in the (*zy*) plane. Optical views (10x) are shown on the right column. 154

Figure 6.3: SEM images of copper deposits around a pore at 0 and 4 T for deposits grown under activation control at η = -40 mV, showing effect of the field on growth and a higher presence of oxygen when deposition was performed under field. Lower panel: ratio of oxygen to copper counts, along the line scans, indicating that the field increases oxygen content in the sample. 156

Figure 6.4: Scanning electron microscope images showing copper deposits obtained in co-reduction with hydrogen during 25 seconds, from a 0.3 M $CuSO_4$ solution. No field is applied. 159

Figure 6.5: Scanning electron microscope images showing the effect of fields in morphology in relation with hydrogen co-reduction with copper for deposits grown during 5 seconds at (a) $j / j_{L1} > 1$, B = 0 T and (b) $j / j_{L2} > 1$, B = 4 T, where $j_{L1} < j_{L2}$. 161

Figure 6.6: Zoom-out of site producing different sizes of hydrogen bubbles. Electrolyte 0.3 M $CuSO_4$, B = 4 T, deposition time: 25 s. 162

Figure 6.7: Current efficiency calculated from data obtained with an electrical quartz microbalance, for co-reduction of copper and hydrogen at η = 1.0 V, from a 0.3 M $CuSO_4$ solution. (a) 0 T, (b) 1.5 T. 164

Figure 6.8: Magnetic field effect on roughness, obtained from scanning white light interferometry measurements on samples grown at the co-reduction regime. The system is forced to maintain $j/j_L > 1$. (a) 0 T (b) 1.5 T. 165

Figure 6.9: Scanning electron microscope images showing the effect of fields in morphology in relation with hydrogen co-reduction with copper. (c) $j/j_{L1\,(B = 0\ T)} > 1$, and (d) $j/j_{L2\,(B = 4\ T)} < 1$, where $j/j_{L1} < j/j_{L2}$. 167

Figure 6.10: Time sequences sampled at high frequency (100 kHz), showing the field effect on voltage and distribution of growth events (peaks) when $j/j_{L1\,(B=0\ T)} > 1$ shifts to $j/j_{L2\,(B\neq1.5\ T)} < 1$. 167

Figure 6.11: Electrochemical noise spectra of the working electrode potential during copper deposition under no field and 1.5 T under galvanostatic control. (a) When hydrogen evolution is suppressed, j = 700 $A{\cdot}m^{-2}$, associated with figure 3.51. (b) When strong hydrogen co-reduction is produced at j = 20 Am^{-2}, using a microelectrode. We compare in the graph the effect of $\boldsymbol{F}_L$ orientation. The electrolyte is 0.3 M $CuSO_4$ + 1.2 M H_2SO_4. The black line shows $1/f^2$ slope. Data shown are undersampled to 1000 Hz from the 100 kHz raw data. 169

Figure 6.12: Electrochemical quartz crystal microbalance measurements taken for deposition set above the limiting current density. (a) Total change of overpotential, (b) copper current calculated from frequency variations related to changes of deposited mass, and (c) differential current, corresponding to evolved hydrogen gas. 171

Chapter I

Introduction and literature review

I.1 Motivation

Industrial processes involving electrochemical phase transformations are important to sustain modern society. Copper, a metal of high demand for electronics, electric and building industry, is brought to a high purity state by electrolysis, where copper ions contained in a solution are crystallized onto a cathode by the passage of current.

Industrial production of copper by electrolysis faces several challenges regarding high power consumption, growth morphology of the final product as well as the space and time used to achieve a certain production rate, known as space-time yield. These challenges ultimately stem from limitations on the mass transport of species between the bulk solution and the reacting surface of the electrodes involved [1].

Since it is known that magnetic fields can influence mass transport-limited reactions, we explore in this thesis the effects of uniform horizontal and vertical magnetic fields on the electrochemical phase transformations occurring in a copper electrolysis cell. We do this for several conditions where mass transport limitation is relevant, and we integrate the effect of gravity as a source of convection as well. Our aim is to evaluate how, by influencing the mass transport-limited cell reactions, the use of magnetic fields can help reducing space-time yield and power consumption while maintaining a good deposit quality and reducing the space-time yield.

I.2 Reactions occurring in industrial copper production

Electrolysis is used in many industrial processes to obtain pure copper metal in different shapes and thicknesses. Depending on the characteristics of the deposit obtained and on the source of the ion, the following processes are distinguished:

a. Electrowinning (EW): where a dense and compact deposit is obtained from a solution.
b. Electrorefining (ER): where a pure dense and compact deposit is obtained from an impure metal, through its anodic dissolution and subsequent cathodic deposition.
c. Electroplating: where a compact thin layer is obtained from a solution.
d. Electroforming: where metallic pieces with specific shapes are fabricated via electrolysis.

All of them are cathodic processes taking place, for the case of copper, according to the equation:

$$Cu^{2+}_{(aqueous)} + 2e^- \leftrightarrow Cu^0_{(solid)} \qquad E = 0.34\ V \qquad (1.1)$$

which is positioned at 0.34 V in the scale of standard electrode potentials.

Electrowinning is a good example of an electrolytic cell. Figure 1.1 shows a scheme for copper electrowinning. In EW, the anodic reaction is oxygen evolution reaction (OER) from water, given by:

$$2H_2O_{(aqueous\ )} \leftrightarrow O_{2(gas)} + 4H^+ + 4e^- \qquad \text{E} = 1.23\ \text{V} \qquad (1.2)$$

In electrorefining (ER), instead of oxygen evolution, the copper reaction of Eq. (1.1) proceeds, reversed, at the anode. This means that copper dissolves from metal to ionic state.

Two side reactions may also occur at the cathode along with copper metallization. One is the reduction of dissolved oxygen gas into water, according to Eq. (1.2), reversed, and the second one is proton reduction to form hydrogen gas, known as hydrogen evolution reaction (HER), which proceeds according to:

$$2H^+{}_{(aqueous\ )} + 2e^- \rightarrow H_{2(gas)} \qquad \text{E} = 0.0\ \text{V} \qquad (1.3)$$

For charge transfer to occur, two mutually complementary half-reactions are needed: one produces electrons while the other consumes them. In the case of the studied system, they correspond to equations (1.1) and (1.2). They occur in physically separated places – the anode and cathode in figure 1.1. The sum of both half-reactions is known as the redox (reduction – oxidation) reaction.

When a solid phase is formed at the cathode through this process, the reaction is generally known as electrodeposition. In this system, the electrodeposited species is copper. When a solid undergoes phase transformation into a liquid through this process, it is generally called anodic dissolution. That is the case of copper dissolution in ER. Both are described by Eq. (1.1).

When a gas is the product, either through cathodic or anodic processes, the reactions are known as evolution reactions. That is the

case of the oxygen evolution reaction (OER) at the anode in EW, Eq. (1.2), and of hydrogen evolution reaction (HER) at the cathode under high polarization conditions, Eq. (1.3). Also, at cathodic conditions, dissolved oxygen may reconvert to water through the oxygen reduction reaction (ORR), described by Eq. (1.2) reversed.

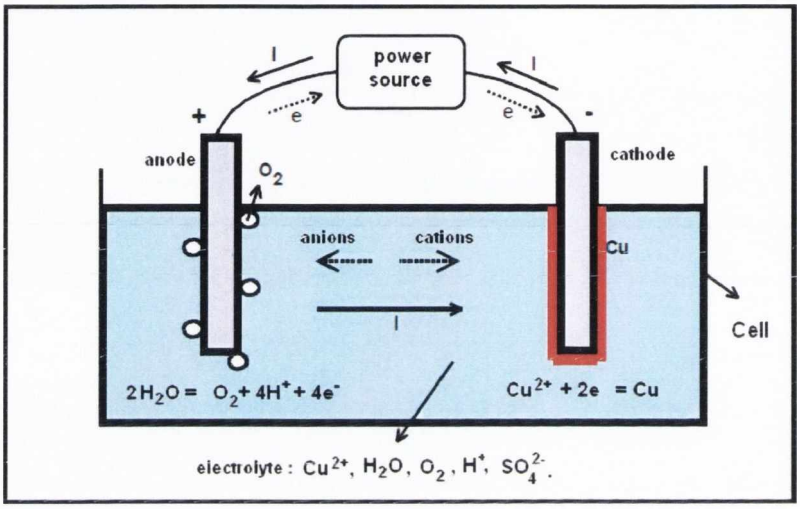

Figure 1.1: Scheme of an electrolytic cell showing the product species at the cathode and anode for the reactions involved in copper electrowinning (EW).

I.3 Electrochemical formation of bulk phases

The stability zones for aqueous systems can be calculated from thermodynamic data to obtain a potential-pH – or Pourbaix – diagram of equilibria. The system of interest in this study is the acid copper system. Figure 1.2 shows a simplified Cu-H_2O Pourbaix diagram, indicating the zone of interest, coloured, on the left side. Values on the ordinate, E_{SHE}, correspond to the potential with respect to the standard hydrogen electrode (E_{SHE}), the reference value for the thermodynamic scale of redox potentials. Values on the abscissa correspond to the pH of the aqueous system. The reactions between species are represented by lines.

Since these diagrams are calculated from thermodynamic data, they inform about the viability of a process according to the free energy criteria, and regardless of any kinetic aspect.

In the figure, lines (b) and (a) represent respectively, the OER and HER reactions of Eq. (1.2) and (1.3). They delimitate the zone of water stability. The cathodic possible reactions are found within the yellow zone and the anodic ones in the green area. Both zones are separated by the equilibrium between metallic and ionic copper – the horizontal line between them, representing Eq. (1.1) [2].

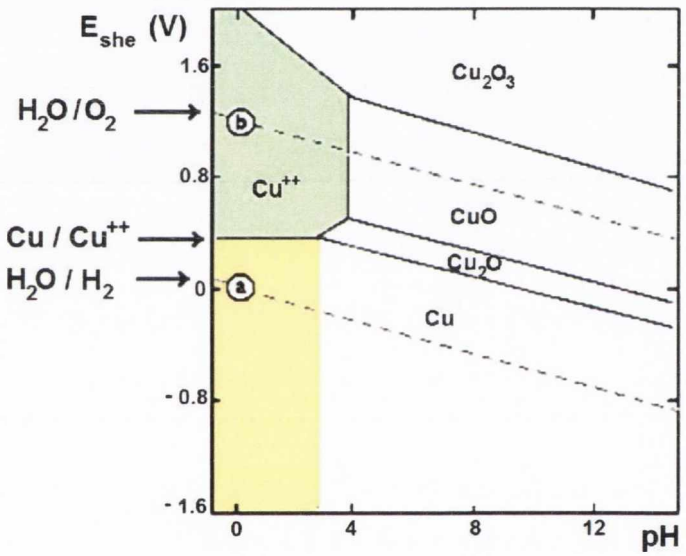

Figure 1.2: Summarized Pourbaix diagram (potential – pH) for the system Cu – H_2O at 25° C [2], where reactions relevant for copper electrolysis are highlighted. The cathodic reactions occur within the yellow area, while the anodic reactions occur within the green area.

Under electrochemical equilibrium, species coexist. In these conditions a system is stable, implying no net formation, growth or dissolution of phases. When one phase becomes supersaturated,

equilibrium conditions are disrupted; hence reactions with electron exchange are possible. In order to reach supersaturation conditions in an electrolytic cell, a potential beyond that of the equilibrium – or overpotential (η) – is imposed. The overpotential is defined as:

$$\eta = E^0 + \eta_{diff} + \eta_{cryst} + \eta_{IR} \tag{1.4}$$

where E^0 is the standard equilibrium potential and the other terms correspond to the contributions of diffusion, crystallization and solution resistance to the overpotential value.

By applying a potential difference, the system becomes polarized; equilibrium is unbalanced, which promotes an electrochemical reaction in which charge transfer will tend to diminish the free energy of the system, ΔG. The cathodic processes of interest in this study are triggered by applying a negative potential to the substrate (electrode). On its surface, heterogeneous reactions producing metal and gas may proceed. When various species are present in solution, there are possibilities of producing simultaneous reactions over the electrode surface, provided that the necessary supersaturation conditions are met. In the case of this study, no foreign ions are present. However, there are still possible side reactions: those described by Eq. (1.2) and (1.3) on the cathodic area of figure 1.2. In other words, hydrogen and oxygen gas may be present during copper metallization.

The formation of a new phase involves the production of a stable interface. Accordingly, nucleation is the earliest stage of the phase transformation process. A nucleus or cluster can be roughly defined as an aggregate of atoms which possesses the same properties of the macroscopic phase that it will form after growth. As the forming phase is different from the surroundings, a phase boundary is formed which has associated a certain surface energy, ΔG_S. This contributes to the total free energy ΔG, increasing it. As a consequence, many clusters re-dissolve because their free energy is too high to form a stable phase.

Clusters overcome their surface energy by increasing their volume. The scheme in figure 1.3(a) represents what happens when a cluster of atoms gather to form a spherical shape. As it increases its size, surface increases and so does its energy (positive). The total energy, given by the sum of the surface and volume energies, is positive so long as the surface contribution is larger than that of the volume (negative). At a certain critical size, given by the associated critical radius r*, the volume contribution dominates and the energy variation is reduced as the cluster keeps growing. After that, the cluster is a stable nucleus and may keep growing [3-8].

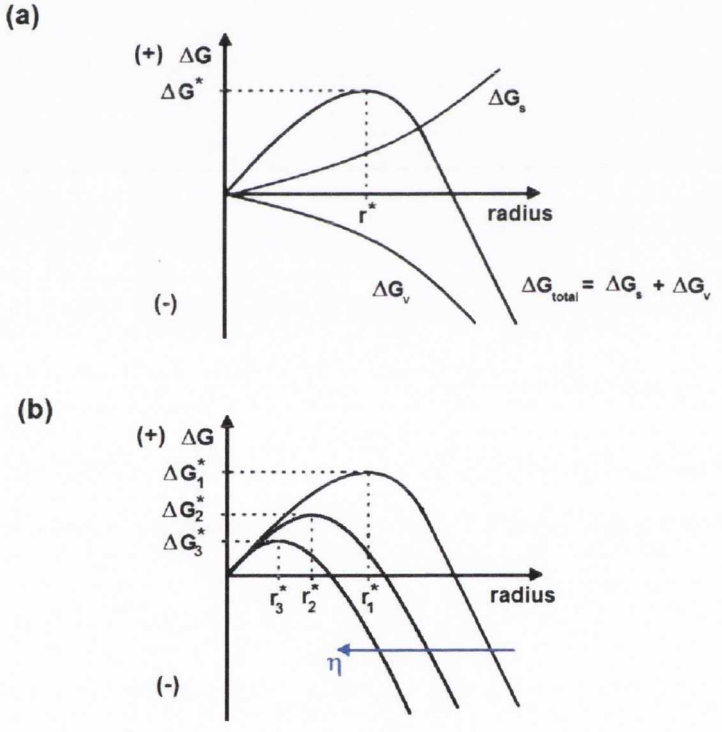

Figure 1.3: (a) Free energy variation (ΔG) of a system as a result of the volume and surface energies contribution (ΔG_V and ΔG_S), indicating the critical radius r*. (b) Reduction of the critical radius r* as a function of overpotential η [7].

Supersaturation and the critical radius for nucleation are related. High supersaturation conditions imply that the critical size to form stable nuclei is lower, since the Gibbs free energy for transformation is higher. Polarized electrodes exhibit high supersaturation values, thus phase transformations are much favoured at higher overpotentials. A scheme of this is shown in figure 1.3(b).

The reactions taking place are heterogeneous, i.e. there is a contact zone, the interphase, through which mass is transferred from one phase to the other. It is usual that in heterogeneous systems the two-phase mass transport determines to certain extent the rate of the global reaction.

In phase forming reactions, the diffusion through the zone adjacent to the reaction surface may determine the reaction rate. When the reaction commences, a concentration gradient is gradually established near the surface, as figure 1.4(a) shows. For conditions of constant stirring, the thickness of this zone remains constant and stationary state is achieved. Here, the amount of material transferred in and out the zone is equal.

The first Fick's diffusion law relates the amount of mass diffusing perpendicularly per time unit through a specific area and the concentration gradient:

$$J = -D\frac{\partial C}{\partial x} \tag{1.5}$$

where J is the mass flux in moles m^{-2} s^{-1}, C is the concentration of dissolved species in moles m^{-3}, x is position coordinate and D is the diffusion coefficient of species in determined medium at certain temperature, given in m^2 s^{-1}.

The Nersnt layer is a thin film of fluid adjacent to the surface, through which species are transported by diffusion only. It is derived from a linearization of Fick's law, as follows:

$$J = \quad -D\frac{C_0 - C_S}{\delta} \tag{1.6}$$

where C_0 is the concentration of species in the solution bulk, C_S is the concentration of species at the surface and δ is the thickness of the Nernst diffusion layer. Mass transport rate can be enhanced by reducing the diffusion layer thickness, increasing the concentration gradient (augmenting C_0), increasing the contact area or increasing the temperature.

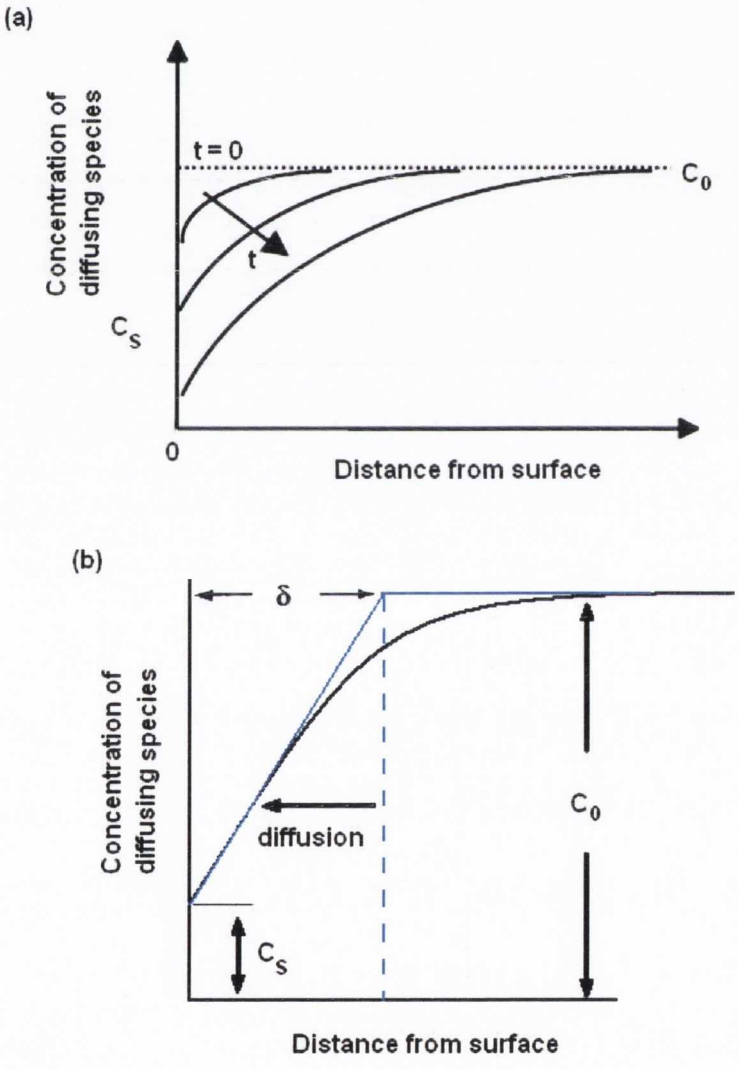

Figure 1.4: (a) Concentration of a species being consumed at the reacting surface, as a function of distance and time, (b) linearized concentration gradient, according to Nernst, Eq. (1.6).

I.4 Overpotential – current relationship

In the previous section the relevant reactions were described in terms of their location in an equilibrium diagram, and this was related to supersaturation conditions by the overpotential. In the present section the reaction rates are taken into account.

In electrolytic reactions there is a relationship between the supersaturation conditions and the kinetics of the overall process, expressed in terms of overpotential (η) and current density (j), respectively. Figure 1.5 shows the relation between the electrode potential and the flow of current through the reacting area, known as polarization curve. The reaction rate, in electrochemistry, is considered equivalent to the current density j, which accounts for the amount of charge passed through a specific reacting area.

If mass transport is the slow path of the overall reaction, the species concentration being consumed at the reacting surface is near to zero. Hence, the reaction rate depends on the approach rate of the ions to the surface. The value corresponding to the current plateau is known as the diffusion limited current density, j_L, and is measured when the difference between the concentration of species at the electrode surface and in the bulk electrolyte is maximum, as figure 1.4(b) shows. Its value is given by:

$$j_L = \frac{nDFC_s}{\delta} \tag{1.7}$$

where n is the number of electrons involved in the reaction, D is the diffusion coefficient, F is the Faraday constant, C_s is the ionic concentration at the bulk and δ is the thickness of the diffusion layer.

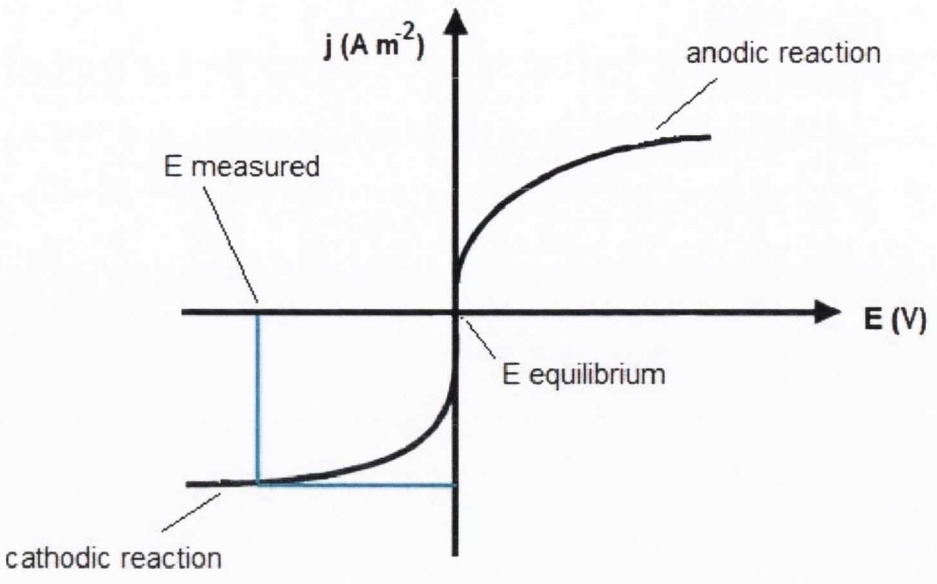

Figure 1.5: Scheme representing the overpotential – current relationship.

Figure 1.6(a) shows a general cathodic overpotential – current (η–j) relationship, where four successive regions can be distinguished: linear, exponential, mixed control and mass transport limited regions. The η- j relationship has initially a linear region, followed by an exponential region (zones 1 and 2). At these low supersaturation conditions (low η) the transfer of electrons to the cations is a slow process and the electrode reaction rate is determined by the charge transfer.

At much higher overpotentials (zone 4), the slow process is now transport of species between electrode and solution, hence the overall reaction rate is mass transport controlled. As figure 1.6(a) shows, this zone is characterized by a current plateau, the diffusion limited current density j_L. The zone in between 2 and 4 corresponds to a mixed controlled region (zone 3), where charge transfer and mass transport occur at relatively similar rates [3-9].

The right part of figure 1.6(a) relates deposit morphology with the ratio between the applied current density j and its limiting value j_L, Eq. (1.7). Morphology is determined by the relation between overpotential

and current. Depending on the lattice characteristics of the forming phase and the substrate, as well as the electrode overpotential, crystals spread to their sides and/or project into the fluid according to the growth rate of their planes. Eventually, the formerly independent growth centres approach until their diffusion zones overlap. Propagation of the solid phase (i.e. growth) leads to the development of a characteristic morphology and surface profile. This is determined by the relation between overpotential and current, leading to different particle shapes, as indicated on the figure. The j/j_L quotient – i.e. the ratio between the current applied j and that limited by mass transport, j_L Eq. (1.7) – constitutes a very useful parameter to describe growth in real systems [9-12].

In copper electrowinning, current densities are maintained as high as possible without compromising the deposit quality. This has traditionally been between 200 and 300 $A \cdot m^{-2}$, which corresponds roughly to j/j_L ratios between 0.5-0.6. Figure 1.6(b) shows an example for industrial EW at a current density of 220 $A \cdot m^{-2}$. The corresponding measured overpotentials, cathodic and anodic, are indicated in the polarization curves. It is seen that:

a. Cathodic current is kept well below the plateau limit.
b. The corresponding anodic current is identical, with opposite sign.
c. The cathodic overpotential (η_c), associated to copper is relatively low (< 0.1 V)
d. The anodic overpotential (η_a),associated to the OER is high (~0.6 V).
e. The difference between cathodic and anodic reactions is 0.9 V.

The composition of the cell voltage contains these contributions plus the electrolyte resistance IR and current loses. Typically in this system, IR and losses add 0.5 V to the cell voltage, so it can be estimated a total drop of over 2.1 V. Considering the high tonnage treated in this manner, EW processing is an energy-intensive process. Hence,

diminishing the cell voltage, even in slight measure, would be a great contribution to reduce power consumption.

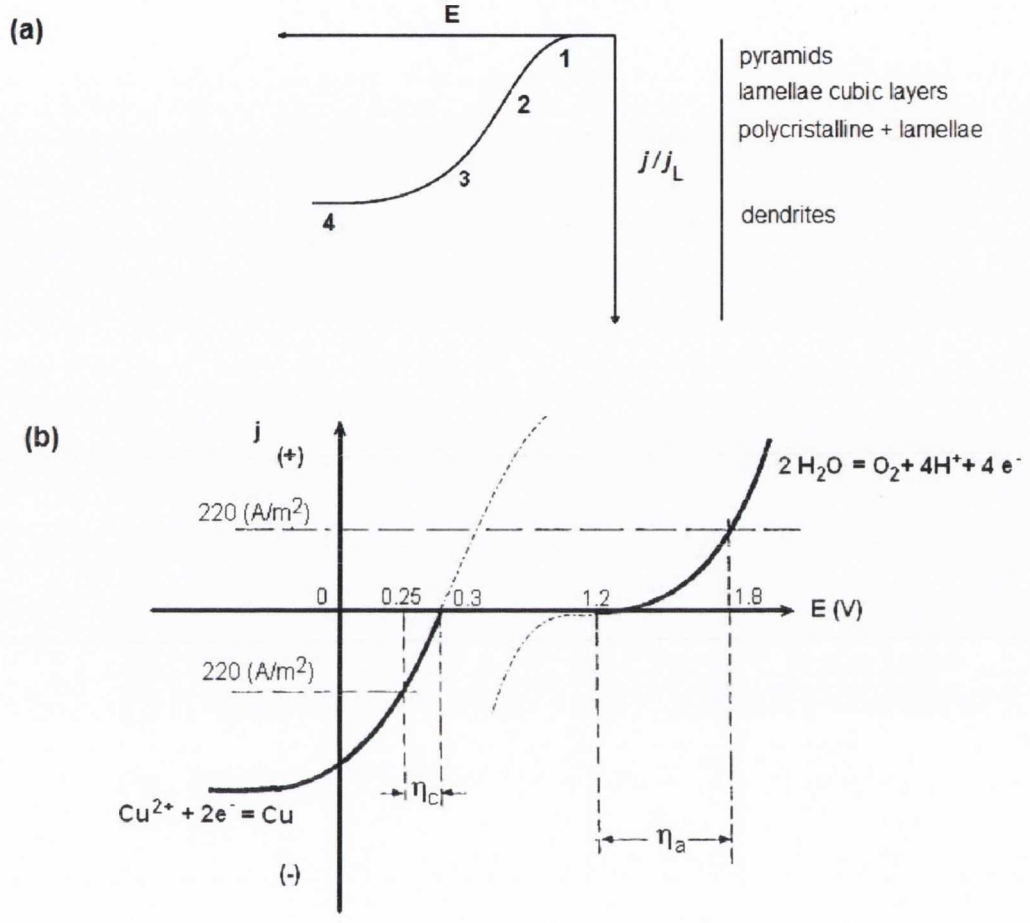

Figure 1.6: (a) Scheme showing the general case of current-potential relationship for a metallization process, showing: linear (1), exponential (2), mixed control (3) and mass transport limited (4) regions. These are related to growth modes at the right-hand side of the scheme [3]. (b) An example of polarization curves for copper electrowinning, relating current density with the corresponding cathodic and anodic overpotentials.

A great part of the IR contribution to cell voltage stems from the OER because the gas occludes the electrode surface. However, if the cathodic process were conducted at higher rates, closer to the plateau values, local conditions may promote hydrogen production through the

HER, raising another ohmic contribution. Both hydrogen and oxygen evolution reactions are very important for industrial systems. Hence, in the present work, formation of gas phase is also in the scope of this study. An interesting article on water electrolysis reviews recent progress from theory to applications [12].

Gas phase formation implies, as for the solid case, supersaturation and nucleation at the early stages. The overpotential value is also related to current density for the electrochemical reaction. The physicochemical conditions define the amount of gas to be stored in solution in its molecular form, or supersaturation value. Bubbles start to form when this value is reached locally [13]. At early stages of growth, bubbles can be found colloidally interspersed in the electrolyte [14], after which they may grow, coalesce and form bigger bubbles. It is important to be aware that the more sensitive the visualization technique the higher should be the proportion of observed gas with respect to the current actually transformed.

I.5 Current distribution, mass transport and the role of convection

In practice, all electrodes have a non-uniform distribution of current across their surface, and the measured quantity corresponds to its average. Current distribution represents the local rate of reaction on a given surface. Uneven current distribution implies diverse local rates of growth and, hence, differences in the properties therefore developed.

Sources of uneven current distribution are structural, diffusional and ohmic. A structural cause of uneven current distribution arises from the fact that different crystal faces have different surface energies which

lead to different rates of reaction. Diffusional causes of uneven current distribution originate from variations of the mass transport rates between different points in the electrode surface and the bulk solution. This is usefully expressed in terms of the effective thickness of the diffusion layer, δ. Ohmic sources of non-uniform current distribution arise when the resistance of the solution between the bulk and different points at the electrode surface exhibit strong differences, in which case current will concentrate at those sites offering the path of least resistance.

The current distribution relates to three components: electrolyte resistivity (IR), the activation overpotential and the concentration overpotential. Depending on which contributions are relevant the current distribution is defined as primary, secondary and tertiary.

Primary current distribution is related to the macroscale. It is completely controlled by the electrolyte resistivity between working and counter electrodes; hence, cell and electrode geometry is determinant. Other effects are neglected.

Secondary current distribution is controlled by electrolyte resistivity plus the charge transfer resistance of the reaction. The current takes into account the effect of the activation overpotential, so if the reaction is slow compared to electrolyte resistivity, the current distribution is more uniform. Concentration overpotential is ignored, so this is basically related to reactions occurring under activation control, i.e. with no mass transport limitation.

Tertiary current distribution is controlled by the electrolyte resistivity plus charge transfer resistance plus concentration overpotential. It is mass transport limited and is most relevant to our study. The concentration changes occurring at the electrode surface affect the reaction rate, therefore they can be considered as an additional surface resistivity. Tertiary current distribution is important to achieve

smooth plating quality at substrate trenches. One important parameter in this realm is the ratio between the roughness amplitude and thickness of the Nernst diffusion layer (Eq. 1.6) [15, 16].

Figure 1.7 shows a scheme of the relation between surface profile and the diffusion layer. In (a) the case of roughness amplitude much higher than the diffusion layer thickness is shown; this is called macro-roughness. Here tertiary current distribution is not important and the current distribution is similar in valleys and peaks. In figure 1.7(b) the case of roughness amplitude lower than the diffusion layer thickness is shown. This is called micro-roughness, where tertiary current distribution becomes important, and current distribution in valleys is much lower than at the peaks. In (c) the case of very pronounced and irregular surface roughness is shown. In this, both the roughness amplitude and diffusion layer thickness vary widely from one point to another, so that the two previous cases may be present. Current distribution is correspondingly irregular.

Mass transport by diffusion in the electrolyte gives rise to morphological instabilities during solid growth. The formation of a solid involves an interface moving towards the electrolyte whose advancing rate depends on current distribution. Mass transport conditions across the diffusion layer may vary from one point of the surface to another, amplifying any local differences and generating enhanced local growth in certain areas with respect to others. This gives as a result non-uniform deposits. A thorough review describing kinetic roughening of growing surfaces has been published by Schwarzacher [17].

The scale of surface irregularities is very important. It is so also for its quantitative measure. Defined as the difference in height (h) of a surface over a certain length (l), the roughness value ω depends strongly on the scale. The root mean square roughness is given by:

$$\omega(l) = \sqrt{(h - \langle h \rangle)^2} \tag{1.8}$$

hence, its value can vary widely within the same sample just by changing the measuring scale.

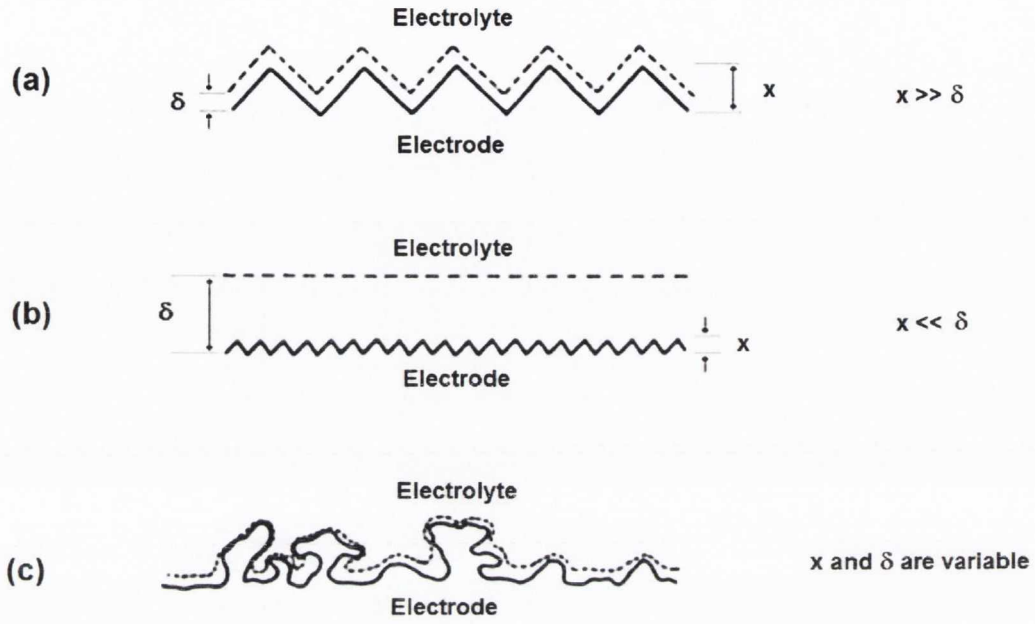

Figure 1.7: Scheme showing the relation between roughness amplitude (x) and diffusion layer thickness (δ), related to the relative limited current density on peaks and valleys. (a) Macro-roughness, (b) micro-roughness and (c) variable conditions.

The effect of the scale is also crucial when access of fresh electrolyte to recesses and dispersal of exhausted electrolyte from it are hindered. In those cases electrodeposition is inhibited. This becomes very important when a specific deposit quality is required. For example, if the aim is obtaining a bright deposit, then the scale of interest is the wavelength of visible light (0.4 to 0.8 μm). In such a situation, the ability to produce smooth deposits is crucial, and for such purpose usually additives are used. They inhibit uneven growth via specific adsorption in hills or valleys of the advancing interface.

It has been seen that mass transport is relevant during growth at high current densities and is thus a key factor in industrial electrolytic processes. Due to production requirements, industrial processing involves the decision of working at, or near to, the limiting current, j_L. The reactions taking place with mass transport limitation depend on the concentration gradient of electroactive species ahead of the interface, $\Delta C/\delta$. The ratio between the concentration variation and the diffusion layer thickness depend on the surface concentration and Reynolds number, respectively, which in turn are related to the j/j_L ratio. This stresses the importance of the limiting current value of a system, j_L (Eq. 7). Reynolds number is defined as the ratio between inertial and viscous forces, and is given by:

$$Re = \frac{\rho V L}{\mu} \tag{1.9}$$

where ρ is the fluid density, V is the mean fluid velocity, L is a characteristic length and μ is the dynamic viscosity of the fluid. Reynolds number is, thus, related to the hydrodynamics of the system and hence to the thickness of the diffusion layer, δ.

It is clear that the local j value varies due to structural, physical and hydrodynamic conditions of the system. In general terms, it is possible to establish that the distribution of potential varies according to the substrate's physico-chemical properties, while current distribution changes according to surface roughness and flow variations. The flow variations include natural convection, flow segregation, turbulence, gas evolution, secondary flows or other sources of change in the system's hydrodynamics [9]. This is relevant, as it allows controlling the current distribution by varying the electrolyte flow. It also points to the role of gravity in electrochemical phase transformations. The differences in electrolyte density derived from these processes make local volumes of fluid susceptible to gravity, introducing a driving force for convection. In the case of solid phase formation this force is known as natural

convection, $\boldsymbol{F}_{NC}$, and for gas formation as upthrust, $\boldsymbol{F}_{UP}$. They are given by:

$$\boldsymbol{F}_{NC} = \boldsymbol{F}_{UP} = \Delta\rho\boldsymbol{g} \tag{1.10}$$

where $\Delta\rho$ is the density variation between two fluid volumes and $\boldsymbol{g}$ is the gravitational acceleration. Typical values of these forces in an electrochemical cell would be of the order of 1000 N m^{-3}. Natural convection has been reported to produce fluid motion during electrodeposition [18] influencing velocity and concentration profiles in front of the electrode [19], affecting growth morphology [20, 21].

I.6 Magnetohydrodynamics and electrochemistry

Magnetohydrodynamics, MHD, describes the processes where a magnetic field promotes motion within a fluid which is susceptible to magnetism. When an electrolyte is the chosen fluid, this interdisciplinary area of study is known as magnetoelectrochemistry. The magnetic field effects in electrochemistry have been reviewed at least once per decade since 1980's [22-27]. The field is known to affect fluid dynamics, which is directly related to mass transport limited reactions and growth.

The main effect of a magnetic field in electrochemical reactions has been described as gentle stirring, and attributed to the Lorentz force, $\boldsymbol{F}_L$. This force arises from the interaction between the orthogonal lines of magnetic field and the electric current, according to the cross product:

$$\boldsymbol{F}_L = \boldsymbol{j} \times \boldsymbol{B} \tag{1.11}$$

where $\boldsymbol{j}$ and $\boldsymbol{B}$ are the vectors of curremt density and magnetic field intensity. Lorentz force magnitude has been considered similar to that of the natural convection force $\boldsymbol{F}_{NC}$ [25]. Thus, it seems relevant to consider a possible interaction between the Lorentz and natural convection forces

when the field effect on electrochemical formation of solid and gas are described.

I.6.1 Field effect on the electrochemical response

Since magnetic fields are known to produce convection, their effect on current density j can be described by the use of Navier-Stokes equations. Numerical simulation has recently succeeded in describing some experimental findings [28-31]. In most cases though, relations based on the pioneering work by Aogaki [32] have been used They are of the type:

$$\boldsymbol{j}_L \propto \boldsymbol{j}_0 + \alpha \boldsymbol{B}^n \tag{1.12}$$

where $\boldsymbol{j}_L$ is the limiting current density, $\boldsymbol{j}_0$ is the current at zero field, α is a proportionality constant and n = 1⁄3. Modifications have been proposed in literature adding terms as concentration, diffusion coefficient, kinematic viscosity, dielectric constant, number of electrons involved and proportionality constants [33, 34].

In the case of copper magnetoelectrodeposition, the diffusion limited current corresponds to the proportionality relation given by:

$$\Delta \boldsymbol{j}_L = j_{L(B)} - j_{L(B=0)} \propto \boldsymbol{B}^{1/3} C_0^{\,4/3} \tag{1.13}$$

where $\boldsymbol{B}$ is the intensity of field applied and C_0 is the bulk concentration of the electrolyte [35-37].

I.6.2 Field effect on phase growth

I.6.2.1 Solid phase: Copper.

The effect of magnetic fields on the morphology of solid deposits has been reviewed by Fahidy [24]. Two characteristic cases are found: for fractal growth carried out in flat cells, the branches orientation is shifted according to the field direction. For bulk deposits, fields promote smoother surfaces. This is valid for the copper system as well [37-39]. More recently, effects at the microscale have been reported. Field influence inside the diffusion layer was observed by Krause [40], and changes in mass transport-controlled deposition of copper was produced by field gradients by Tschulik [41]. A recent communication describes changes in copper surface profiles in relation to the overpotential [42]. Surface evolution, local distribution of current, profiles or growth mode has not yet been discussed in terms of j/j_L ratio.

I.6.2.2 Gas phase: Hydrogen.

The field effect on gas phase growth has been subject of recent investigation, in relation to water electrolysis. For the case of cathodic hydrogen only (not along with any metal deposition), literature indicates that applying magnetic fields increases the gas production rate and reduces bubbles size [43, 44]. The explanation is related to the interaction between magnetic flux and current lines in the base of the growing bubble, leading to the so-called "twist-off" effect. This has been described as a toroid motion around the rim of the electrode on the bubble base, promoting bubble detachment. This proposed explanation,

however, is still not based on observations of the behaviour of a single bubble immersed in a magnetic field.

I.6.2.3 Growth of solid in presence of gas phases

Although the co-reduction of gas and solid is largely known in industrial processing, theoretical descriptions of it are mostly recent. Hydrogen evolution is sometimes the unavoidable secondary reaction for several metallization processes, thus the aim is minimizing it. In some cases, however, gas growth during metallization is useful to produce three-dimensional patterns [45-47], where gas bubbles are used as a dynamic template around which the solid grows.

The effect of magnetic fields on the simultaneous growth of solid and gas has been reported mainly for cobalt and nickel systems. Field imposition enhances or diminishes hydrogen currents depending on the overpotential used [48-51]. Only the work by Hinds and co-workers [37] studied this aspect of copper magnetoelectrodeposition. In that report, the highest part of the cathodic branches, corresponding to hydrogen co-reduction with copper, exhibit lower current values and a crossover with respect to the ones obtained under no field influence. No explanation for this experimental fact has been proposed, which was manifest at pH values both 3.5 and 0.5.

Morphological evidence of a field effect on copper deposition at low overpotentials was reported by Matsushima and co-workers [38] who found that, at -60 mV versus a copper reference electrode, magnetic fields promoted smaller grain size. For the case of a 5 T field they observed particle size reductions from 20 to 5 microns.

O'Reilly et al [39] have reported negative changes in current for copper magnetoelectrodeposition at overpotentials related to activation

control when fields were applied. In a previous report, we showed that copper growth and currents may be inhibited at low overpotentials as a result of magnetoconvection [42].

Work by Fricoteaux and Douglade [52] addresses the influence of different modes of convection on copper electrodeposition. They found that, at low cathodic currents, the growth of certain copper textures was inhibited due to convection-enhanced oxygen adsorption on the electrode surface.

I.7 Overview of the following chapters

In the following chapters the study of the field influence on the cathodic acid copper system is presented. In Chapter II the experimental procedures, equipment and characterization techniques are described. Chapter III describes the first, electrochemical approach to the field effect. By use of diverse electrochemical techniques, the influence of the field on the measured response is described. Field intensity, electrolyte concentration and position relative to gravity, as well as electrode area are analyzed.

Chapter IV describes the growth of solid copper under the field influence. By use of potentiostatic and galvanostatic techniques, the different growth modes are analyzed. Deposits were characterized in terms of morphology, thickness and roughness. Current distribution is discussed according to the combined observations.

Chapter V describes the influence of magnetic fields on growth of hydrogen bubbles, one of the secondary cathodic reactions of the acid copper system. In this chapter the hydrogen evolution reaction is studied alone, i.e. without any copper in solution. A method to study the bubbles bubbling regime and maximum size is developed combining electrochemical noise and high speed photography. The noise method is first validated, then the physicochemical aspect of bubbling are addressed, to then finally analyze the effect of the magnetic fields. The relative orientation of the fields to the electrode surface and gravity are considered in full.

Chapter VI combines the knowledge gathered through the previous chapters and addresses the field effect when copper grows with in the presence of a simultaneous gas-phase reaction. Morphological and electrochemical analysis are in place, and current efficiency is discussed.

Chapter II

Experimental methods

During this investigation, the influence of magnetic fields on the electrochemical formation of bulk solid copper and bubbles of hydrogen gas from acid sulphate electrolytes was studied. Electrolytic cells were placed inside uniform magnetic fields before the reactions were run. The experimental information was extracted from the electrochemical response and the reaction products. The response was monitored with diverse electrochemical techniques. Copper metal deposits were characterized after magnetoelectrodeposition, while growth of hydrogen bubbles was studied in situ with a high speed camera during the reaction.

In the following sections, the experimental procedures and setup are described.

II.1 Magnetic and electrochemical devices

II.1.1 Magnetoelectrochemical cell

The ***working electrodes*** (WE) used were made of high purity metal wire (Cu or Pt) embedded in Teflon filled with resin. They were ground transversally to their axis so that circular disks were exposed, with diameters ranging from 35 μm to 1 mm. Also, substrates of sputtered copper on silicon wafers were used for experiments where further analysis of the deposit was required. The rms roughness of these substrates is less than one nanometer; the exposed area was defined by Kapton tape masks. In order to monitor the electrode response, high purity wires of Cu or Pt were used as pseudo-***reference electrodes*** (RE) for copper deposition and hydrogen reduction reactions, respectively, given by Eq. (1.1) and (1.3). These were chosen for their small size, to minimize flow perturbation. Their stability and accuracy was successfully tested against conventional AgCl reference electrodes. When using the same material as the working electrode, the values measured by the pseudo-references were highly stable and accurate, making it possible to directly relate them to the overpotential. The ***counter electrodes*** (CE) used in order to produce the auxiliary redox reaction in the cell were made of copper sheet or platinum foil of large areas. In other words, three Cu electrodes were used as WE, CE and RE to study copper deposition from $CuSO_4$ electrolytes, and three Pt electrodes were used as WE, CE and RE to study hydrogen evolution. Both systems proved as stable as with using an AgCl reference electrode, because the chosen reaction to be hosted did not change the state of the surface. Hence, the reading corresponds directly to the overpotential of the reaction.

The electrolytes were made from analytical grade reagents and Millipore water. Unless stated otherwise, they were not deoxygenated. All the solutions contained 1.2 M H_2SO_4, with a copper content ranging from 0.0 to 0.6 M $CuSO_4$. The copper-free solutions were used to study gas formation; the rest to study solid copper growth. A small quantity of 0.25 mM KCl was added to the copper containing electrolytes in order to ensure a fixed range of chloride in all the experiments, since chloride is a strong surfactant present in traces in most copper sulphate reagents which leads to changes in morphology of copper growth.

Due to the hydrodynamic nature of the magnetic field effect on electrochemical processes, it depends on cell geometry. Hence, the experimental cell was designed so that it minimizes turbulence, by using round surfaces and confining the gas-evolving counter electrode to a glass tube, ionically connected by a frit. This cell was used in the main portion of the experiments. When setup constrictions made it necessary, different cells were used provided that the ions electrochemical response was coherent with previous results.

Factors such as cell geometry, relative position of electric and magnetic fields, as well as their position relative to gravity were considered in the design of the experimental setup. In order to avoid turbulence arising from the interaction of the flow with the walls, a cylindrical cell with hemispherical bottom was chosen, allowing any generated convection to continue its trajectory without major alteration due to cell geometry.

Hydrodynamic perturbations due to the counter electrode reaction were also avoided. The half reaction occurring at the Pt counter electrode surface is water oxidation, which produces gas oxygen. Bubbles evolving from the anode generate a stream whose convection was isolated by placing the counter electrode inside the tube ionically connected with the solution by a frit.

The cell electrodes are positioned facing each other by the use of control guides which allow observing their relative orientations and hence the electric field position relative to the magnetic field. In most of the experiments, the fields are located in mutually orthogonal positions.

The cell size is compatible with uniform field generators. As uniform fields can usually be applied only in reduced volumes, cell dimensions were adjusted accordingly. It contains a volume of electrolyte up to 100 mL, and has an external diameter of 5 cms, and fits into the gap between the poles of the electromagnet or in the bore of the vertical superconducting magnet. Figure 2.1 shows a scheme of this cell.

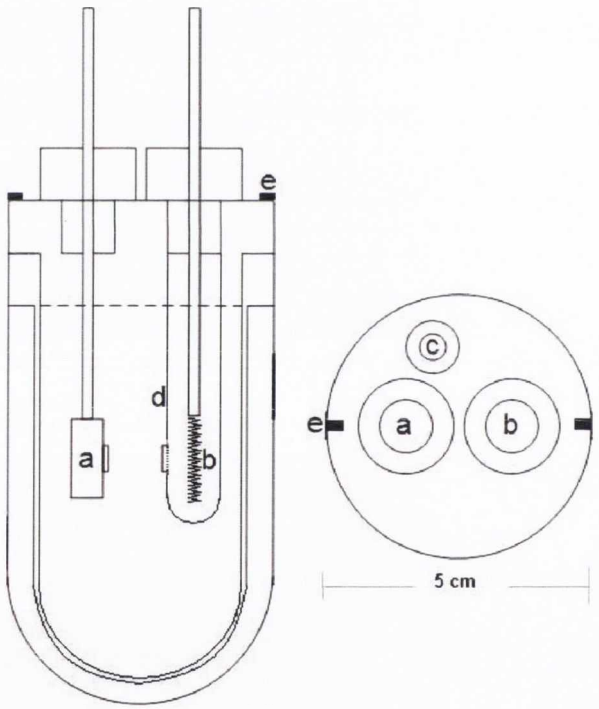

Figure 2.1: Scheme of the magnetoelectrochemical cell used: (a) working electrode, (b) counter electrode, (c) reference electrode, (d) tube with frit connection, and (e) position guides.

II.1.2 Electrochemical devices

Two models of ***potentiostats/galvanostats*** were used, EG&G PAR 273A and Solartron SI 1280B. Scans of potential were applied to the working electrode to characterize the systems. The potentiostatic mode was used to maintain a constant voltage value between reference and working electrodes, by applying the necessary polarizing current between counter and working electrodes. The galvanostatic mode was used to supply a constant current to the working electrode, independent of voltage and impedance changes at the electrode surface.

In selected experiments, analysis of the ***electrochemical noise*** was carried out. The analogue output of the potentiostat was in these cases fed directly to a SR560 voltage preamplifier (Stanford Research Systems), serving as an anti-aliasing filter. A computer controlled by a Labview program with a DAQ card (National Instrument M6250) working at a sampling frequency up to 100 kHz was used to record time sequences. The noise spectrum was obtained by Fourier transforming the digitised time-domain signal.

An ***electrochemical quartz crystal microbalance*** (EQCM) was used in order to follow the mass changes during experiments producing simultaneously gas and solid phases. This accurate technique is very useful when gain or loss of material occurs along with the reaction. The principle is based on the piezoelectric properties of a slice of quartz crystal, where an alternating applied voltage produces resonant vibration of the plate. The frequency of oscillation is sensitive to mass changes on the crystal surface. Thanks to this property, the system functions as an accurate microbalance, since the amount of molecules bound on the sensitive area of the crystal can be quantitatively measured as a decrease of the resonant frequency. This device was used to follow

the current efficiency when copper metallization proceeded along with hydrogen gas formation.

Figure 2.2(a) shows a scheme of a typical piezoelectric quartz crystal with a scheme of the shear horizontal vibration. The thin plate of quartz is coated with metal electrodes on both sides and is inserted in a holder for simplified manipulation and connection to measuring systems.

The EQCM used consists of a Hameg HM8122 Counter Timer, a Maxtech Ltd. resonator model PL-70 and Testbourne Ltd. 5 MHz gold-plated 25 mm diameter quartz crystals. The frequency response was monitored using a Labview program. The current and microbalance frequency were recorded as a function of time, and the impedance matching method was used to calculate the change in mass [61]. The copper current was extracted from the change in mass via:

$$I_{Cu} = \frac{dm}{dt}\frac{nF}{m_{Cu}} \tag{2.1}$$

where dm/dt is the time derivative of the measured mass, $n = 2$ is the number of electrons transferred, F is Faraday's constant and m_{Cu} is the molar mass of the depositing ion.

Rotating disk electrodes are typically used in experiments where convection is an important aspect of the study. This type of electrode was used to obtain deposits under a *mechanically induced convection* regime, for selected cases. The resulting morphology was compared with those obtained under magnetoconvection. The hydrodynamics of a rotating disk electrode is very well known; the current is described by Levich:.

$$j_L = 0.62\, nFAD^{2/3}\omega^{1/2}v^{-1/6}C \tag{2.2}$$

where j_L is the Levich current, n is the number of electrons transferred in the half reaction, F is the Faraday constant, A is the electrode area, D is

the diffusion coefficient, ω is the angular rotation rate of the electrode, ν is the kinematic viscosity and C is the species concentration. The size of the disks used is 7 mm in diameter, rotating at rates up to 900 rpm.

These electrodes consist of a disk of the electrode material surrounded by an insulating material, they can be made from wire or rods sealed in glass, Teflon or any suitable resin. It is very important that there is no leakage of the solution into the electrode mantle between the electrode material and the insulator. One end is ground smooth perpendicular to the axis, while the other end is electrically connected by means of a brush contact. The rod is attached to a motor and is rotated at a certain frequency. Figure 2.2(b) shows a scheme of the velocity profiles obtained at the RDE.

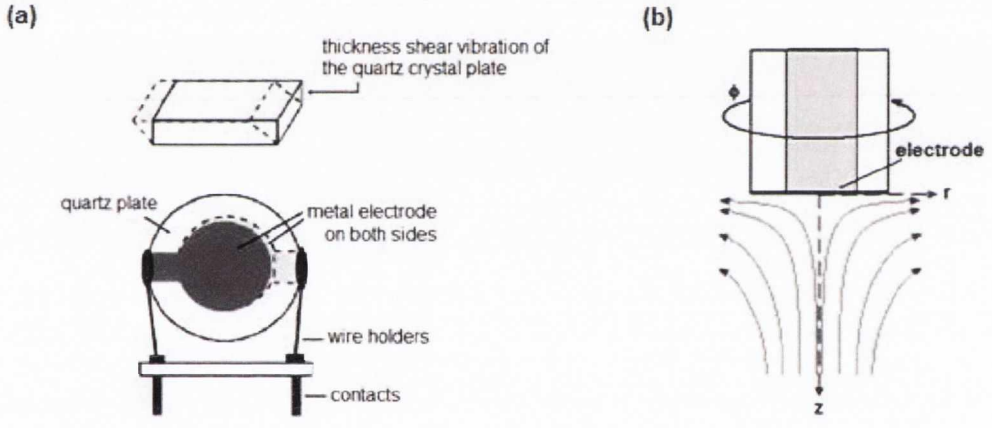

Figure 2.2: Scheme of (a) quartz crystal working electrode, and (b) flow in a rotating disk electrode.

II.1.3 Magnetic devices

During the measurements, the cell was located within a volume where uniform magnetic fields were applied. The devices producing such fields, with better than 1% of non-uniformity, were an electromagnet and a superconducting magnet. Unless stated otherwise, the fields were applied orthogonal to the main proportion of the current, i.e. parallel to the electrode surface.

A water-cooled ***electromagnet*** producing horizontal fields up to 1.5 T was used. The working volume is located between 200 mm pole faces with a 60 mm gap. Figure 2.3(a) shows a scheme of an electromagnet. They consist of a magnetic circuit composed by a yoke and two cores made of high permeability carbon steel. Two coils of wire having hundreds to thousands of windings are allocated around the cores. The pole caps produce a magnetic field in the gap, whose intensity depends on the current passing through the coils, the permeability and saturation induction of the core and the physical dimensions of the magnetic circuit, particularly the gap distance. The maximum current used is limited by the insulation of the copper wire used for making the coils. The coils, which are connected in series, are water cooled in order to avoid damage of the insulating copper wire. Figure 2.3(b) shows the actual electromagnet used.

A cryocooler-cooled "Cryogenics" ***superconducting magnet***, producing vertical fields up to 5 T was also used. The working volume is at room temperature and corresponds to the bore of the magnet, a cylinder of 100 mm in diameter and ~300 mm high. Superconducting magnets can apply high fields in a large volume for long periods of time. They require liquid helium or a helium refrigerator to maintain the superconducting state. Some magnets have a superconducting wire switch connected in parallel, which is heated to maintain the normal

state during the magnet excitation. The magnet is excited by the use of a power supply to increase the current going through it. At the regulated current, the switch is cooled to the superconducting state and the current circulates in the superconducting circuit including the magnet. This is the persistent-mode operation, where the field remains perfectly stable. Figure 2.4(a) shows a schematic cross section of a superconducting magnet, and the equipment used is seen in (b).

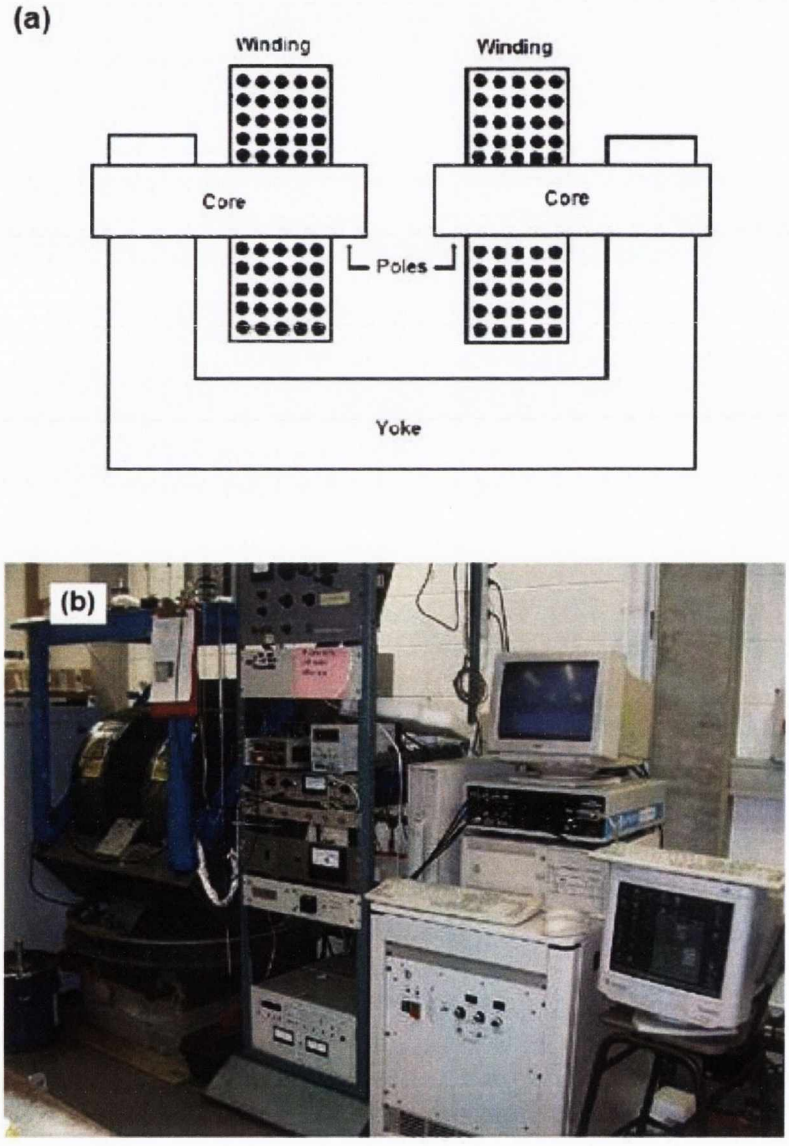

Figure 2.3: (a) Scheme of an electromagnet. (b) Picture showing the equipment setup used in most of the experiments with horizontal fields up to 1.5 Tesla.

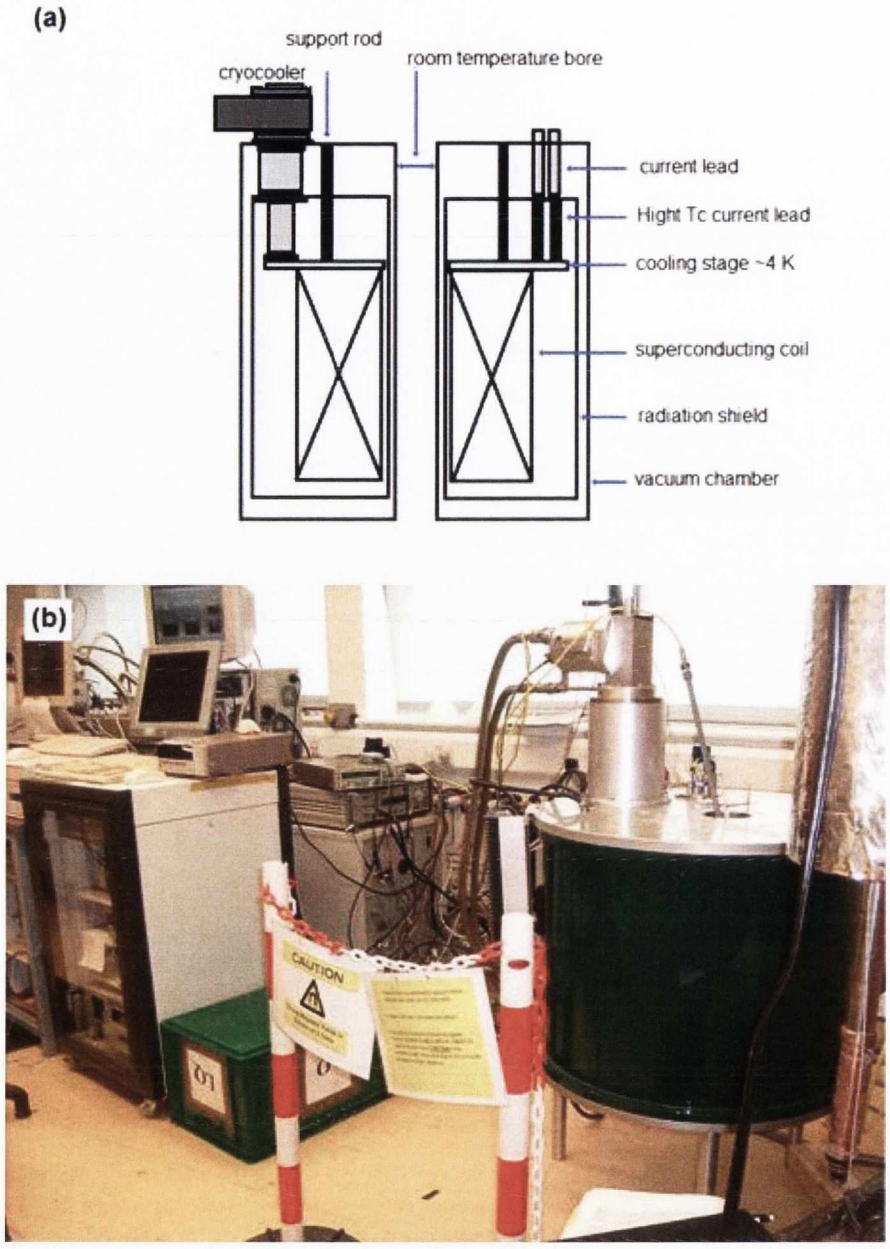

Figure 2.4: (a) Scheme of a cryocooler–cooled superconducting magnet. (b) Picture of the superconducting magnet used in this study, and the annexe equipment setup.

II.2 Characterization techniques

Scanning electron microscopy (SEM) was used to characterize growth morphology at high magnifications up to 50,000 times. It uses a focused beam of high-energy electrons to generate a variety of signals at the surface of solid specimens. Accelerated electrons in a SEM carry significant amounts of kinetic energy, and this energy is dissipated as a variety of signals produced by electron-sample interactions when the incident electrons are decelerated in the solid sample. Figure 2.5(a) sketches these interactions. The signals include secondary electrons (that produce SEM images), backscattered electrons (BSE), diffracted backscattered electrons (EBSD that are used to determine crystal structures and orientations of minerals), photons (characteristic x-rays that are used for elemental analysis and continuum x-rays), visible light (cathodoluminescence-CL), and heat. Secondary electrons and backscattered electrons are commonly used for imaging samples: secondary electrons are most valuable for showing morphology and topography on samples and backscattered electrons are most valuable for illustrating contrasts in composition in multiphase samples (i.e. for rapid phase discrimination). Bidimensional images display variations in these properties within a specific area. Typically, areas ranging from approximately 1 cm to 5 microns in width can be imaged in a scanning mode using conventional SEM techniques (magnification ranging from 20x to approximately 50kx, spatial resolution of 50 to 100 nm). SEM analysis is considered to be "non-destructive"; that is, x-rays generated by electron interactions do not lead to volume loss of the sample, so it is possible to analyze the same materials repeatedly.

While the scanning electron microscope uses a focused beam of electrons to image the sample in the chamber, in a Focused Ion Beam instead of electrons, ions are used, usually Gallium. In this, Ga metal is placed in contact with a tungsten needle and heated. Gallium wets the

tungsten, and an electric field (greater than 10^8 volts per centimeter) causes ionization and field emission of the gallium atoms. Source ions acceleration can yield energies of 5 - 50 keV. The equipment can produce a spot size of a few nanometers. When the high-energy gallium ions strike the sample, they sputter atoms from the surface. Due to this reason, the technique is considered to be "destructive". Focused ion beam was used during this study to produce thin cuts on selected magneto-electrodeposited samples to have a side view. FIBs are sometimes incorporated in systems with both electron and ion beam columns, allowing the same feature to be investigated using either or both beams. This is the case of one of the equipments utilized in this investigation, a FEI Strata 235 FIB dual-beam system. The chamber and annexe equipment setup are shown in figure 2.5(b). A second tool used for SEM characterization was a Zeiss Ultra Plus scanning electron microscope.

In some cases, focused ion beam (FIB) was used during this study to produce thin cuts on selected samples to have a side view. The chamber has integrated an energy dispersive spectroscopy (EDS) system, which is used to find the chemical composition of materials from a spot size of a few microns, and to create element composition maps over a much broader area. In this study, area and line scans of x-ray diffraction patterns were performed on certain samples.

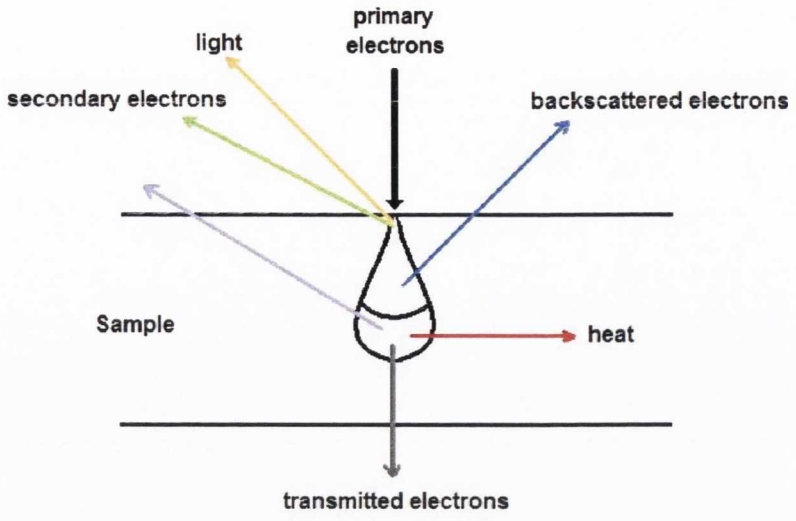

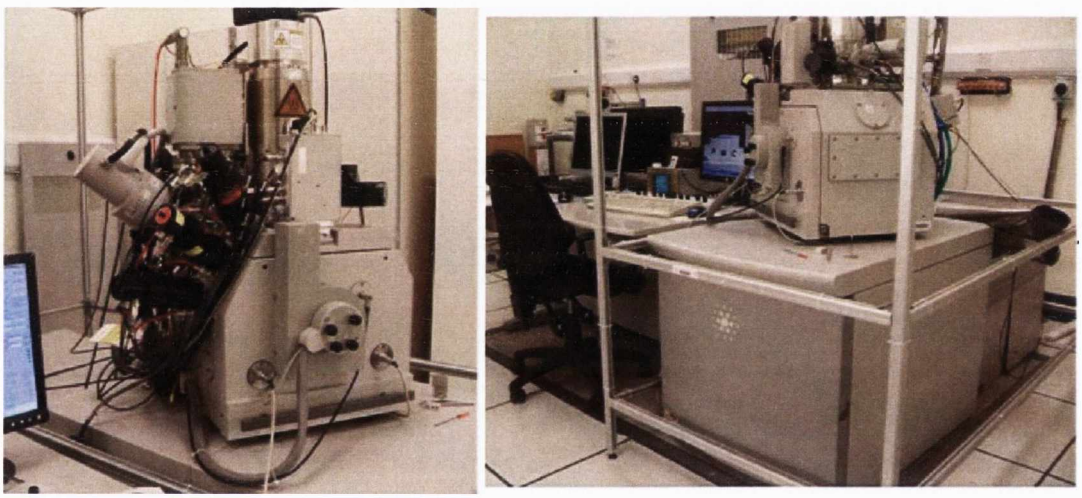

Figure 2.5: (a) Scheme of the beam interaction with a sample. (b) SEM-FIB Strata 235, one of the tools used.

Surface ***profilometry*** characterization was also performed across some samples. The equipment used for this purpose was a Dektak 6M Stylus profilometer. It applies the cantilever principle – schematized in figure 2.6 – in order to obtain data in the *x*-*z* axes, i.e. horizontal distance versus height. The bi-dimensional plot represents the thickness of the sample, provided that the base level is measured as well. The height differences that can be resolved are on the nanometer scale. Figure 2.7 shows the device used.

Atomic force microscopy (AFM) is a technique where the cantilever principle is used as well. In this case, a microcantilever which has a nanometer size tip is used, and Van der Waals, capillary, chemical bonding, electrostatic, magnetic or solvation forces, among others, are in play. The deflection is typically measured by laser detection, and a feedback mechanism is employed to adjust the distance between the tip and the sample by maintaining a constant force between them. The sample is generally mounted on a piezoelectric tube, which moves the sample in the *z* direction for maintaining a constant force, and in the *x* and *y* directions for scanning the sample. As a result, the tri-dimensional information represents the topography of the sample. The characteristics of the scanner and the forces involved allow resolution in the nanometer range, with scanned areas from tens of nanometers to tens of microns. In this study, the equipment used is a Nanoscope III instrument, and data collection is performed in tapping mode.

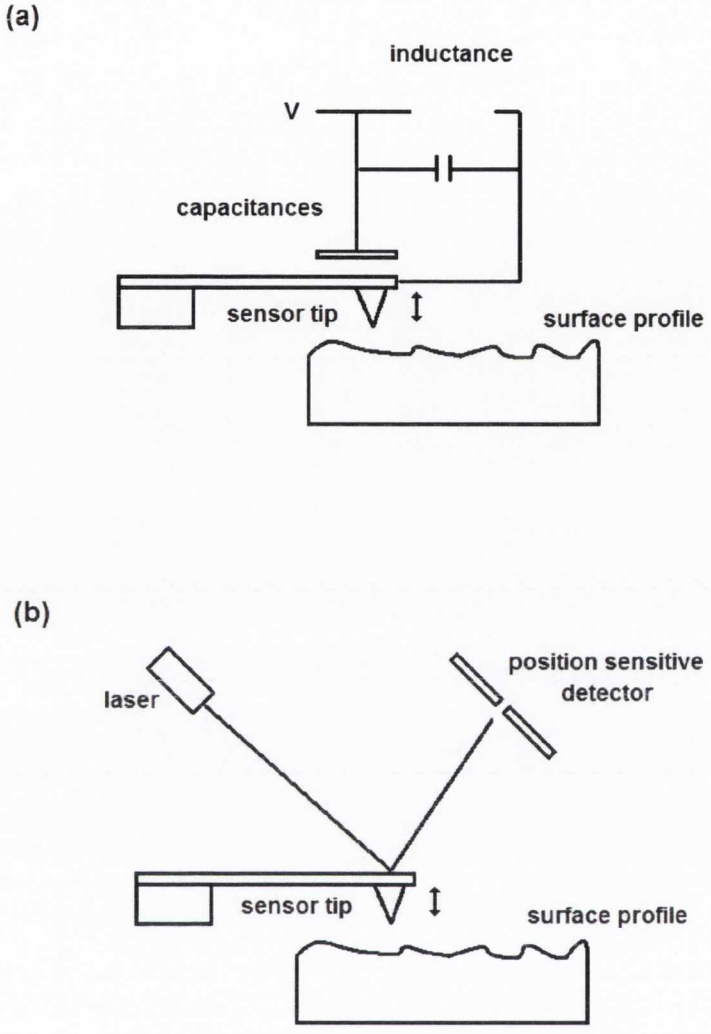

Figure 2.6: The cantilever principle, showing the basic principle of profilometry, with detection of the sensor tip movement by: (a) capacitance measurement, and (b) laser deflection.

Figure 2.7: Dektak stylus profilometer used during this investigation. (a) View of the profilometry chamber, (b) view of the equipment setup, with its pneumatic optical table and controlling units.

Scanning white light interferometry, SWLI, is a non-contact technique which produces tridimensional information from a pattern of bright and dark lines (fringes) resulting from an optical path difference between a reference and a sample beam. Typically, magnifications range from 0.5x to 100x, providing sub-nanometer resolution.

These instruments use broadband sources together with mechanical translation of the object or reference surface to measure large discontinuous surface features. A piezoelectric actuator is used to translate the object in a direction parallel to the optical axis of the interferometer over an interval of several tens of micrometers. Incoming light is split inside the interferometer, one beam going to an internal reference surface and the other to the sample. After reflection, the beams recombine inside the interferometer, undergoing constructive and destructive interference and producing the light and dark fringe pattern. When the part is in focus the interference contrast is maximum. The surface topography is measured by calculating the fringe contrast as a function of scan position and then relating the point of maximum contrast to a surface height for each pixel in the image. By collecting this information point by point, a 3D map of the sample surface can be obtained. Figure 2.8(a) schematizes the functioning principle of these equipments and in 2.8(b) a picture of the device used is seen.

SWLI is a very useful and fast acquisition technique, especially for extended areas. The equipment used was a Zygo 100, utilized to characterize surface roughness of selected copper samples grown under magnetic fields.

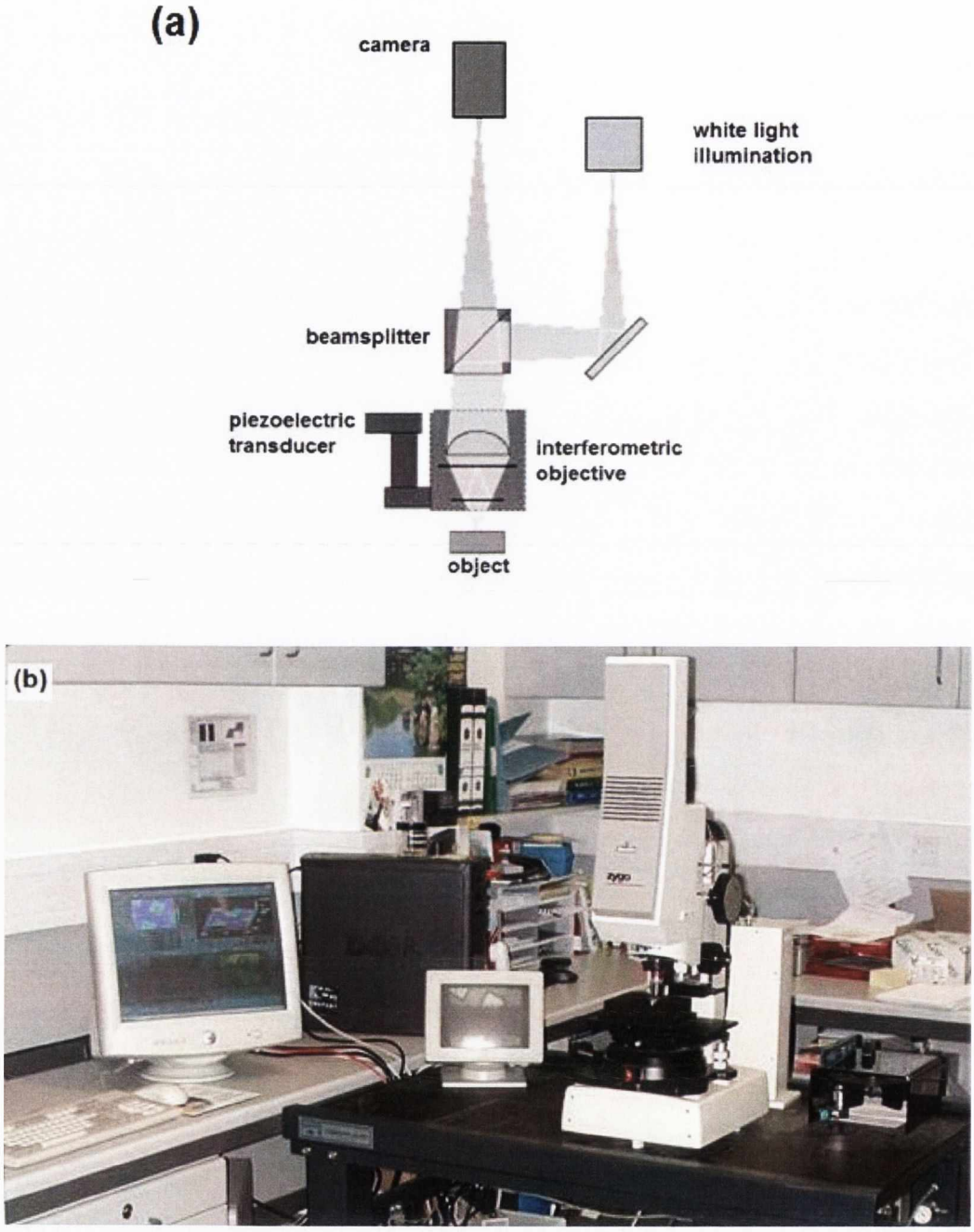

Figure 2.8: (a) Scheme of the functioning principle of a scanning white light interferometer. (b) Picture of the device used.

The study of bubbles growth was followed simultaneously by electrochemical and in situ-optical techniques. For ***bubbles visualization*** images were taken using a Pico 1200 hs high speed monochrome camera with frame rates up to 30 fps and 600 fps. Magnifications between 3.5 and 5.2 were achieved using a Sigma 180 mm 1:3.5 Alp Macro DG lens in conjunction with 140 mm macro bellows. The hydrogen bubbles were illuminated from behind using either a PHLOX planar backlight or Fiber Light DC-950 light source with attached fiber optic cable in conjunction with a diffusion plate, dependent upon the magnetic field strength used. The resulting greyscale images were analysed using ImageJ. Figure 2.9 shows the devices used for the optical setup.

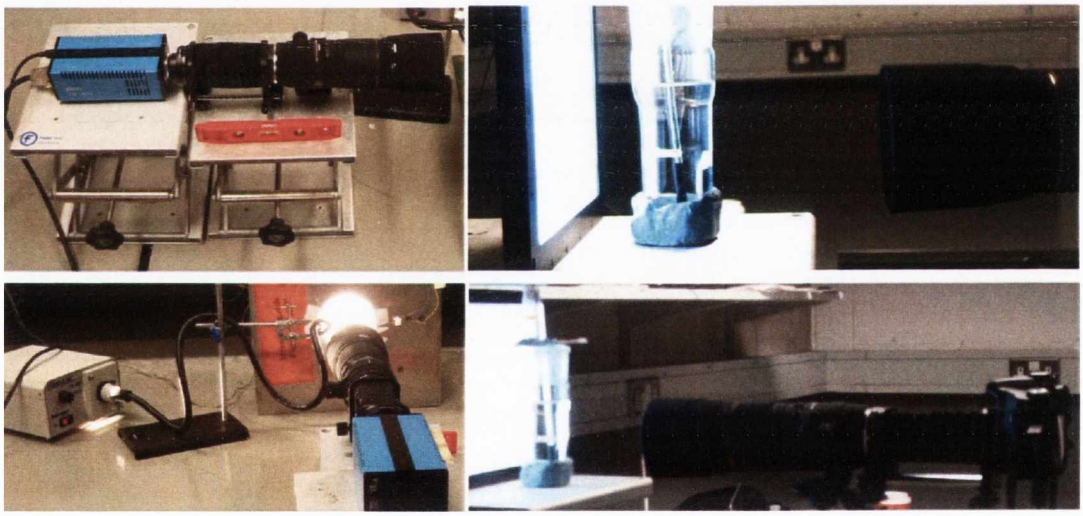

Figure 2.9: High speed camera, macro lens, fiber optic light source with diffusion plate and planar backlight, used to follow the growth of bubbles.

Analysis of the **electrochemical noise** (EN) was performed for certain experiments. The Fast Fourier Transform (FFT) and the power spectrum are powerful tools for analyzing and measuring signals from plug-in data acquisition (DAQ) devices. FFTs and the Power Spectrum are useful for measuring the frequency content of stationary or transient signals. FFTs produce the average frequency content of a signal over the entire time that the signal was acquired. An FFT produces a discrete frequency spectrum. The continuous, periodic frequency spectrum is sampled by the FFT.

Because of noise-level scaling with Δf, spectra for noise measurement are often displayed in a normalized format called **power or amplitude spectral density** (PSD). This normalizes the power or amplitude spectrum to the spectrum that would be measured by a 1 Hz-wide square filter, a convention for noise-level measurements. The level at each frequency line then reads as if it were measured through a 1 Hz filter centered at that frequency line.

$$Power\ spectral\ density\ = \frac{Power\ \ spectrum\ \ in\ V_{rms}^2}{\Delta f\ \times Noise\ \ power\ \ bandwidt\ h\ of\ window} \tag{2.3}$$

Power spectral density is thus computed as:

$$PSD\ \equiv \frac{V_{rms}^2}{Hz}\ or \frac{V^2}{Hz} \tag{2.4}$$

and is used to characterize events occurring at specific or broad ranges of frequencies.

Chapter III

Magnetic field effect on the electrochemical response

This chapter describes the changes induced by uniform magnetic fields on the electrochemical response when cathodic processes take place in the acid copper system.

The effect of electrolyte concentration, field intensity, gravity and electrode area are studied. Potentiodynamic and potentiostatic techniques are used to characterize the system's response. The field effect on the cathodic reaction is analyzed when the system is under activation, mixed or diffusion-limited control.

III.1 Effect of concentration and field intensity

The acid copper system was characterized by using linear sweep voltammetry (LSV), at scan rates of 0.2 mV s^{-1}. In this case currents are plotted on a logarithmic scale to expand the lower values. Figure 3.1 shows families of curves illustrating the concentration influence on the current and the field effect on them. In the left panel (0 T), the acronyms OCP, ACT, MIX, DIF and HER indicate, respectively, the location of the open circuit potential, the zone of control by activation, zone of mixed activation-diffusion control, zone of diffusion control and the region where hydrogen evolution reaction occurs.

At low overpotentials, where charge transfer for copper electrodepositionoccurs at rates lower than that of ions transport from the solution bulk to the electrode surface, the change of concentration does not make a difference on the measured current. This area is activation controlled (ACT). The zone is estimated to extend from the open circuit potential (OCP) to the point where a first inflexion of the η-j curve is observed.

The curves present a current plateau at high overpotentials, corresponding to the diffusion limited zone (DIF). Here, the reaction rate is dominated by ions transport to the cathode surface. The higher copper concentration plots in (a) do not exhibit constant current values for the diffusion limited zone. This has a two-fold explanation: firstly, there is high availability of ions at the electrode surroundings and, secondly, there is also an increase of the real surface area during the reaction. This is addressed in further sections.

The zone between the areas marked as (DIF) and (ACT) corresponds to the mixed control zone (MIX), and appears when the relative rates between charge transfer and ions access to the surface of reaction are rather similar. In these cases, an increase of the electrolyte

concentration reduces the relative contribution of mass transport to the rate limitation. This can be seen from the plots as an increase on current density, in proportion to the electrolyte concentration.

At the left end of these curves, corresponding to overpotentials beyond the diffusion controlled zone, hydrogen evolution reaction (HER) starts to occur along with copper reduction. The contribution of this secondary reaction to the current is evident from the curves.

When a magnetic field of 1.5 Tesla is applied, Figure 3.1(b) all the curves exhibit changes in current. Shifts of the measured values due to the field are seen at almost all overpotentials but are more evident in the plateau zone. This is consistent with the fact that, except within the activation zone, copper reduction proceeds under at least some degree of mass transport limitation. Hence, increases of current are expected when convection is established. Diluted electrolytes still present plateaus, although with higher current values. The concentrated ones do not.

A clearer visualization of the concentration-related field effect is seen in (c). The graph shows shifts in limiting current (for $\eta = 0.5$ V) as a function of copper content of the solution, when fields of 0.5 and 1.5 Tesla were applied. The currents are increasingly enhanced with copper concentration, until a maximum is reached between 0.2 and 0.3 M $CuSO_4$. For higher concentrations, the field has less effect on current values. This is consistent with an improvement of mass transport conditions when the copper content in the electrolyte is increased. In other words: since a more concentrated electrolyte reduces mass transport limitation such systems are less prone to show effects related to mass-transport enhancement.

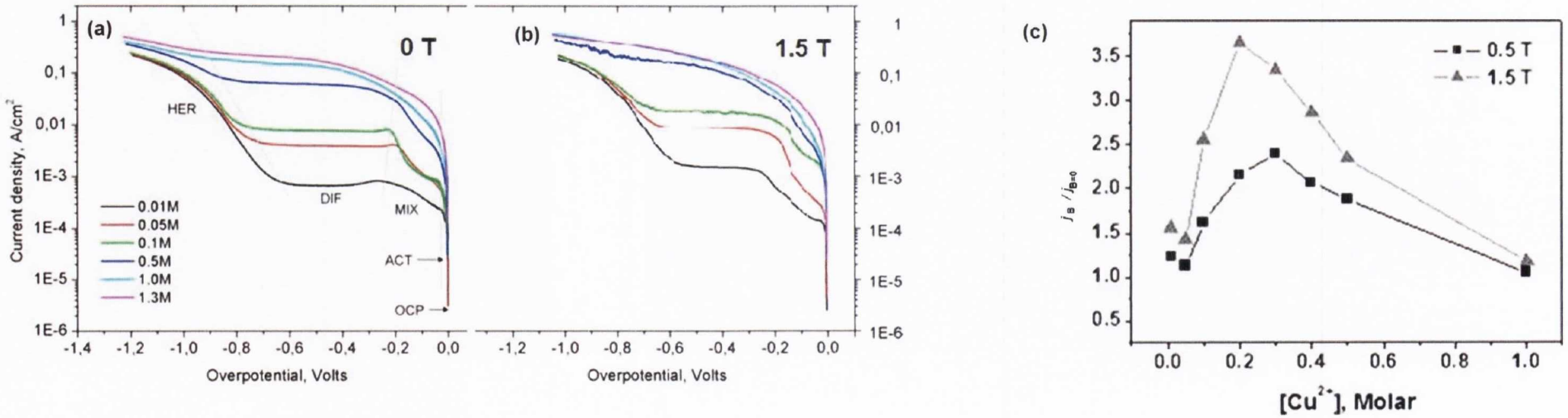

Figure 3.1: (a) Linear sweep voltammograms showing copper deposition from acid copper sulphate electrolytes on Cu substrates at 0 T and 1.5 T. The family of curves show the effect of copper concentration on the current. Scan rate: 0.2 mV s^{-1}. (b) Field-induced enhancement of the limiting current at $\eta = 0.5$ V, as a function of electrolyte concentration, for 0.5 T and 1.5 T.

.

The next step was to evaluate the extent of the field-induced enhancement on the reaction rate, for fixed electrolyte concentration and variable field intensity. A concentration near the enhancement peak was chosen. Figure 3.2(a) shows voltammograms measured using a 0.3 M $CuSO_4$ electrolyte and magnetic fields up to 5 Tesla. It is seen that the variation tends to saturate above 3 Tesla. According to the relation given by Eqns. (1.12) and (1.13), the current delta is a function of concentration and field intensity in the form of a power law, which saturates at higher fields. Figure 3.2(b) shows points based on the experimental data.

Changes in current were also evaluated at overpotentials other than the transport limited zone. For instance, current shifts at the mixed region are also observed. They are expected since there is a component of mass transport limitation in this zone. Figure 3.3 shows the field-induced current shift as a function of electrolyte concentration evaluated at different overpotentials. At η = 1.2 V (HER zone), big changes in current are observed. In this case, two reactions take place simultaneously: copper and hydrogen reduction. The field effect on each is examined in further sections. At overpotentials 600 and 400 mV (DIF zone), the field-induced enhancement of the current is similar to that shown in figure 3.1(b). This is expected, and corresponds to the improved access of copper ions to the electrode surface.

At overpotentials 300 and 200 mV (MIX zone), there is less change in current. However, it still is present, and this is valid for all ranges of electrolyte. The changes correspond, as in the previous case, to an improved access of ions to the reacting surface. However, as in this zone only a fraction of the rate is transport-controlled, a lower fraction of the current changes under field influence. Interestingly, at η = 80 mV (ACT zone) small changes in current were observed within error, similar to that observed by O'Reilly [39]. A field effect for copper is not expected in this zone. However, as explained in Chapter I, in this zone there is also oxygen reduction (ORR). This is addressed in Chapter VI.

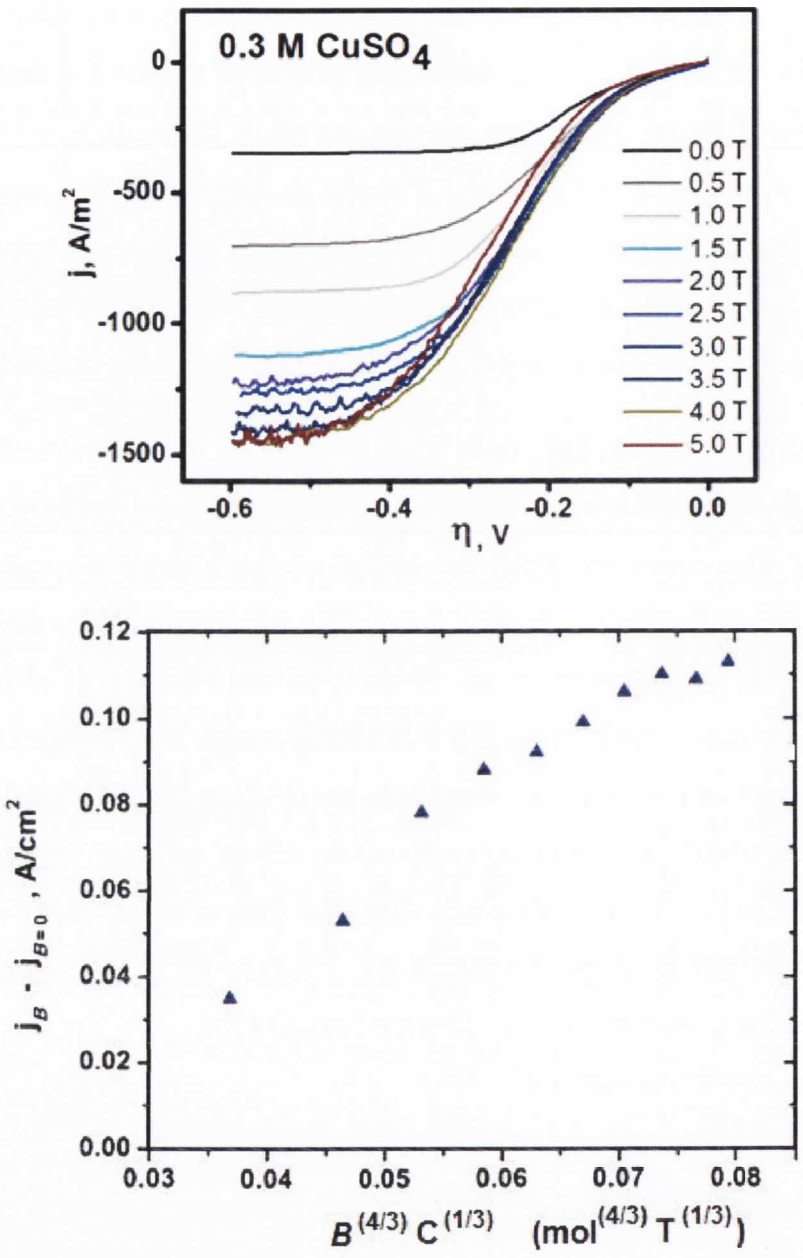

Figure 3.2: (a) Effect of magnetic fields up to 5 Tesla on cathodic voltammograms from a 0.3 M $CuSO_4$ electrolyte. (b) Corresponding changes in current density values as a function of field intensity and electrolyte concentration, following the power law described by the empirical relation $\Delta j_L \propto B^{1/3} C_0^{4/3}$. Fields applied from 0.5 to 5 Tesla.

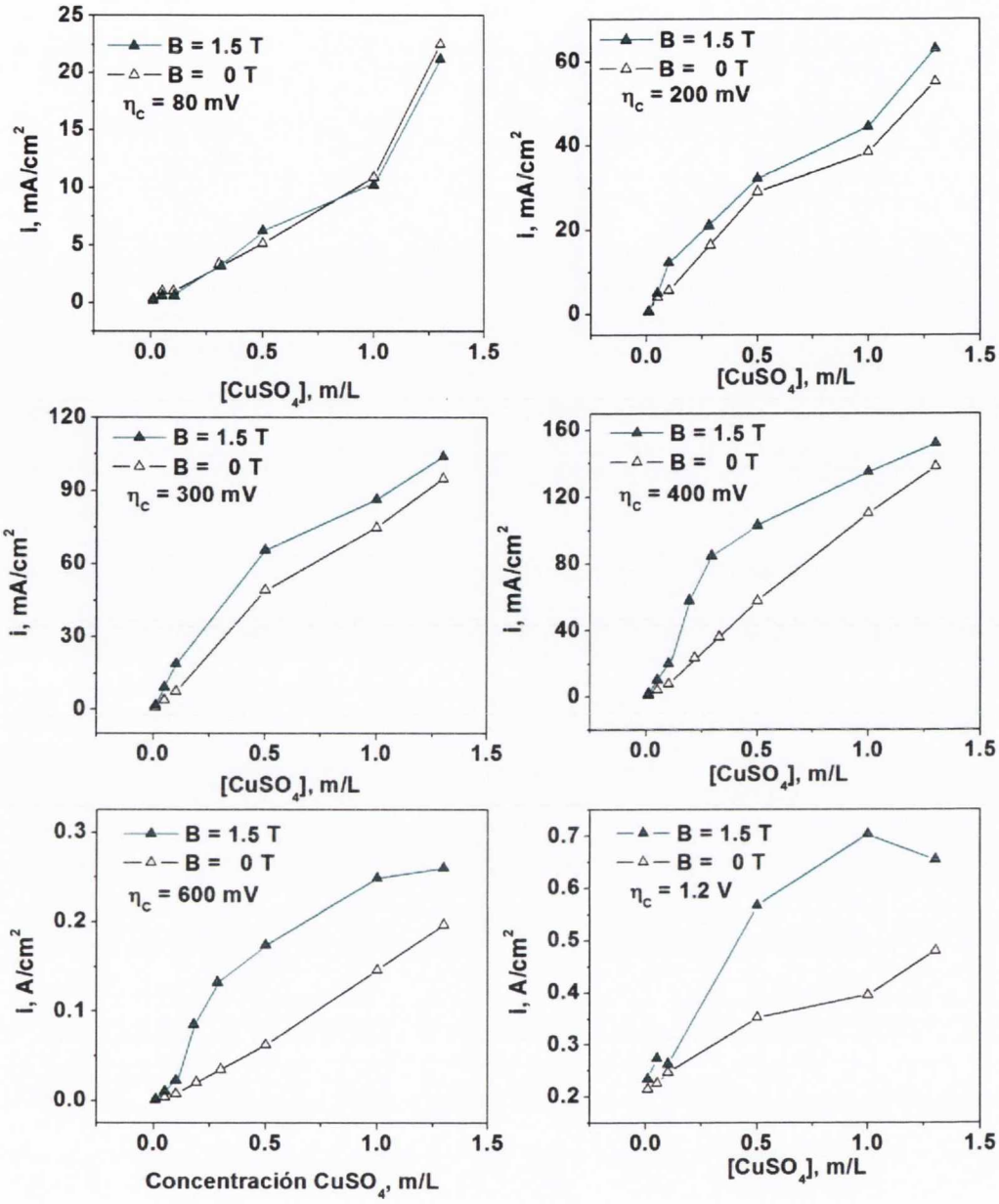

Figure 3.3: Shifts in the absolute value of cathodic current density as a function of electrolyte concentration, for diverse overpotentials, when a field of 1.5 T is applied.

III.2 Effect of gravity

The field effect observed depends also on the electrode orientation with respect to gravity. Figure 3.4 shows the effect of vertical fields for the different electrode positions. Natural convection is known to promote higher ion transport rates towards vertical or facing upwards electrodes, and interaction with fields has been shown [18, 21, 53]. As the graph shows, that is actually the case: the highest values are obtained when the electrode is located horizontally facing up, and the lowest are found for electrodes placed horizontally facing down. Intermediate values are exhibited by vertical electrodes. Interestingly, the differences observed with electrode position are amplified as fields are more intense.

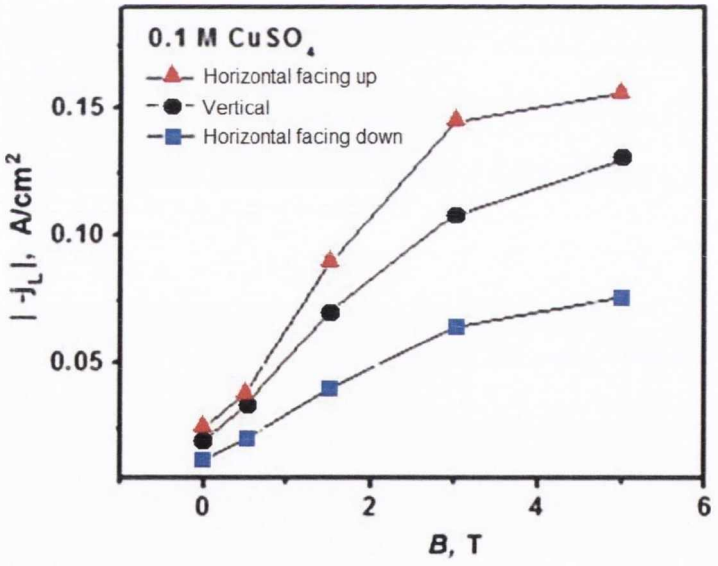

Figure 3.4: Effect of gravity (in terms of electrode position) on the values of the limiting current density obtained when fields up to 5 Tesla were applied vertically.

III.3 Effect of electrode area

Changes in electrode area also lead to variations of the measured current. As mentioned in section I.6, the effect of the area has been taken into account in the models describing changes of limiting current density values due to magnetic fields. Here, two different aspects of the area dependence of the field effect are addressed.

Firstly, the influence of electrode size is evaluated for three different orders of magnitude, from 35 to 5000 μm in diameter. Figure 3.5 shows the increment of current, with respect to its values under no field, as a function of the electrode size. Enhancements between 1.5 and 3.2 times are seen with a field of 1.5 Tesla. The bigger electrodes exhibit the larger relative changes. Direct observation of the experiments allowed us to observe that higher convection was generated when larger electrodes were used; all other conditions kept the same.

Secondly, the real area of reaction is considered. The electrode area is constantly changing during growth, not only in its position and shape but also in magnitude. In consequence, it is the absolute value of reactive area that is relevant. In particular, systems growing under mass transport conditions are known to generate three dimensional deposits with nodular or dendritic structure. The area of these structures evolves with time, increasing as a power law [54]. If the field effect is mainly related to transport-limited conditions, the evolution in time of the real area of a growing system must be considered. Nevertheless, so far no attention to this aspect has been manifest in literature.

Figure 3.6(a) shows an example of the influence of area evolution during magnetoelectrodeposition. In this case the deposits are obtained potentiostatically at η = 500 mV, i.e. the current density ratio is kept at j/j_L = 1. Copper hence grows dendritically. As the chronoamperometry shows, under fields the current increases over time, becoming noisy. The

corresponding amount of charge Q passed is shown in 3.6(b), showing that a linear dQ/dt, seen for 0 T no longer describes deposition under fields. The dotted lines project a linear rate of deposition, from which the curves clearly divert, in proportion with field intensity.

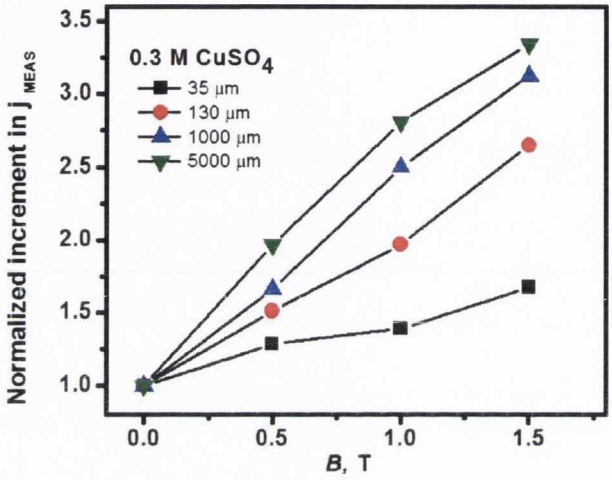

Figure 3.5: Changes in limiting current values as a function of electrode size and flux density.

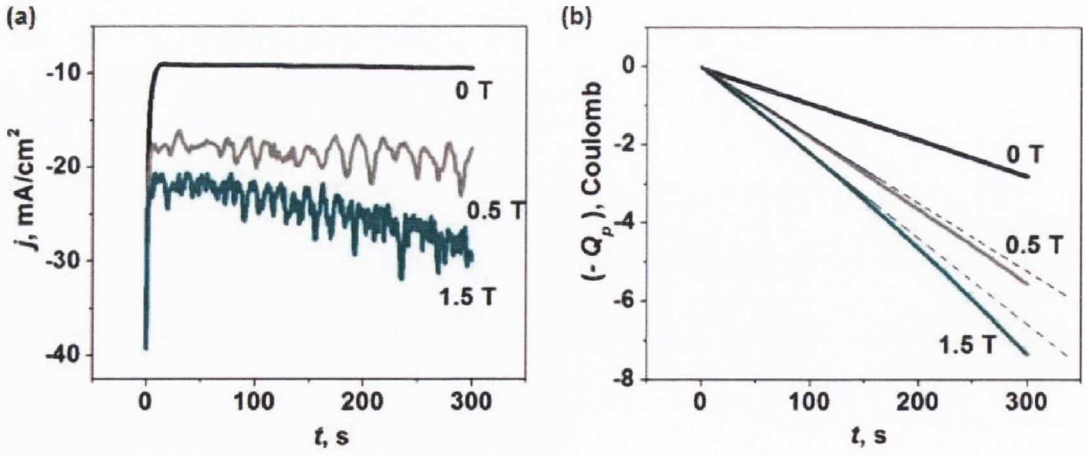

Figure 3.6: (a) Current evolution over time for 0, 0.5 and 1.5 Tesla. (b) Corresponding charge passed. Electrolyte 0.3 M $CuSO_4$.

Figure 3.7 shows an example of linear sweep voltammetry, scanned at 0.5 mV s^{-2}, with a 0.5 M $CuSO_4$ electrolyte. Graphs (a), (b) and (c) show the results obtained with horizontal electrodes facing up, vertical electrodes and horizontal electrodes facing down, respectively. As expected, limited current density decreases progressively at 0 T, from 50 to 40 to 25 mA cm^{-2} in each case. This is due to the convection component introduced by the action of gravitational acceleration on the density gradients in front of the electrode. When the fields are applied, however, all the curves showed almost the same current behaviour, with no visible changes in current among them.

Since the field effect is usually compared with mechanical stirring, measurements with a rotating disk electrode were also performed. Figure 3.7(d) shows the results. It is seen that current response does not behave in exactly the same way, since it appears to reach a limited current density. For increasing angular velocities from 25 to 900 rpm the limited current grows proportionally, between 53 and 77 mA cm^{-2}.

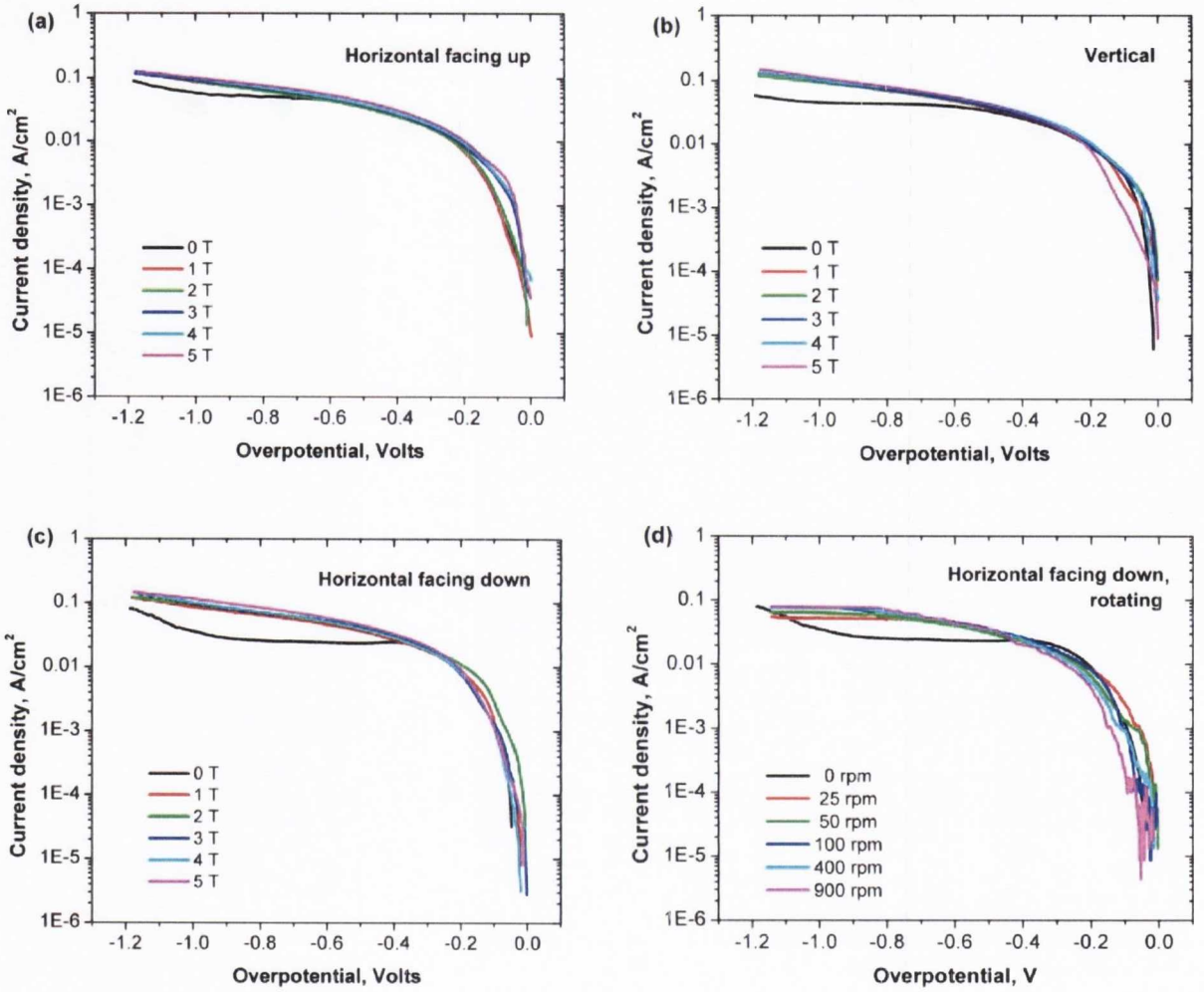

Figure 3.7: Cathodic linear sweep voltammograms showing the effect of convection on the measured current density for a concentrated electrolyte containing 0.5 M Cu^{2+}. The effect of gravity is considered by changing the electrode position: (a) horizontal facing up, (b) vertical, and (c) horizontal facing down. The effect of angular velocity for a rotating disk electrode is seen in (d).

The use of microelectrodes allows potentiodynamic techniques at high scan rates. This is useful to observe any possible fast processes or to overcome resistive behaviour of the electrolyte. In order to evaluate these aspects under magnetic fields, copper microelectrodes of 50 μm in diameter were scanned from the OCP to -1.2 V of cathodic overpotential at a rate of 2 Volts per second. Figure 3.8 displays a series of measurements showing the effect of a 1.3 Tesla field, for increasing copper concentrations. As expected, the responses are more clearly defined, particularly for the 0.5 M Cu^{2+} electrolyte, than they are from the LSVs in figures 3.1 and 3.6.

The behaviour observed is as follows. For instance, when the electrolyte contains 0.2 M Cu^{2+}, under no field (black curve), the forward scan shows a maximum of current around η = 500 mV, which indicates the moment in which reacting ions within the diffusion shell are depleted. This determines the beginning of concentration decay. As the scan goes further, the driving force for reduction increases thus incrementing the rate of ions consumption. At higher overpotentials, hydrogen evolution takes place, increasing the measured current density.

Since for higher electrolyte concentrations the diffusion layer is thinner, a progressive shift of the peaks at 0 T is observed for increasing copper content. This indicates that it takes longer to complete reactants consumption inside the diffusion shell when the electrolyte is more concentrated.

The field effect is similar to that of increasing concentration. For any specific copper content, applying a field (red curves) results in a shift of the corresponding peaks towards more negative values and higher currents, just as observed when concentration increases. This confirms that the diffusion shell thickness, δ , is reduced when magnetic fields are applied.

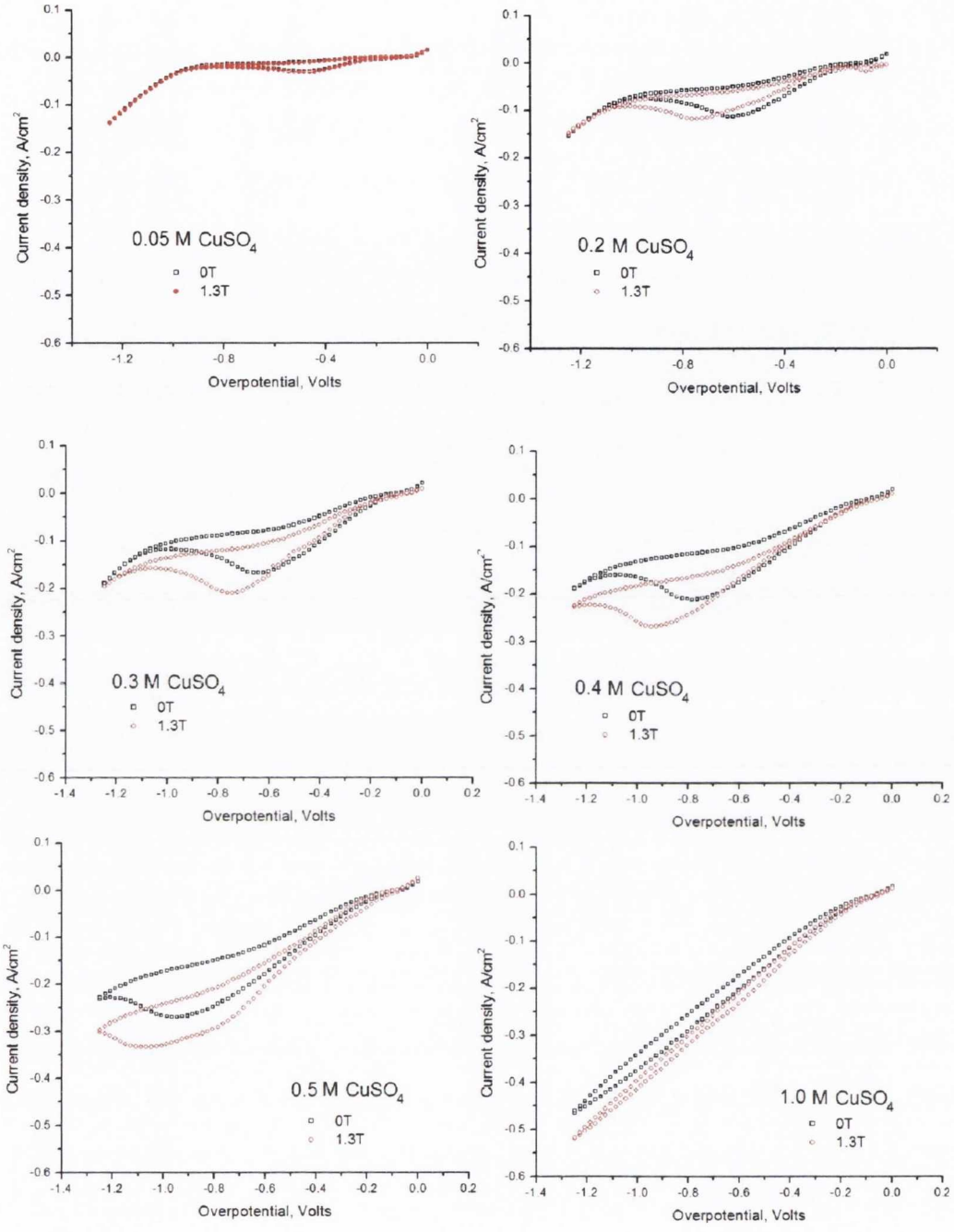

Figure 3.8: Cyclic voltammograms performed at 2 V s^{-1} using microelectrodes of 50 μm in diameter, to show the magnetic field effect on the reactions occurring at different Cu^{2+} concentrations. Field applied is 1.3 T.

III.4 Discussion and summary

The cathodic processes were identified by cyclic and linear sweep voltammetry, for copper concentration ranging from 0.01 M to 1.3 M in acid solutions. Field-induced changes in cathodic current density were identified at all ranges of overpotential, regardless of the rate controlling step. Zones separately identified as ACT, MIX, DIF and HER presented shifts in current when fields were applied.

As expected, the mass transport limitation at the MIX, DIF and HER zones make the system prone to field-induced changes in current. The shifts are proportional to electrolyte concentration, reaching a maximum around 0.2-0.3 M $CuSO_4$. Higher concentrations present progressively lower mass transport limitation and thus the shifts, although exist, decrease in magnitude.

Electrolytes of 0.3 M and lower copper concentration present increments of the plateau-current when fields are imposed, according to the power law given by Eq. (1.13).

The field effect on transport-limited currents changes with the electrode area in two different ways. Firstly, the geometric area of the electrode influences the shift. Electrodes with larger areas present the bigger changes. The effect is amplified in proportion to the field intensity. Secondly, increasing the reaction area promotes an evolving field effect in time, which can be seen as non-linear relation of the charge passed with time. The field effect in evolving areas is difficult to quantify, since:

a. The growing area process changes mass transport limitation condition itself, thus the initially measured j_L value may not represent the system after it starts to grow.
b. The field effect is proportional to the mass-transport limitation conditions.

The field increases currents although they are already affected by gravity. Currents reflect the influence of gravity-induced convection in the order: horizontal facing down < vertical < horizontal facing up. It was seen that fields amplify the values proportionally.

Electrolytes with high concentrations of copper tend to produce ohmic responses under fields. This effect was overcome by using small microelectrodes and high scan rates, and was not observed when a rotating disk electrode was used.

Chapter IV

Magnetic field effect on growth of metallic copper

This chapter describes the growth of solid copper under the field influence. By use of potentiostatic and galvanostatic techniques, the different growth modes are analyzed. Deposits were characterized in terms of morphology, thickness and roughness. Current distribution is discussed according to the combined observations acquired with the different techniques.

IV.1 Deposition under potentiostatic control

IV.1.1 Mixed control conditions

The field effect on electrodeposition is often related to its influence on the diffusion controlled currents. However, for practical purposes, electrochemical deposition is rarely performed in a purely diffusive regime. Most of the times a mixed-control regime is chosen to ensure bright deposits.

Vertical magnetic fields were applied parallel to the vertical electrode surface. In this case, the resulting Lorentz force acts horizontally. An influence of magnetic fields in these conditions is not evident at first sight. Figure 4.1 shows a macrograph where no apparent change is seen on deposits grown under 0 and 4 T, at an overpotential of 200 mV, from a 0.3 M $CuSO_4$ electrolyte. The deposit brightness seems unaffected. In order to quantify this, roughness measurements were performed via SWLI and AFM.

In general terms, atomic force microscopy (AFM) was used for samples with low thickness and roughness, while scanning white light interferometry (SWLI) was used for thicker, rougher deposits. In order to test the equivalence of both methods, one sample with an intermediate roughness was analyzed by both AFM and SWLI. The sample was obtained at -200 mV overpotential during 300 seconds from a 0.3 M Cu^{2+} electrolyte. Figures 4.2 (a) and (b) show the topographic results. The roughness of the sample, measured with AFM is 0.283 μm and 0.273 μm with SWLI, which shows that both techniques have similar accuracy.

Deposits obtained under field were then compared with deposits grown at zero field, potentiostatically controlled at η = -200 mV. Figure 4.3 shows an example. The sample grown at 0 T exhibits a rms roughness of 0.252 μm, similar to the 0.244 mm measured for the sample grown at 1.5 T. No effect of the field on roughness is thus observed.

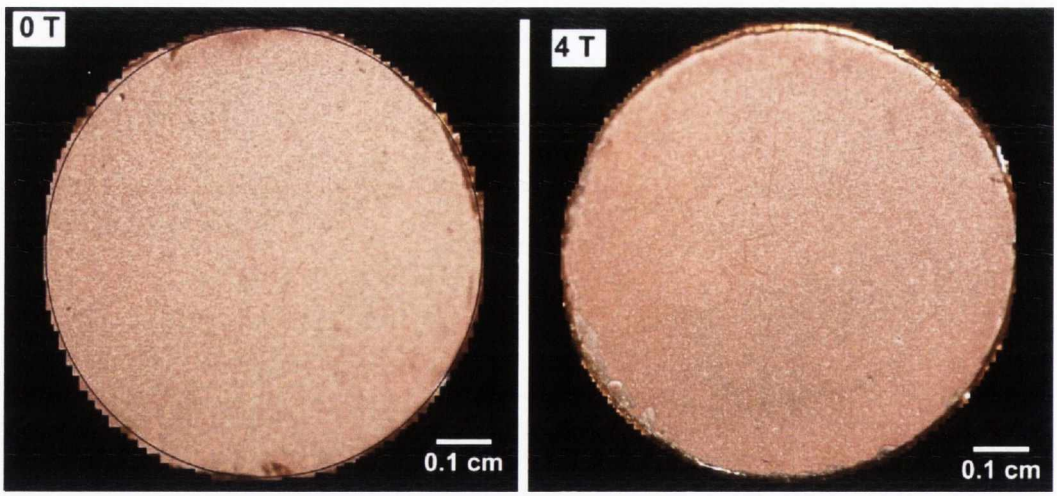

Figure 4.1: Macrograph of samples grown potentiostatically from a 0.3 M $CuSO_4$ electrolyte, at η = -200 mV for 300 seconds, at 0 and 4 T. No evident change is observed. The electrode diameter is 0.8 cm.

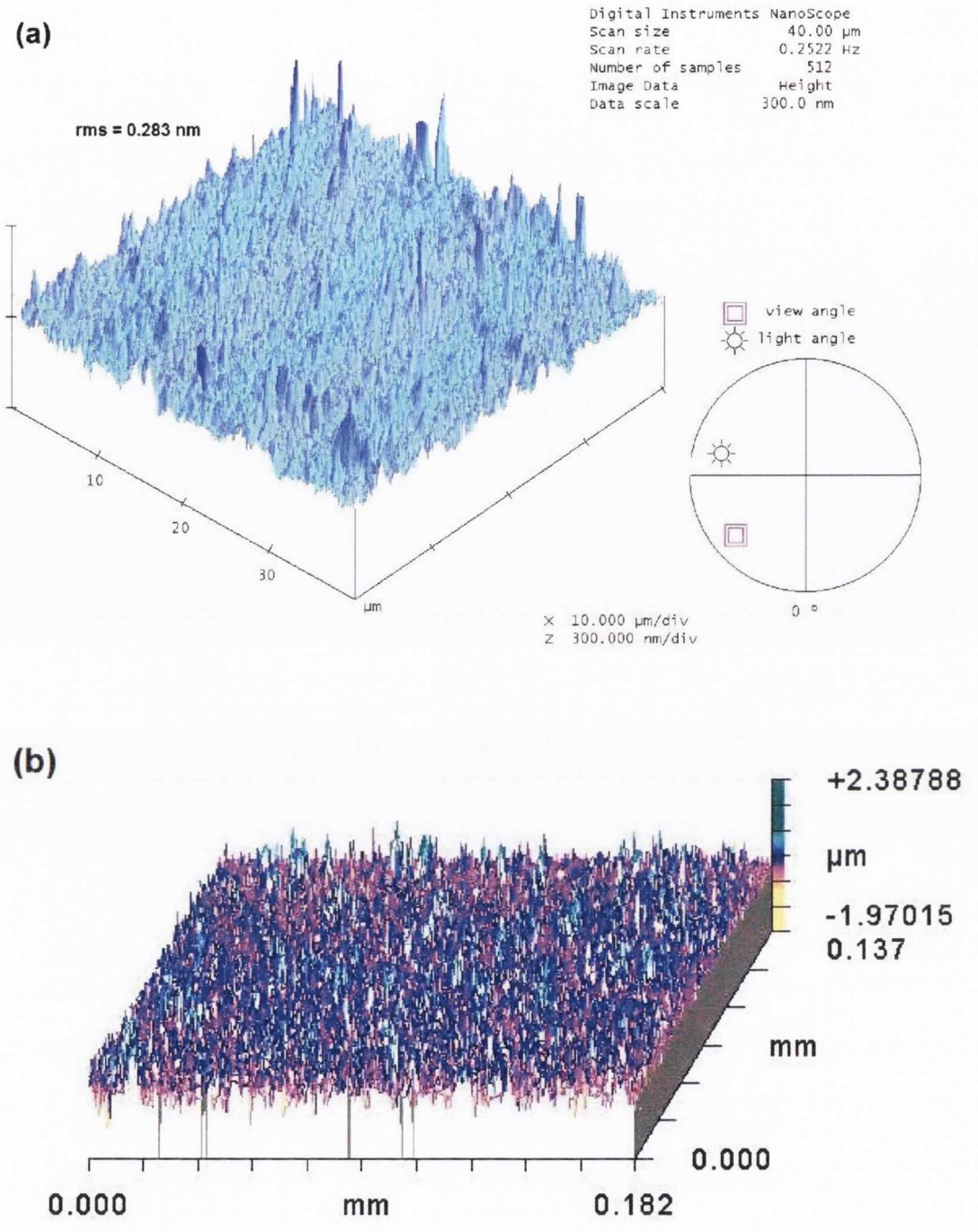

Figure 4.2: Comparative images showing the topology analysis of the same sample, made by (a) AFM and (b) SWLI techniques. Electrolyte 0.3 M $CuSO_4$, η = -200 mV, t = 300 s.

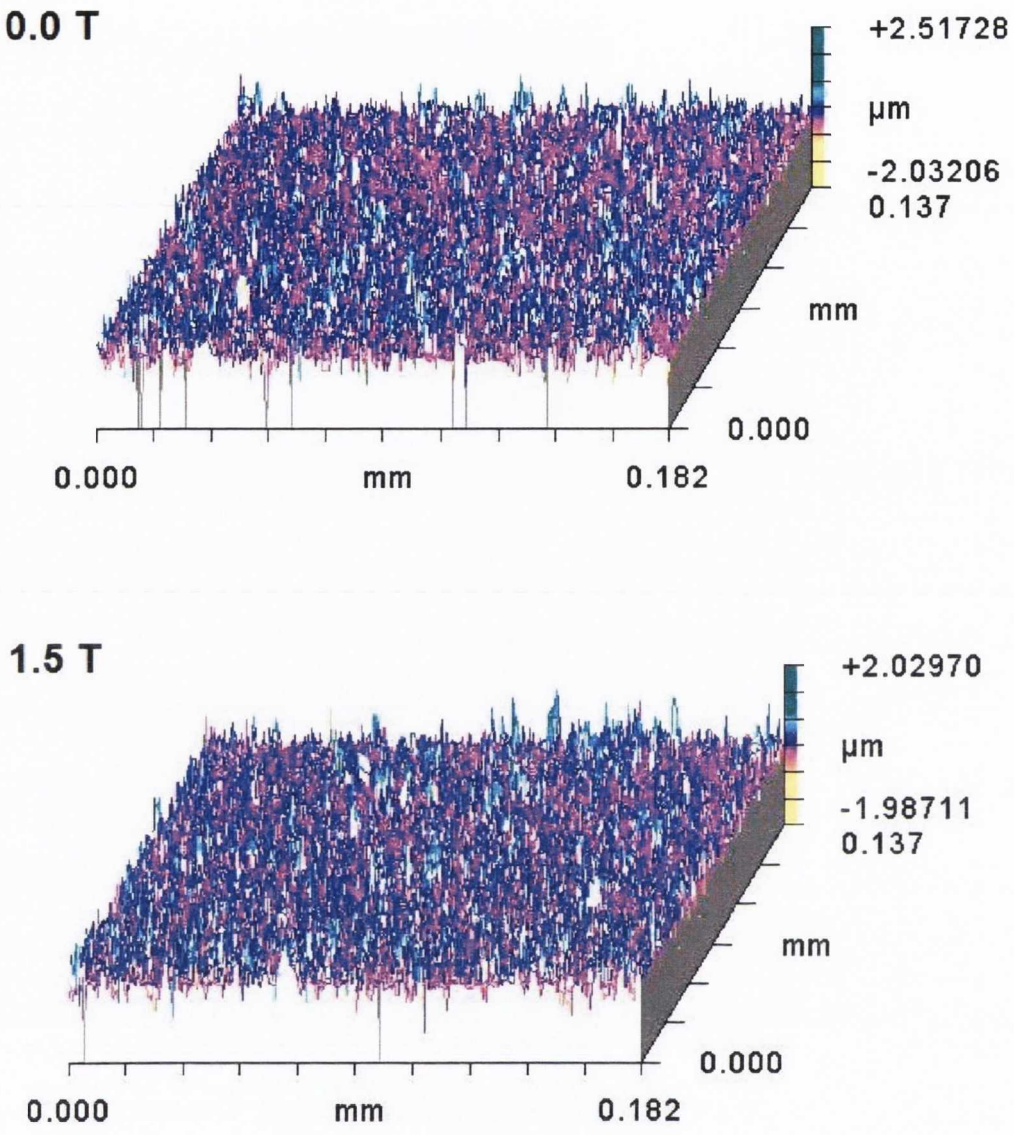

Figure 4.3: Topographic characterization scanning white light interferometry of samples grown potentiostatically from a 0.3 M $CuSO_4$ electrolyte, at η = -200 mV for 300 seconds, at 0 and 1.5 T.

However, a different result is obtained when thickness is measured across the samples. Deposits were grown potentiostatically at η = -200 mV for different field intensities from a solution containing 0.3 M $CuSO_4$. Figure 4.4 shows the resulting profiles in both vertical and horizontal direction. The sketch shows the electrode position relative to the natural and Lorentz convection directions.

Given that under potentiostatic control fields increase the current, deposit thickness is expected to increase as well. This is the case, as the average height shows for the horizontal and vertical profiles.

For the case of horizontal profiles (in the direction of the Lorentz force) a build up of metal is seen at the leading edge in the Lorentz force direction. These peaks are typical of flow cells. Hence, reasonably, they seem to be promoted by the Lorentz-induced electrolyte flow. Increasing field intensity promotes higher peaks at the leading edge, indicating a direct proportionality between field intensity, Lorentz force magnitude, fluid velocity and metal build up at the leading edge.

In the case of the vertical profiles (in the direction of natural convection force) it is observed that, under no field, natural convection shapes the profiles in a similar way to that of magnetoconvection in the Lorentz force direction. When fields are applied, more even vertical profiles are obtained; magnetically induced convection seems to balance the effect of natural convection on profile development.

These results provide physical evidence of the comparability of $\boldsymbol{F}_L$ and $\boldsymbol{F}_{NC}$ magnitudes proposed by Hinds and co-workers [25] and discussed by other authors [21, 35]. They also agree with concentration distributions observed by Ragsdale and co-workers using an electrochemical scanning microscope [53].

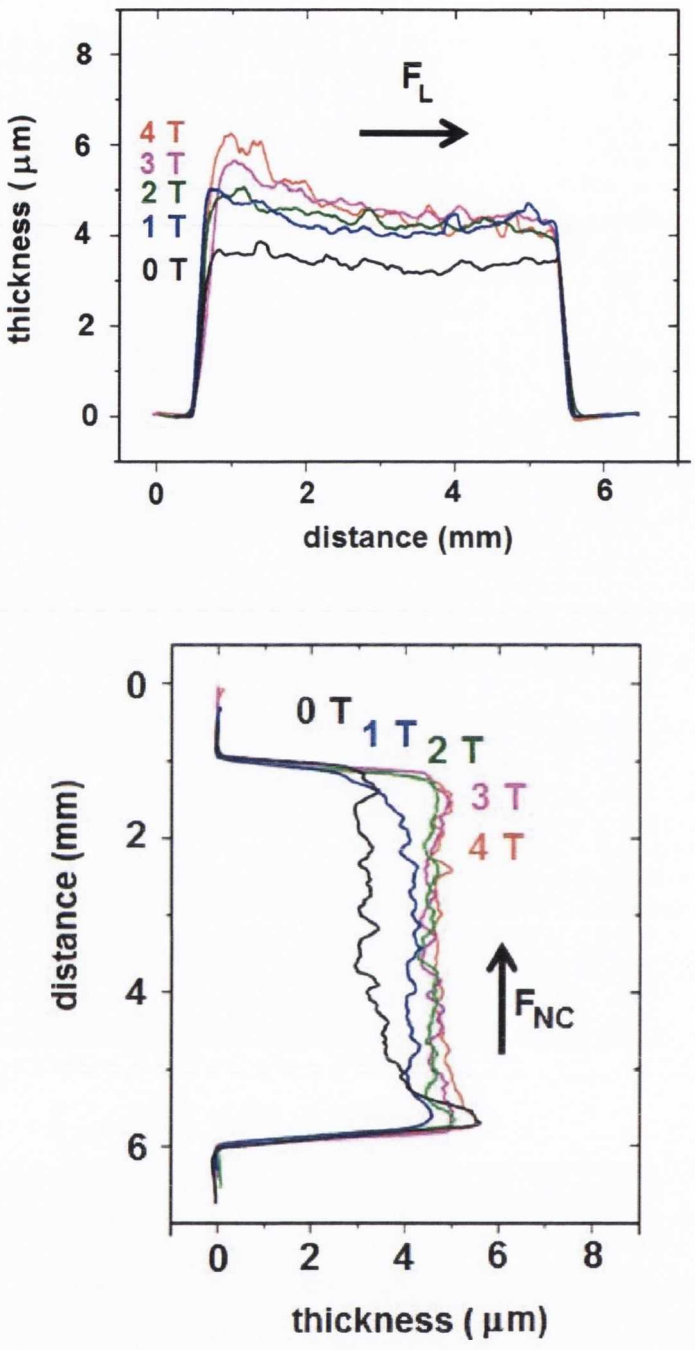

Figure 4.4: Profiles and morphology of samples grown potentiostatically at a vertically oriented electrode, from a 0.3 M $CuSO_4$ electrolyte, at η = -200 mV for 300 seconds, under magnetic fields up to 4 T. The directions of Lorentz and natural convection forces across the vertical electrode surface are sketched, and the magnetic field influence on the deposit profiles in their direction is shown.

The morphology was observed by scanning electron microscopy at different areas of the electrode. No evident change on growth mode was seen at any area. In particular, there is no difference between the left side and the centre of the sample, either with fields applied or not. An example is shown in figure 4.5.

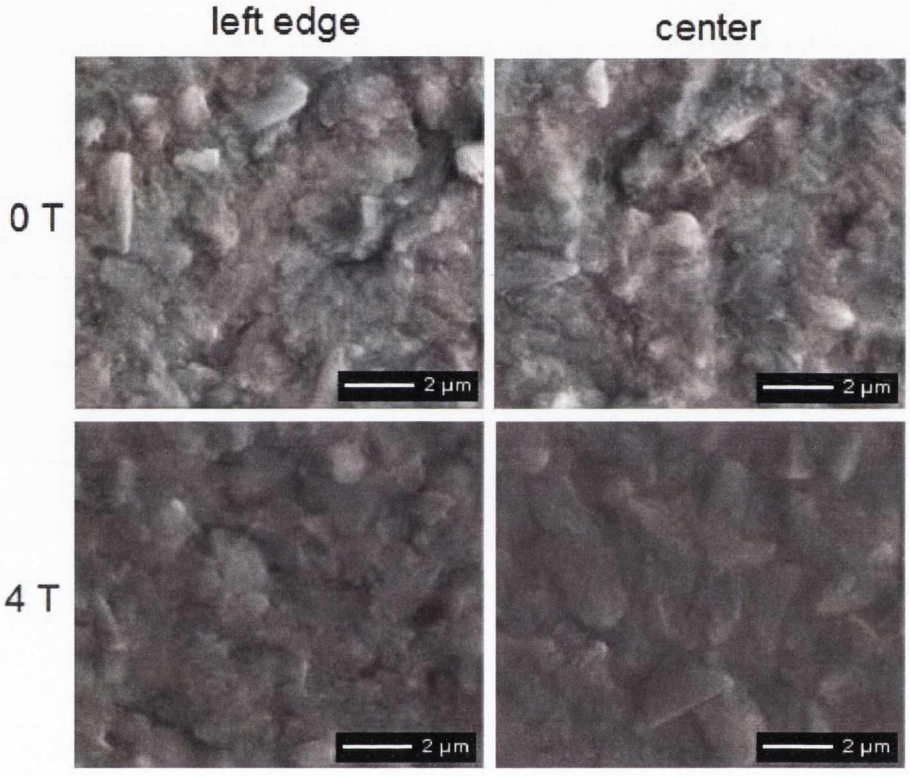

Figure 4.5: SEM images showing no evident change in the growth mode when samples are obtained potentiostatically at the mixed control region, under magnetic fields, neither on the left edge (where a peak associated with Lorentz force) or on the centre of the sample.

IV.1.2 Diffusion control conditions

Figure 4.6 shows SEM images of deposits grown from a 0.3 M $CuSO_4$ solution, at 0 and 4 T, for different electrode potentials, corresponding to the diffusion, mixed and activation controlled regimes (-550, -200 and -40 mV of overpotential, respectively). They show that field effect on deposit morphology is evident only in the diffusion limited regime, where dendritic growth is replaced by more columnar crystals.

Figure 4.7 shows images of deposits for the same electrolyte concentration, 0.3 M $CuSO_4$, after 25 seconds of deposition, when dendrites have not yet fully developed. It can be seen that particle shape changes from the early stage of dendrite formation without a field to more columnar crystals under field. The insets in the corresponding figures show expanded images of representative particles, showing at 0 T the characteristic axes of initial dendrites, with the primary branches around the central axis. At 5 T only the central axis corresponding to columns is seen. This is coherent with the fact that at zero field the system grows under mass transport limitation, which determines the initiation of dendritic growth. When a field is applied, magnetoconvection sets in and crystals grow with a higher concentration of copper ions ahead of the advancing interface, promoting columns instead of dendrites.

At -550 mV also the presence of pores is affected by the field. It can be seen from the same figure that the scarce but bigger pores found without a field are replaced by smaller but more frequent pores, as indicated by the white circles in the 5 T image.

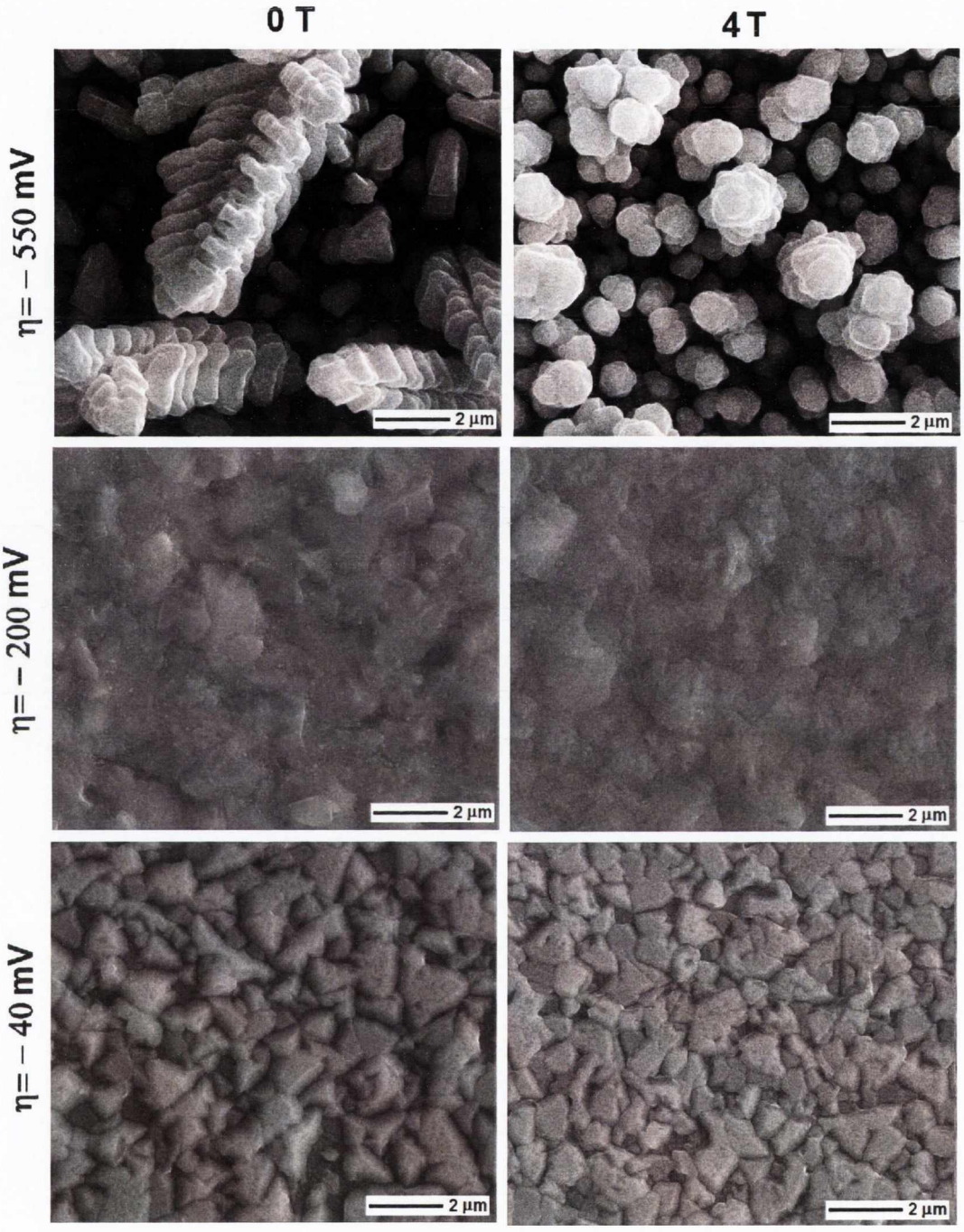

Figure 4.6: Morphology observed by scanning electron microscopy, for samples potentiostatically grown from a 0.3 M $CuSO_4$ electrolyte during 300 seconds, at 0 and 4 T. Overpotentials applied correspond to the zones of diffusion, mixed and activation control (-550, -200 and -40 mV, respectively).

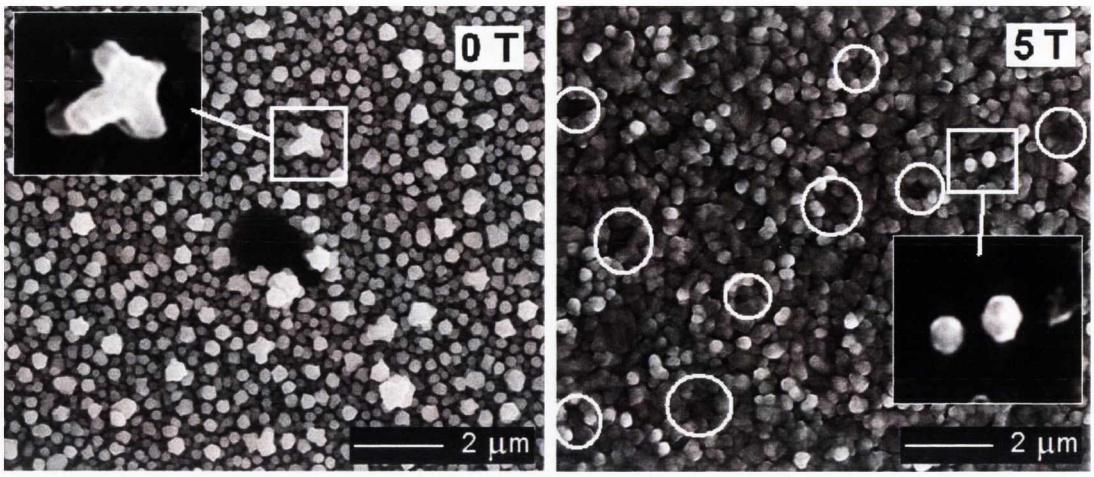

Figure 4.7: Scanning electron microscopy images showing the inhibition of dendrite formation at early growth stage, induced by magnetic field. Deposits were obtained after 25 seconds of deposition at η = -550 mV. The electrolyte used was 0.3 M $CuSO_4$.

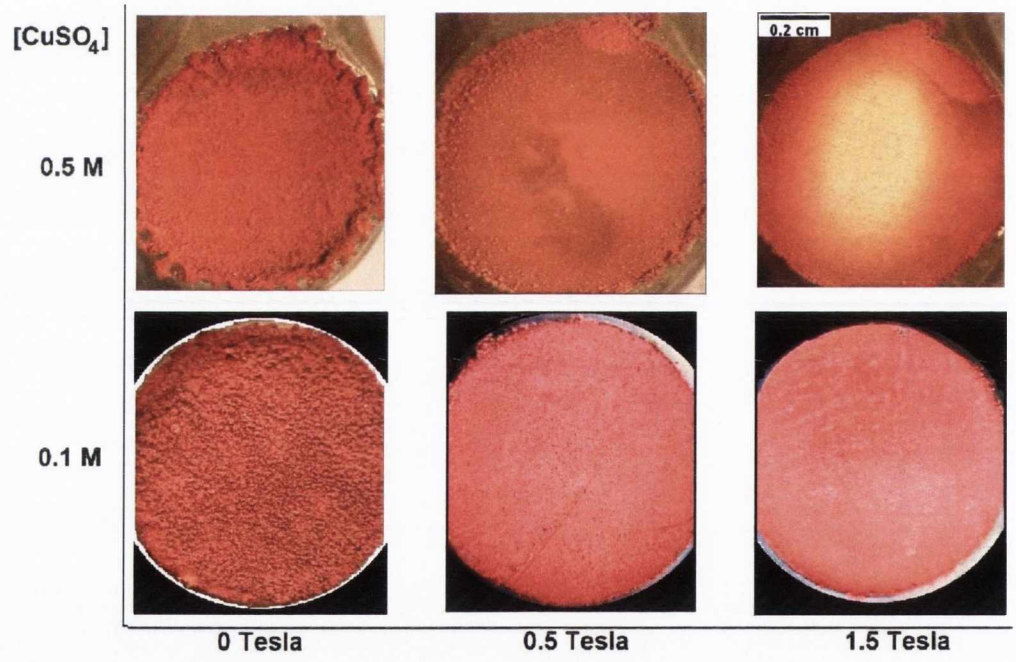

Figure 4.8: Macrographs showing magnetically induced improvement on deposit morphology, including edge effects, as a function of electrolyte concentration and field intensity. The electrode diameter is 0.8 cm. Spongy, powdery deposits typical of mass transport limitation are suppressed under magnetic fields throughout the whole electrode. In particular, the edges exhibit a much compact growth.

At a macro level, the field effect is evident. Figure 4.8 shows the field effect on the deposit morphology, including edge effects. Electrolytes containing 0.1 M and 0.5 M $CuSO_4$ were used and fields up to 1.5 T were applied. There is clearly an improvement of deposit brightness, and the edges present less build-up of material. The better results are found for higher copper concentrations.

The ellipse formed at the centre of the electrode surface in 1.5 T with the 0.5 M $CuSO_4$ electrolyte, which appears shiny and smoother, gives an idea of the hydrodynamic conditions established in the central part of the circular electrode.

Figure 4.9 shows profile measurements carried out for samples grown at η = -400 mV. As expected, higher fields promote thicker deposits. The three-dimensional nature of the growth structures is clearly seen as big height differences on the profiles. The data are plotted to highlight those differences, so the aspect ratio (thickness vs. distance axes) is altered. Also, these are soft (spongy) deposits, so although the profiles are representative of the samples, some material is lost because it attaches to the measuring needle of the Dektak instrument.

Again in the profiles a build-up of material is found at the leading edge of the flow, whether arising from gravity or magnetic field's influence.

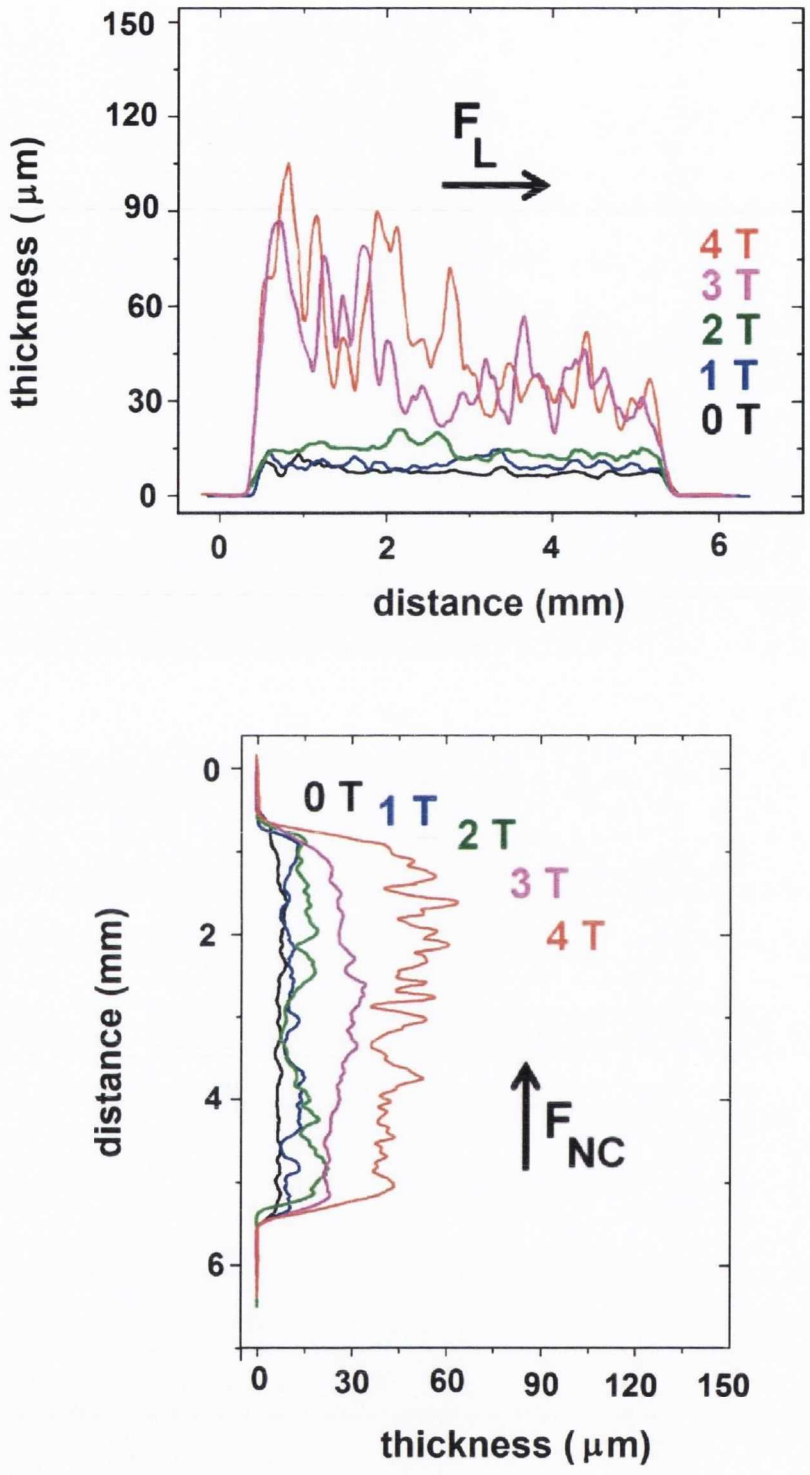

Figure 4.9: Profiles and morphology of samples grown potentiostatically from a 0.3 M $CuSO_4$ electrolyte, at η = -400 mV for 300 seconds, under magnetic fields up to 4 T. The directions of Lorentz and natural convection forces across the vertical electrode surface are sketched.

Topography and roughness was also measured by AFM for samples grown potentiostatically in the diffusion-controlled regime. In this case, deposition was performed for short times in order to avoid excessive height differences for the cantilever. In general, roughness is reduced in proportion to the field intensity, as can be seen from figure 4.10. Here, deposits grown potentiostatically for 2 seconds at η = -400 mV from a 1 M $CuSO_4$ solution are shown. Here the field effect is observed for timescales where convective flow is not yet steady. The roughness changes in such conditions indicating that some aspect related to ions diffusion is affected by the fields.

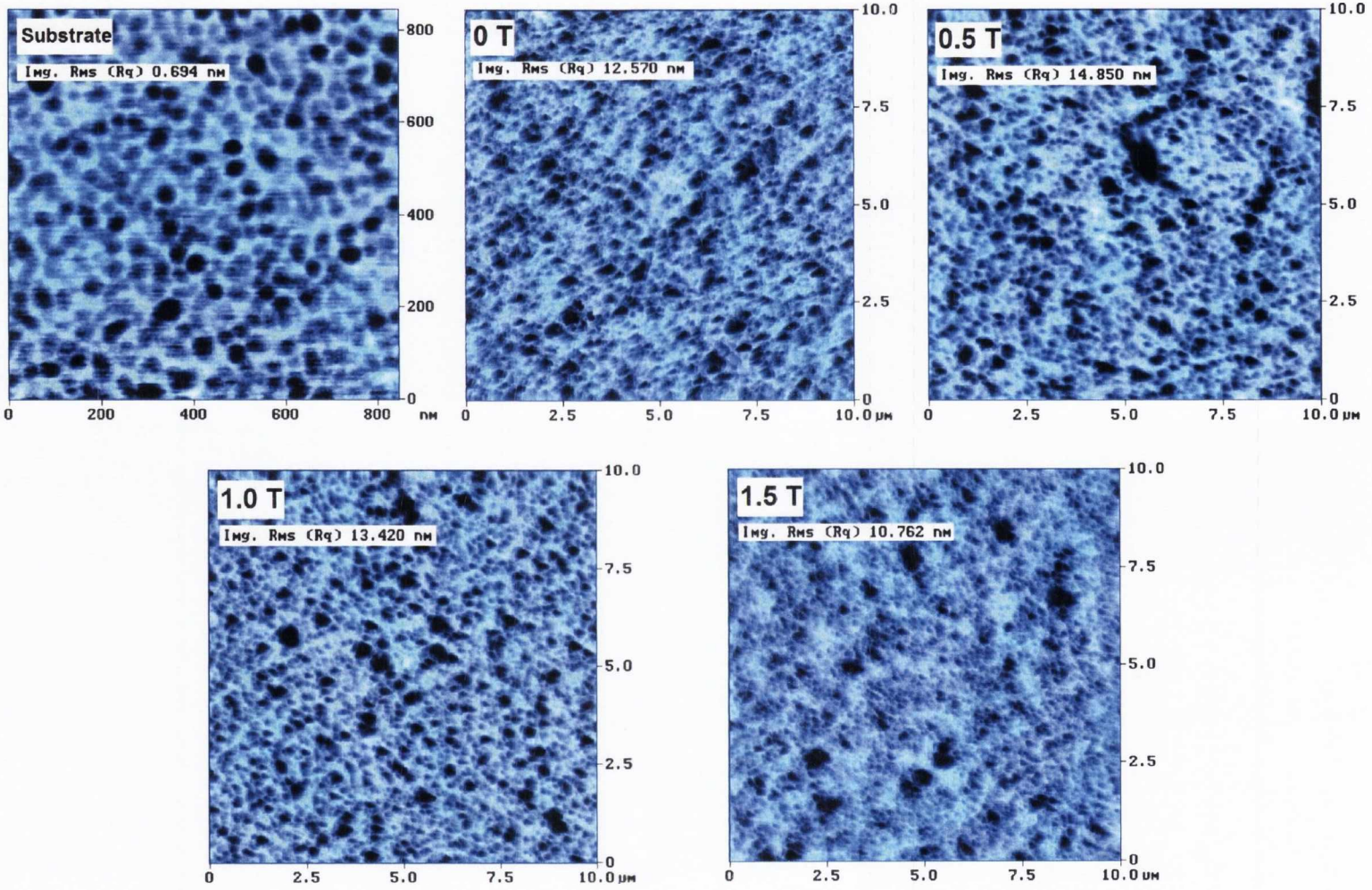

Figure 4.10: AFM characterization showing the magnetic field induced reduction of roughness for samples grown after a 2-second potential pulse at diffusion-limited overpotential (η = -400 mV). The electrolyte used was 0.3 M $CuSO_4$.

IV.2 Deposition under galvanostatic control

The profiles shown thus far were obtained at fixed overpotentials, which gives the system one degree of freedom, observed as variations of the measured current density. This means that for every value of current density, a different average growth rate was associated. The local distribution of current changed with the field as well.

In order to analyse the evolution of deposits grown at equal average growth rates, galvanostatic control was used. The obtained deposits were characterized by profilometry, SEM and AFM.

Samples were grown for different times, from 5 to 2500 seconds from a 0.3 M $CuSO_4$ electrolyte using j = -60 mA cm^{-2}. Fields up to 5 T were applied vertically to vertical electrodes, which gives as a result a horizontal Lorentz force. Figure 4.11 shows an example of the profiles across the Lorentz force direction, of deposits grown for 25 and 2500 seconds. It is seen that the same characteristic profile develops, with material build-up on the leading edge of the electrode. Unlike the case of deposition at fixed potential, when the current is fixed, higher fields lower the peaks at the leading edge of the flow and tend to produce more even deposits.

The local current distribution is clearly affected with the field. In the galvanostatic mode, however, the j/j_L ratio decreases with increasing field. Its values decrease from 1.5 at 0.0 T to 0.8, 0.55, 0.52 and 0.50 at 0.5 T, 1.5 T, 3.0 T and 5.0 T respectively. The values under field correspond to the mixed control zone (MIX), with the diffusion-limited component of the current in that zone decreasing with lower j/j_L ratio values. Hence, lesser amounts of current are susceptible to transport limitation under field. This may explain the lower peaks at higher fields in the galvanostatically controlled experiments.

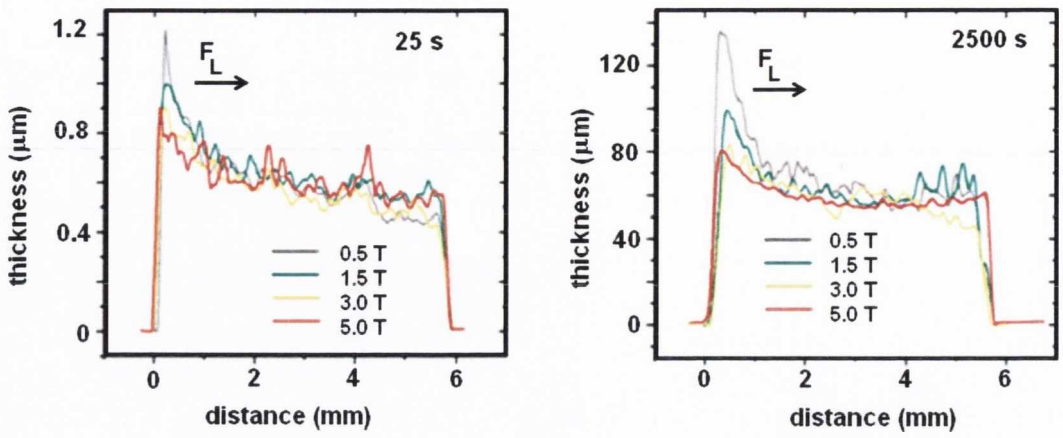

Figure 4.11: Profile measurements of deposits obtained under galvanostatic control from a 0.3 M $CuSO_4$ electrolyte at vertical electrodes under vertical fields up to 5 T. The applied current is j = -60 mA cm^{-2}. Fixed time of deposition is 25 and 2500 seconds.

Roughness analysis of samples grown for short times was carried out by atomic force microscopy. Figure 4.12 shows the images for samples grown during 10, 15, 30 and 60 seconds. For samples grown at longer times (i.e. higher thickness) the AFM image reliability deteriorates because of the specific characteristics of the technique, where physical proximity of the tip to the sample restricts its accuracy for deposits with big variations in height. The scan area corresponds to 10 μm x 10 μm in all cases. It is seen that at zero field the growth is very different from that obtained under applied field, and that any field intensity promotes a similar type of growth. The morphology of samples grown at zero field evolves differently than it does under fields, when there are smaller particles. In association with these samples, figure 4.13 shows SEM of deposits grown for 30 seconds at 0, 1.5 and 5 T. From the images it is clearly confirmed that there is a change in growth mode when samples are obtained under magnetic fields.

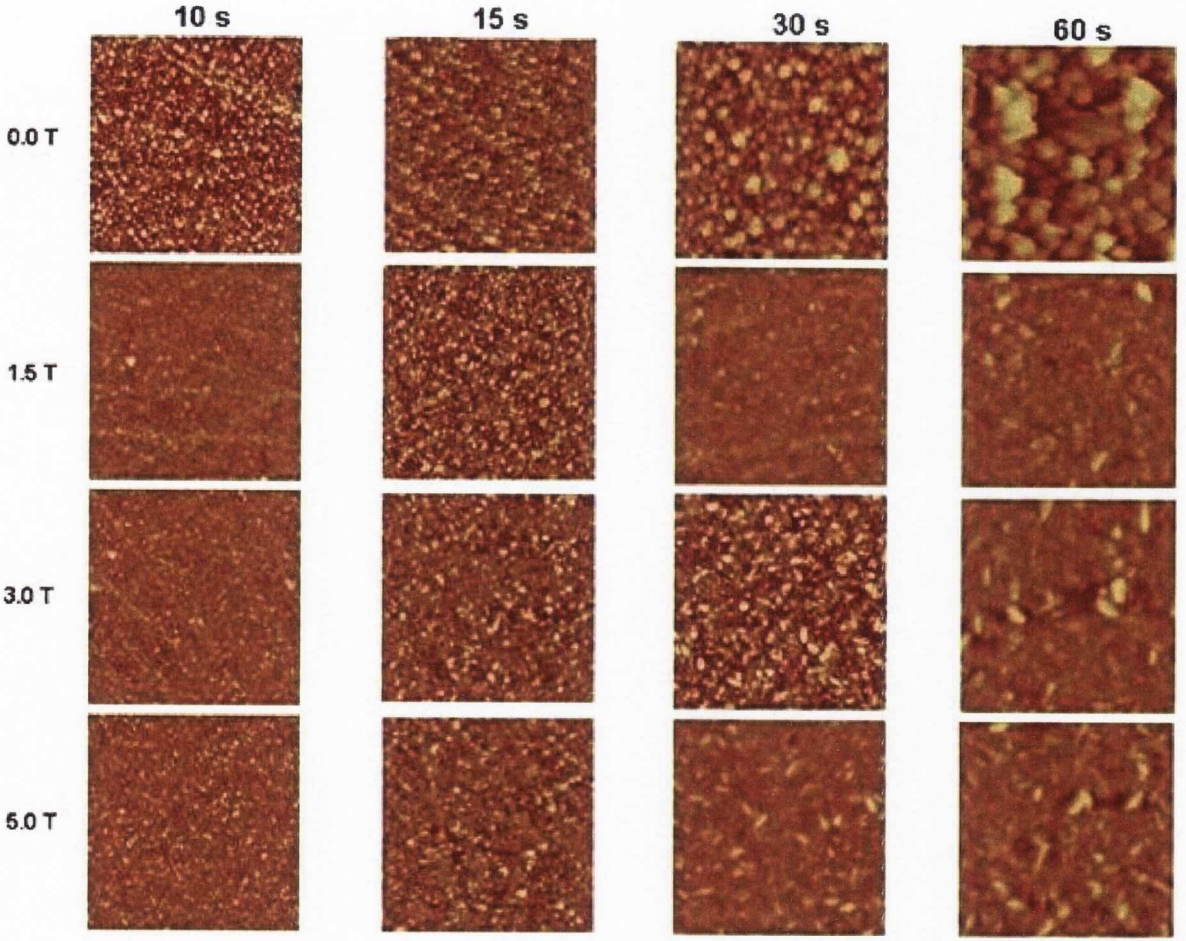

Figure 4.12: AFM images showing the effect of magnetic fields on the particle size and shape of copper deposits obtained under galvanostatic control at $j = -60$ mA cm^{-2} from a 0.3 M $CuSO_4$ electrolyte. Deposition times are 10, 15, 30 and 60 seconds.

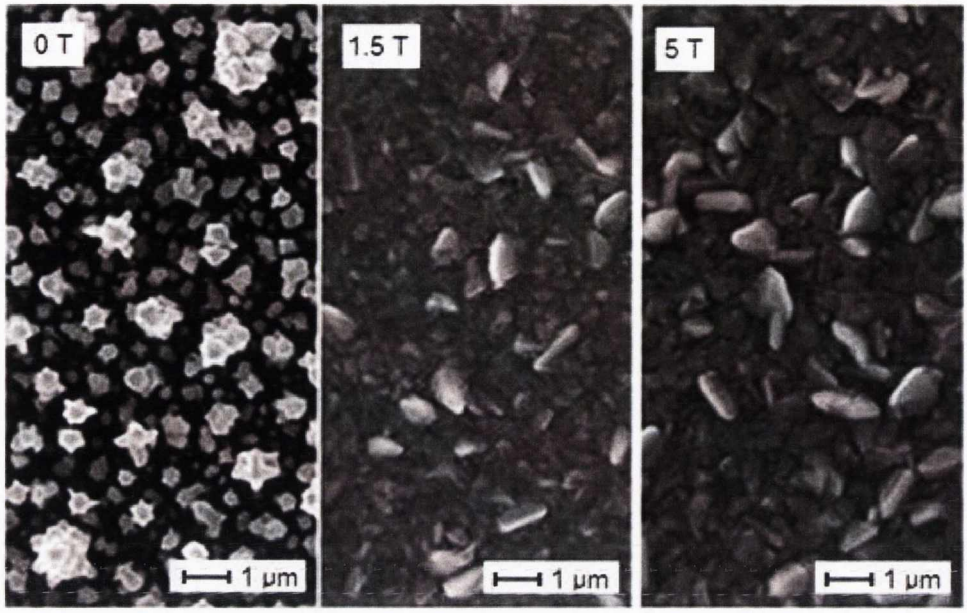

Figure 4.13: SEM images corresponding to samples grown during 30 seconds of deposition at $j = -60$ mA cm^{-2} from a 0.3 M $CuSO_4$ electrolyte in different fields. A change in growth mode is seen when magnetic fields are applied.

A quantitative approach is shown by the plot of figure 4.14, for the case of samples grown for 15 seconds at 0 and 5 T. Three-dimensional (*xyz*) data obtained with the AFM were used to calculate the values of the roughness ω as a function of measurement scale length *l*, Eq. 8. The slopes with and without field do not coincide. The slope at the initial part of the curves indicates that the value of roughness changes with the length scale *l*, which is expected since the average value depends on the topology, hence on the extent of the measured surface. Saturation is found for measurements at *l* higher than ~ 300 nm, and the roughness value is reduced from 28 nm to nearly 15 nm with field.

With this information, the values of roughness as a function of deposition time can be evaluated. An example is seen in figure 4.15, which shows roughness evolution with time for deposits grown at $j = -60$ mA cm^{-2} with and without fields. The group of data collected under field

fall onto one single line, clearly separated from the line describing roughness evolution at zero field. The gradient indicates that under field the rms values escalate at a much lesser rate than under no fields. This is consistent with the electrochemical response of the system for such conditions. As figure 4.16 shows, at zero field the cell overvoltage is around 0.8 V, while under any field from 0.5 T to 5 T, the cell overpotential is reduced to approximately 0.25 V.

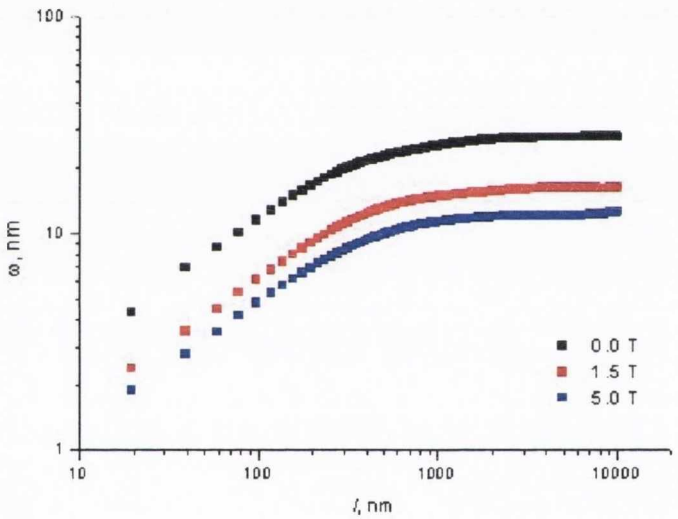

Figure 4.14: Surface roughness obtained from AFM measurements at 15 seconds of deposition at $j = -60$ mA cm^{-2} from a 0.3 M $CuSO_4$ electrolyte.

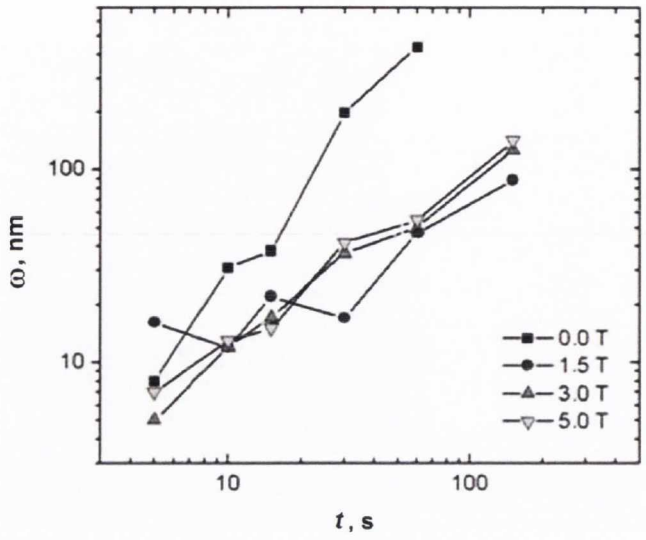

Figure 4.15: Effect of magnetic fields up to 5 T on roughness for samples galvanostatically obtained control at j = -60 mA cm^{-2}, as a function of deposition time. Electrolyte: 0.3 M $CuSO_4$.

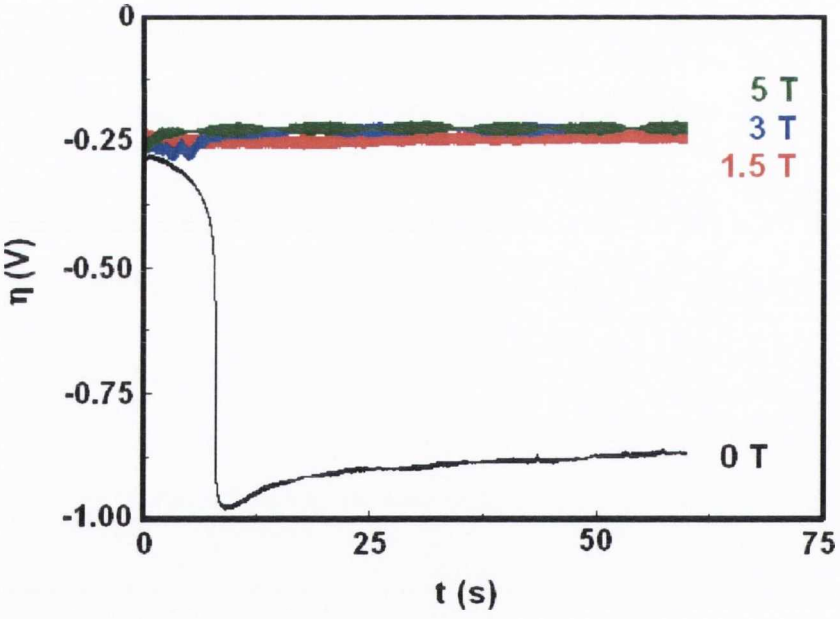

Figure 4.16: Overpotential shift due to magnetoconvection, when $j/j_{L\ (B=0)}$ = 1, changes to $j/j_{L\ (B\neq0)}$ < 1.

IV.3 Discussion and summary

Different characterization techniques were used to study the magnetic field influence on copper growth. Potentiostatic and galvanostatic control was performed. Under potentiostatic control, in the mixed control zone (MIX), SEM images reveal no change in growth morphology due to the field. Roughness measurements also are unchanged with field. However, the same samples exhibit a strong change in thickness throughout the electrode length. Build-up of material at the leading edge of the flow, characteristic of flow cells, was found in relation with the Lorentz force. SEM did not reveal any difference in morphology between the area facing the flow and the rest of the sample.

Under potentiostatic control, in the diffusion control zone (DIF), there are observable changes with all the characterization techniques. SEM images show a remarkable change in growth morphology: dendritic growth change to nodular. Roughness is reduced with fields, accordingly, within the same order of magnitude. This could be identified both at short (~ 2 s) and long times (~300 s) of deposition. The growth change was observed even for the high concentrated electrolytes, where less mass-transport limitation is expected. In the same manner as they did for the deposits obtained at the mixed control zone, profiles thickness increased with increasing fields. On the macroscale, the hydrodynamics could be observed through smoother deposits both in the central part and in the edges of samples of nearly 1 cm in diameter.

Under galvanostatic control, there is a strong field effect when $j/j_L = 1$, corresponding to the mass-transport limitation zone. The growth mode dramatically changes from dendritic to planar, as shown by SEM images. The corresponding cell voltage is reduced by nearly 500 mV, as shown by electrochemical tests. Profiles still develop a build-up at the

edge facing the flow, however, their height is reduced with increasing field intensity. Roughness, measured both by SWLI and AFM, is strongly reduced by 1 order of magnitude, from 3 um to 0.3 um, in association with the change in growth mode. This indicates that growth mode, and the associated scaling roughening, are governed by the overpotential, in agreement with observations by Schwarzacher and co-workers [54,55].

Chapter V

Magnetic field effect on growth of Hydrogen bubbles

Electrodes producing gas as a result of the reaction they host are known as *gas evolving electrodes* and are relevant to many industrial processes. Water splitting, electroflotation, bubble actuation and corrosion are a few to mention. Hydrogen evolution is a frequent side reaction during electrolytic metallization processes from aqueous solutions. It occurs in the Cu^{2+}/Cu^{0} system at high cathodic overpotentials, according to the equilibrium given by the line (a) in the Eh-pH diagram.

In view of its importance for electrochemistry and industrial processing, it is relevant to study the magnetic field effect on this reaction. This section focuses on the hydrogen evolution reaction alone. In particular, the magnetic field effect on growth of hydrogen bubbles produced from a copper-free electrolyte is analysed.

V.1 Electrochemical investigation of gas evolving electrodes

The reactions occurring at gas evolving electrodes constitute an important field of study for both industrial and scientific arenas. References include water electrolysis for hydrogen production [56], Lab-on-a-chip microelectronics [57-59], electroflotation [60], during electrolytic obtention of metals [61] or corrosion [62]. The cell voltage for water electrolysis is given by:

$$E = E_{TMD} + E_{IR} + E_H + E_O \tag{5.1}$$

where the subscript E_{TMD} indicates the thermodynamic term, E_{IR} the ohmic contribution and E_H, E_O are the electrode potentials for hydrogen and oxygen evolution reactions, respectively. Usually, the ohmic contribution is reduced with a suitable geometric disposition of the cell electrodes and the use of conductive media. However, the reaction products (hydrogen and oxygen gas) have themselves insulating properties and thus their presence in front of the reacting surface is expected to contribute to the E_{IR} term.

At the same time, the bubbles leaving the electrode agitate the electrolyte at the reacting front, and thus they are also expected to contribute to mass transfer enhancement. This makes the evolution phenomena a quite challenging reaction to follow and for description via mathematical models [63, 64]. The measured signal, due to these dynamic phenomena occurring at the electrode surface and surroundings, presents itself very noisy.

V.1.1 Fluctuations of the measured signal

V.1.1.1 General aspects

A first approach to the magnetic field effect on the hydrogen reaction was obtained by using a 1.2 M H_2SO_4 electrolyte and copper disk electrodes of 5400 μm in diameter, positioned vertically. Magnetic fields from 0 T to 5 T were applied, also vertically. For this configuration the resulting Lorentz force acts sideways, across the surface of the electrode, as the inset in Figure 5.1 shows. The cyclic voltammograms of this figure show that hydrogen currents increase in proportion to field intensity.

Figure 5.2 shows current-time sequences when the system is potentiostatically controlled at $\eta = -1.0$ V, for the same configuration. The current increases, in accord with the cyclic voltammogram, and sequential current fluctuations of different magnitude are observed. The noisy signal is characteristic of gas evolution. The drift to lower magnitudes of current is due to an increase in the IR drop across the cell during the experiments, as expected due to the ohmic effects associated with the screening of the electrode surface by attached hydrogen bubbles [74, 75].

In the traces of figure 5.2, current drifts followed by sharp returns to the baseline indicate the occlusion of the electrode surface by bubbles attached to it. The reasoning behind is that, as the bubbles grow, they cover an increasingly large portion of the cathode surface, which translates into a decrease in current magnitude. Large bubbles are also formed by a coalescence process where smaller bubbles progressively join together to form bigger ones. When a bubble detaches, the surface formerly occluded is suddenly available for hydrogen reduction, which leads to the sharp increase in current. The low amplitude oscillations are

related to an evolving stream of small bubbles, whereas bigger oscillations correspond to the release of a larger bubble. Hence, the size of the released bubbles can be estimated from the sharp steps in the time sequence. According to this, the sharp steps, of about 2-4% of the signal would correspond to the release of bubbles of nearly 200-400 μm in diameter.

From the connection between the amplitude of the sharp steps and the bubble size, it is apparent that the maximum bubble size in this configuration is reduced by the magnetic field. During the experiments, streams of small bubbles spread throughout the electrolyte due to the induced convection. Since the electrode is vertical, with a vertical field parallel to the electrode surface, the flow generated by the Lorentz force across the surface (as shown the inset in Fig. 5.1) tends to dislodge the hydrogen bubbles sideways as they form. An enhancement of the hydrogen current of up to 25 % in large fields is observed. This is due, at least in part, to less of the cathode area being occluded by bubbles.

At high fields ($\geq$ 3 T) the transparency of the solution was visibly reduced by the presence of many very small bubbles, resembling a colloid suspension. The time needed for the cloudiness to completely disappear was 2-5 min after the experiments stopped. Matsushima et al. [67] had previously described the solution becoming cloudy when hydrogen was evolving under an applied field.

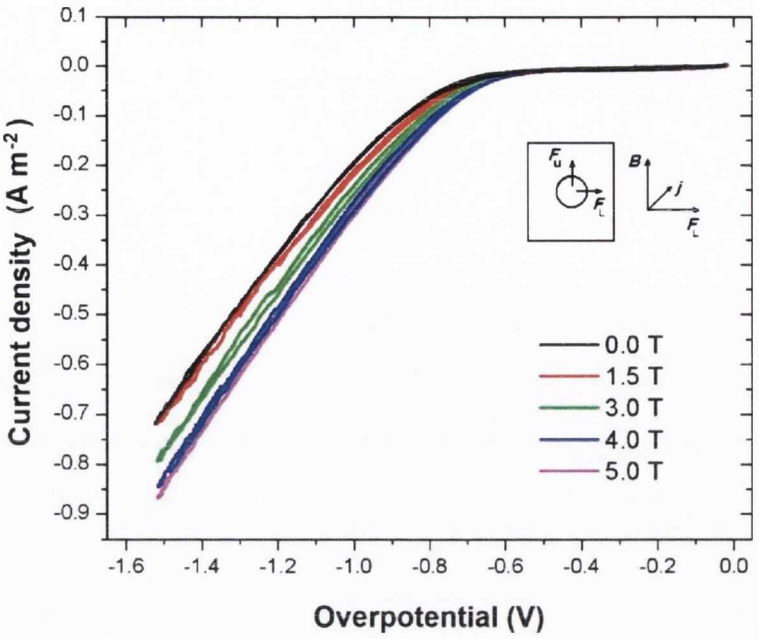

Figure 5.1: Cyclic voltammetry at 0.2 V s^{-1} showing the effect of vertical magnetic fields up to 5 T when a Cu electrode of 5.4 mm in diameter is vertically immersed in a 1.2 M H_2SO_4 electrolyte. The insets show the electrode considering the direction of the current and magnetic field, as well as the Lorentz and upthrust forces.

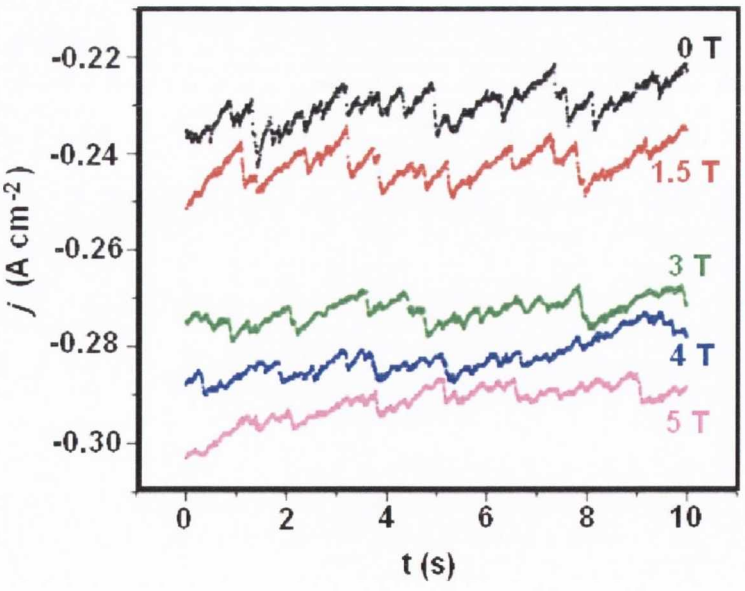

Figure 5.2: Time sequences (chronoamperometry) measured potentiostatically at $\eta = -1.0$ V for a 5400 μm electrode in the conditions of figure 5.1.

V.1.1.2 Noise modulation with electrode size

Since gas bubbles on the electrode surface contribute a resistive component to the measured electrochemical response, the effect of the size of the gas evolving electrode has been analysed. When the electrode size changes the number of bubbles able to form on the surface also does. In consequence, the ratio between the reactive and occluded areas also changes, which has an impact on the noise of the measured signal. By using an electrode small enough, it is possible to modulate noise until a very characteristic oscillation is found, as figure 5.3 shows. In this case, the size of the copper electrode has been reduced to 125 μm in diameter. The applied overpotential is η = 1 V, the electrolyte is 1.2 M H_2SO_4, and no field is applied. These are the same conditions as for the black curve in figure 5.2, except for the electrode size. Clearly, a very regular oscillation waveform is produced in the case of the microelectrode.

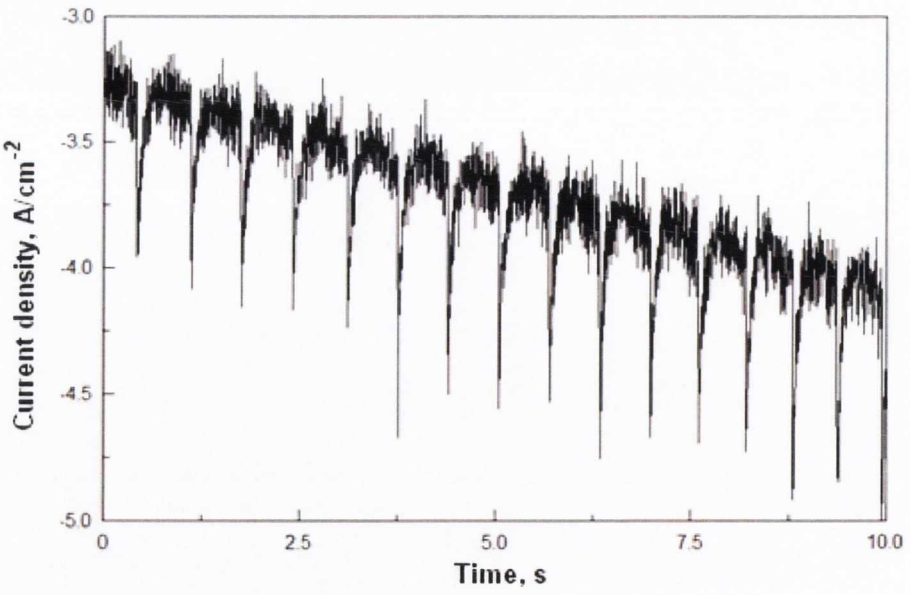

Figure 5.3: Time sequences for hydrogen evolution at Cu microelectrode of 125 μm in diameter, potentiostatically controlled at η = -1.0 V. Electrolyte is 1.2 M H_2SO_4.

The same type of oscillation, flipped vertically, is obtained for galvanostatic control of the reaction, as expected from the current-potential relation. The case is shown in figure 5.4, for a Pt microelectrode. Here, high current density (j = 20 A cm^{-2}) is used, so that larger oscillations are observed. The figure shows the typical information that can be extracted from the time sequences of single bubbling during galvanostatic control. They exhibit characteristic oscillation amplitude η_λ, frequency f and baseline value η_{base}. The bubble departure is connected with return of the signal to the baseline η_{base}. The inverse of the time elapsed between these returns is the oscillation frequency f or the frequency of bubble production. The oscillation amplitude η_λ is also a measure of the IR contribution due to the isolating bubble.

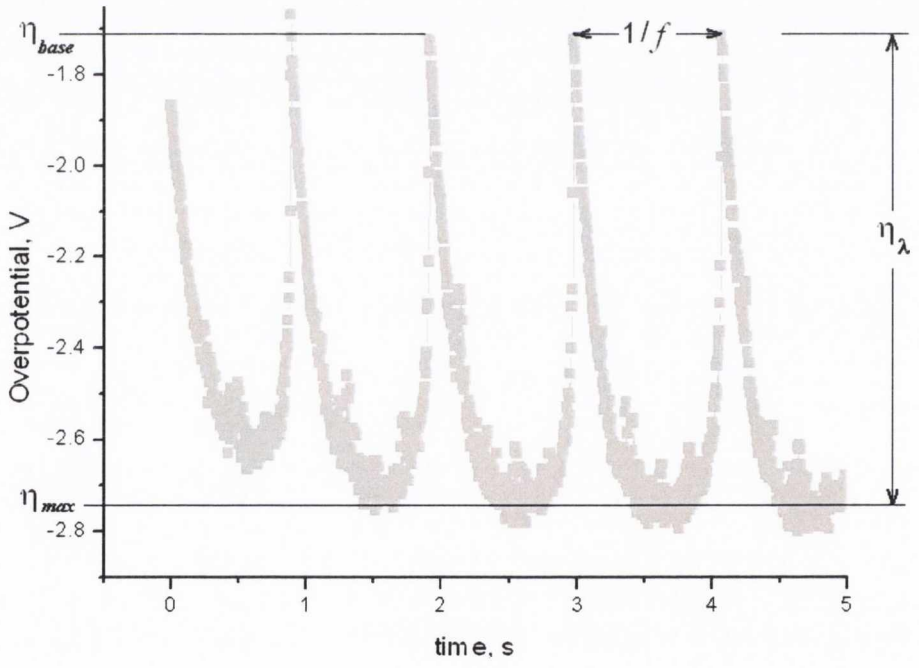

Figure 5.4: Characteristic information that can be extracted from overpotential oscillations during galvanostatic formation of single bubbles at gas evolving electrodes. Pt substrate, ϕ = 125 μm, j = 20 A·cm^{-2}.

V.1.1.3 Formation of single bubbles

The regular oscillation waveform on the measured signal is related to the formation of single bubbles. Figure 5.5(a) shows the matching images of the electrode surface at the time indicated by arrows on the graph. Clearly, each oscillation cycle corresponds to the growth-detachment cycle of one bubble on the surface of the 125 μm diameter Pt electrode.

The dynamics of growth and detachment of bubbles during gas evolution at larger electrodes has been related to overpotential fluctuations for growth of multiple bubbles [61, 68]. The gas phase attached to the electrode reduces its reactive area, changing the primary current distribution and consequently introducing an ohmic component to the measured signal [66].

Figure 5.5(a) shows that, in effect, when a single bubble grows on the electrode surface the overpotential increases (note the overpotential is a negative quantity for a cathodic reaction). This occurs progressively in direct proportion to the bubble size, until detachment begins. At this point, the ohmic contribution is reduced and thus the overpotential is sharply reduced.

By changing the current applied the maximum bubble size was controlled. It was found that bubble size was directly proportional to current density, j. This agrees with reports where larger sizes of bubbles were obtained by increasing current density, however for multiple bubbles growth [60, 63, 68, 69]. We also found that the release frequency f is inversely proportional to j, which relates larger bubbles with longer residence times. The oscillation amplitude λ is directly proportional to the current, which suggests that larger bubbles produce higher ohmic drops.

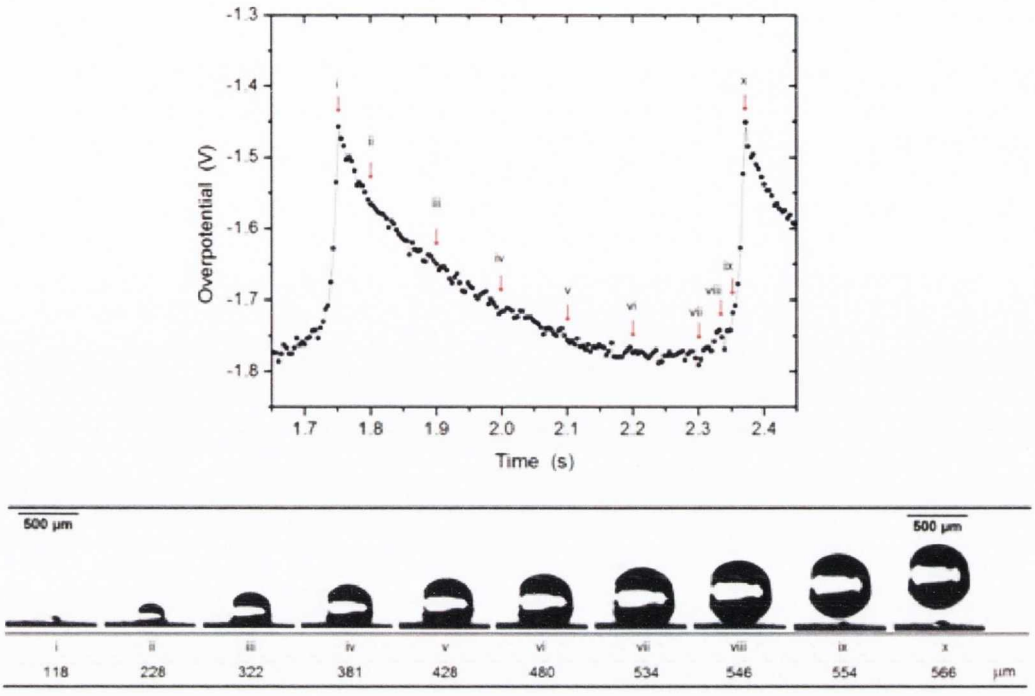

Figure 5.5: Relation between overpotential oscillation and growth-detachment cycle of a single bubble, grown galvanostatically at j = 10 A·cm^{-2} over a Pt microelectrode of ϕ = 125 µm.

From these observations, the oscillation frequency was related to bubble size, taking into account the ideal gas and Faraday laws, as follows. The pressure of hydrogen inside the bubble is close to atmospheric pressure P_0. Corrections are ρgh due to the depth h of the electrolyte of density ρ above the microelectrode surface, and the pressure difference $2\sigma/r$ across the curved surface of the bubble, where $\sigma \approx 70$ mN m^{-1} is the surface tension of water. Both these corrections amount to less than 1% of P_0 and can safely be neglected.

The ideal gas equation $PV=nRT$, where P is the absolute pressure of the gas, V is the volume, n is the number of moles of produced gas, R is the gas constant and T is the absolute temperature, can be combined with $n = Q/zF$, where Q is the charge passed, z is the number of electrons transferred per ion and F is Faraday's constant. At galvanostatic

conditions $Q = It$. Hence, considering the area of the electrode πr_e^2 and the time of bubble growth $1/f$, the moles of hydrogen produced by electrolysis of the couple $2H^+/H_2$ is expressed as:

$$n = \frac{\pi r_e^2 j}{2Ff} \tag{5.2}$$

The radius of the bubble r_b, assuming it to be spherical, can be calculated from:

$$r_b = \left(\frac{3r_e^2 jRT}{8FfP_0}\right)^{1/3} \tag{5.3}$$

For the bubble in Figure 5.5(a), calculations indicate 548 μm in diameter, which matches within 5% error the maximum size measured from images taken with the high speed camera. Similar accuracy was found for different currents ranging from 1 to 20 A cm-2, as shown in Figure 5.5(b). The reason for such an accurate description of the bubble size is rooted in the oscillatory behavior of the signal. The wave frequency f is a direct effect of the IR drop introduced by the bubble itself to the system. Smaller bubbles produce less electrolyte resistance hence the overpotential oscillates with lower amplitude. At the same time they are released faster hence each cycle ends sooner and the frequency is higher. Hence, taking f as a descriptor of the bubble size is appropriate.

It is also important to note that indicators such as moles converted during the electrochemical reaction only indicate the amount of gas produced in molecular form, not the amount of gas found separate from the liquid. The gas converted via electrolysis mainly dissolves into the solution, giving very low gas efficiencies, with proportions as low as 5 to 35% of the past current constituting observable bubbles [60, 70]. The difference is that in the experiments presented here the currents used were up to 3 orders of magnitude higher. The models presented by Vogt [63, 64] relate bubble coverage and gas efficiency with a wide range of current densities, from 0.1 mA·cm^{-2} to 25 A·cm^{-2}. According to Vogt's

model, the current density range used in the present investigation (between 1 and 20 A·cm^{-2}) is high enough to achieve from 50% to 90% gas efficiency. This explains the good correspondence between calculated and observed bubble sizes.

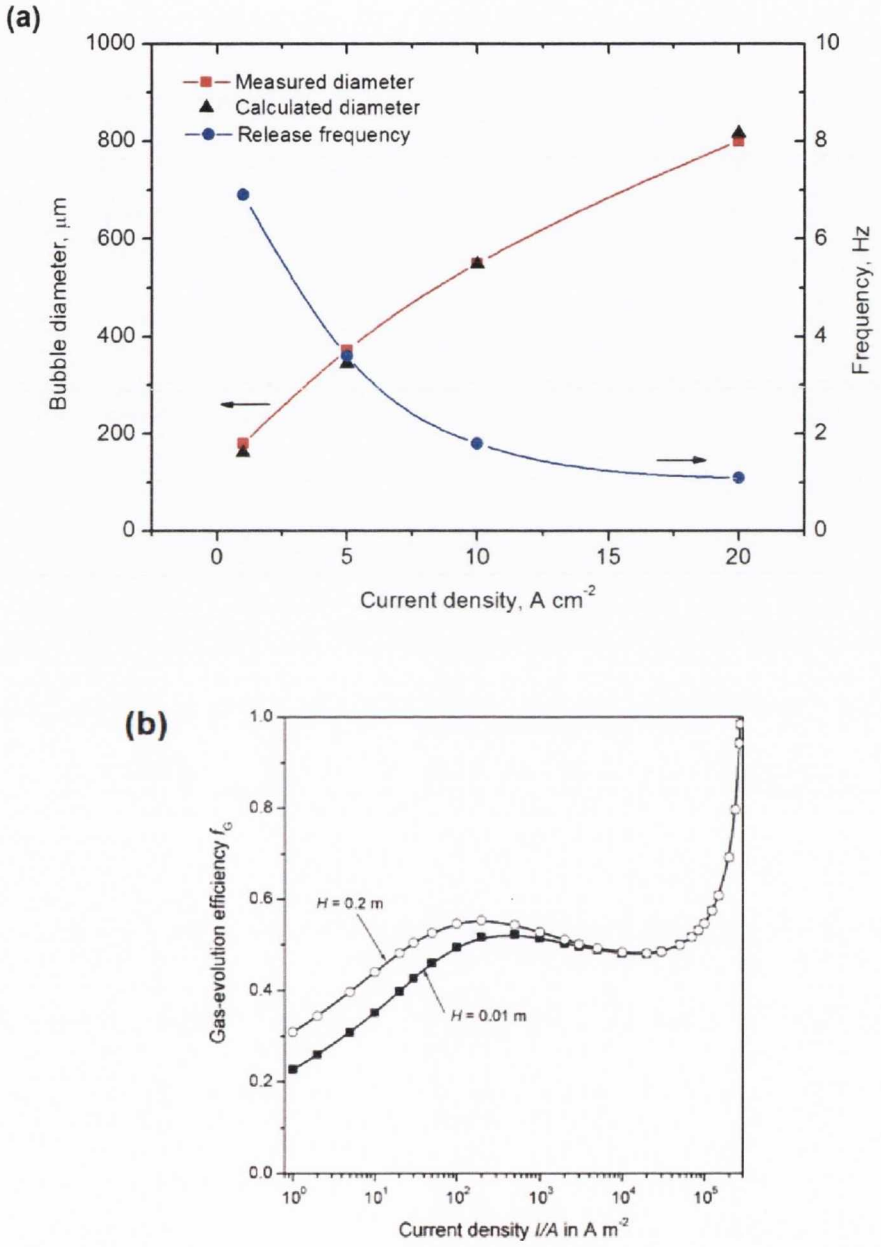

Figure 5.6: (a) Dependence of release frequency and bubble size on current density (b) Vogt's model showing the dependence of gas efficiency on the current density, for different height of electrodes (H); image taken from [9].

V.1.1.4 Waveform shape and stages of bubble growth

Bubbles in Figure 5.7(a) and (b) were grown at fixed *j* values of 10 and 20 A cm^{-2}, respectively. As shown in the previous section, higher currents convey larger mass fluxes and hence larger bubbles are formed. The case shown in (a) is the same as in figure 5.5, but here is compared with a bubble producing a slightly different oscillation waveform, in order to show that detachment dynamics determines the waveform shape.

Several stages can be identified. From the starting point a nearly hemispheric layer of gas gains height until it reaches a nearly spherical shape ("height growth"). A second stage corresponds to an increase of size in all directions ("radial growth"). Up to this point, substrate coverage has progressively increased. It is remarkable that the bubble clearly covers a wider area than the 125 μm diameter electrode. This means that it extends beyond the limits of the metal and onto the surrounding resin.

In the third identified stage, the bubble stretches up, changing its shape to a spheroid ("stretching"). Here the coverage is slightly and progressively reduced, as a result of progressive dislodgement. Finally, the bubble gains enough height to significantly reduce the thickness of its connecting bridge to the substrate ("necking") and finally breaking it. Necking occurs very fast, approximately within 5 ms, ending the cycle. Noticeably, at the starting point of a new cycle a layer of gas phase is already formed over the electrode, product of the neck break.

The difference between the growth-detachment cycles in figure 5.7(a) and (b) is determined by the extension of the height growth, radial growth, stretching and necking stages. In (a) stretching is fast, ending the growth cycle quickly; dislodgement begins at 90% of the cycle (image vii). In a different way, the bubble in Figure 5.7(b) takes longer to separate from the electrode, hence the associated overpotential reduction

appears at 67% (image vi) of the full cycle. The images show that the "necking" stage only corresponds to the very last part of the detachment process, reflected in the electrochemical signal as the sharp step back to the baseline.

The images demonstrate that the mechanism producing the overpotential fluctuation can no longer be explained in terms of partial occlusion and re-exposure of surface due to consecutive cycles of bubble growth and detachment. That is simply impossible in these experiments since the bubbles largely exceed the electrode size at almost all times. However, it is also clear that the effect is related to the bubble cycle and its ohmic contribution to the overpotential measured.

Figure 5.8 proposes a suitable explanation. It sketches the consecutive stages of the bubbling cycle, in relation to their influence on the primary current distribution. A dual-phase volume near the electrode surface is considered. This would be a fuzzy, transitional zone from fully electrolyte (in the solution bulk) to fully gas (in the bubble bulk).

In this case the least resistance pathway defines the reacting volume. For a thin layer of gas spread on the electrode, figure 5.8(a), all the points represent similar resistance. Although there is no free surface, there is still access to the electrode. This resistance is represented by the oscillation baseline, η_{base}, in the measured signal.

Upon bubble growth, the shortest path towards the metal is restricted to a ring-zone at the bubble's base, figure 5.8(b). As a consequence, the reacting volume decreases. Being the system forced to maintain a fixed reaction rate, the ohmic contribution is increased since increasingly more gaseous products and less H^+ reagents are found in the conducting volume. This is represented by the growing oscillation amplitude η_λ in the measured signal.

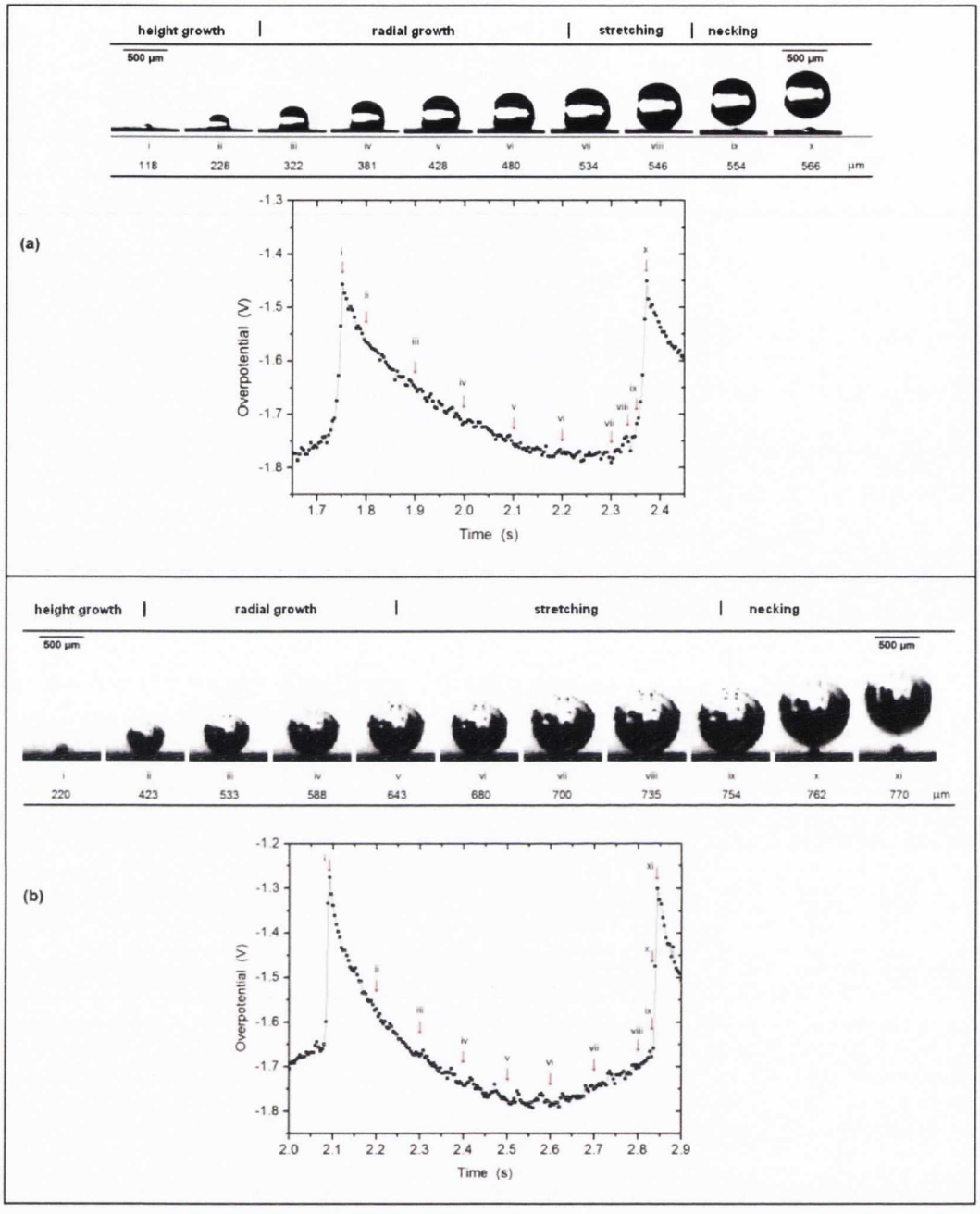

Figure 5.7: Overpotential fluctuation associated to the growth of a single bubble of hydrogen on a Pt microelectrode of 125 µm in diameter, facing upwards. The bubble size, oscillation amplitude and release frequency change with the applied current density j. (a) j = 10 A·cm^{-2}, f = 1.8 Hz, and (b) j = 20 A·cm^{-2}, f = 1.1 Hz.

The gas gathers as a single phase in the volume of the observable bubble. Further gas production leads to bubble growth until it stretches upwards, figure 5.8(c). Although there is still no free electrode surface, the reaction rate is increased by this stretching movement which enhances local mass transfer, progressively reducing IR. This is seen as a slow decrease of the oscillation amplitude from a maximum value η_{max}. When the bubble is in its final detaching stage, figures 5.8(d) and (e) the ions can access to the surface through the neck in a similar way to that of the initial stage. This is represented by the return to the baseline in the waveform.

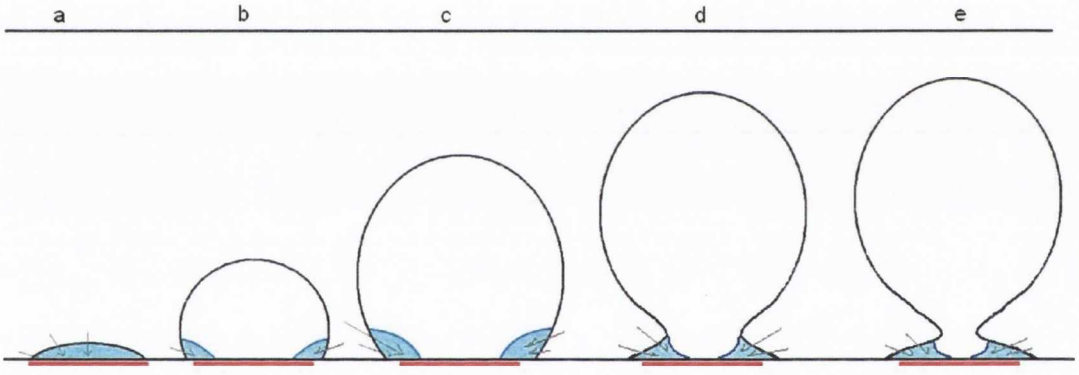

Figure 5.8: Scheme relating bubble size and ohmic contribution to the overpotential oscillation. The blue areas indicate the least resistance pathway between solution and substrate. In (a) the thin gas layer is nearly-equally resistive in all its volume. In (b) only the volume near the three-phase point maintains a similar access pathway, so the reacting volume is diminished. In (c), (d) and (e) the stretching bubble refreshes solution into the three-phase point, increasing the reacting volume.

The shape of the waveform or oscillation pattern also reveals details of the bubbling dynamics.

Figure 5.9 shows different shapes of the overpotential oscillation for a Cu microelectrode (ϕ = 125 μm). In order to show how reproducible these results are, each graph shows two sets of data, corresponding to different runs in identical conditions. According to the stages identified for figure 5.7 and 5.8, regarding bubble shape and their corresponding IR contribution to the overpotential η, the bubbles produced in (a) yielded maximum area coverage right on departure – observed as a sharp return to the baseline from the overpotential maximum amplitude η_λ, achieved after progressive η increment.

In this case, three events, namely the achievement of maximum bubble size $\phi_{b.max}$, maximum area coverage θ_{max} and bubble departure, happen simultaneously. This can be described with the following nomenclature:

$$t_{\phi_{b,max}} = t_{detach} = t_{\theta_{max}} \tag{5.4}$$

However, these times do not necessarily coincide. The oscillation pattern shown in 5.9(b) indicates that the time for maximum area coverage $t_{\theta_{max}}$ occurs at approximately two thirds of the time elapsed for one growth/detachment cycle, t_{detach}. After that, there is a slow reduction of the measured overpotential, which indicates that area coverage diminishes from that time onwards, until the bubble breaks off. This is due to a slower detachment process, and may be described as:

$$t_{\theta_{max}} < t_{\phi_{b,max}} = t_{detach} \tag{5.5}$$

The patterns in (c) and (d) appear to be variations of the behaviour observed in (a) and (b). According to direct observations and the analysis

of the waveform, patterns (c) and (d) may represent a more complex bubbling behaviour. It is possible to suggest the following explanations. In (c) a longer stretching stage may occur, with a more drastic change of shape before necking and breaking-off. In (d) η_λ does not change; it follows that the coverage does not recede or increase. This indicates that there is no significant stretching of the bubble or further radial growth. Since the reaction is ongoing, one likely explanation is that streams of very small bubbles may depart from the electrode while one central bubble is maintained over the electrode until its departure.

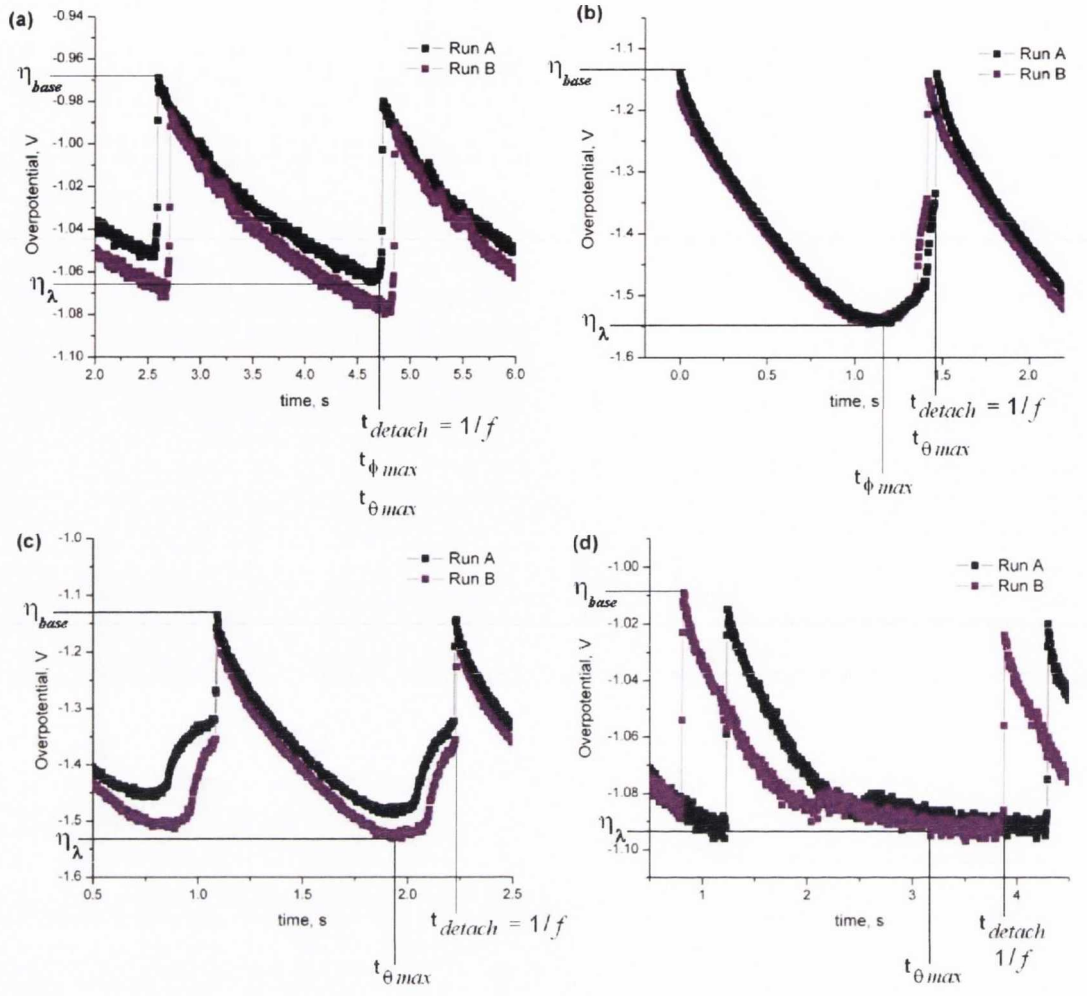

Figure 5.9: Different shapes of overpotential oscillations in the time sequence, associated with IR contribution of the sitting bubble. In order to show how reproducible these results are, each graph shows two sets of data, corresponding to different runs in identical conditions. The maximum oscillation amplitude η_{λ} is related to the time of maximum coverage $t_{\theta_{max}}$. The time of detachment t_{detach} and of maximum bubble size $t_{\emptyset_{max}}$ however, not necessarily coincide with $t_{\theta_{max}}$. In (a) the bubble detaches when reaches maximum size and substrate coverage. In (b) detachment is initiated at $t_{\theta_{max}}$ but occurs later at t_{detach}, when the bubble has reached its maximum size. In (c) and (d), from the waveform shapes, it is inferred a more complex detachment process, with probably a longer stretching stage in (c) and liberation of smaller side bubbles in (d).

V.1.2 Electrochemical noise analysis and structure of power spectra density.

The oscillatory pattern found in chronopotentiometry is also clearly seen when the signal is converted from the time to the frequency domain via fast Fourier transform. The use of this algorithm has been proven a robust and reliable tool to analyze the electrochemical noise of gas evolving electrodes [71]. In the case of corroding systems, studies have been conducted using non-invasive methods such as the analysis of the electrochemical noise, which has proven a reliable technique [62, 71]. However, gas evolving electrodes present quite complex dynamics, and several processes need to be separately identified from the electrochemical noise (EN) analysis, combining the time sequences and power spectra density (PSD) of the treated signal. Fluctuations of the voltage during hydrogen evolution on Fe electrodes were attributed to the ohmic effect of the insulating bubbles covering the electrodes surface [62]. The ohmic contribution was also identified by comparing Pt and Pd electrodes behavior during hydrogen evolution [68]. The use of second species in co-reduction diminished the ohmic component of the obtained PSD for Pt electrodes [65].

Figure 5.10 shows the noise spectra obtained with the same 125 μm Pt microelectrode facing upwards, for different fixed current densities. Power spectra density graphs show relevant information of the single bubbles at frequency ranges below 100 Hz. A main peak is found for each current density, followed by its harmonics. The main peaks correspond to 6.9, 3.6, 1.8 and 1.1 Hz for 1, 5, 10 and 20 $A \cdot cm^{-2}$, respectively. This clearly indicates the periodic characteristic of the bubbling regime in the studied systems. The closest single event analyzed by PSD found in literature for gas evolving electrodes, is the coordinated release of several bubbles from the circular edge of Pt electrodes ($\phi \geq 500$ mm), described as "gas oscillator" behavior, which was

reflected in the PSD as a main peak at the frequency of the bubbles release [72].

A plateau of the spectrum is identified for each signal below 1 Hz. Similar plateaus have been related to the ohmic component of the signal [72]. In agreement, Figure 5.10 shows that, below 1 Hz, datasets collected at higher current densities present plateaus positioned higher in the PSD. Since in this system the bubble size increases in proportion to the current density, also does the IR contribution, hence the associated plateau is shifted upwards. At the same time, bigger bubbles have longer residence times and thus their release frequency is lower, and the main peaks shift to the left.

The spectra present a roll off following a $1/f^2$ relationship. This has been identified as characteristic of coalescence processes [73] and is seen in most of the power spectra for gas evolving electrodes presented in literature [62, 65, 68, 71, 72, 75, 76]. The single bubble dynamics, as observed from the corresponding photographs of Figure 5.7, show no apparent coalescence process. However, the time sequences show smaller fluctuations within the main cycle. This is clearer in Figure 5.7(b), where sub-cycle oscillations of the same shape are seen, especially towards the maximum coverage η_λ. These may be related to coalescence processes at the base of the bubble, unresolved by the camera but evidenced from the electrochemical noise analysis.

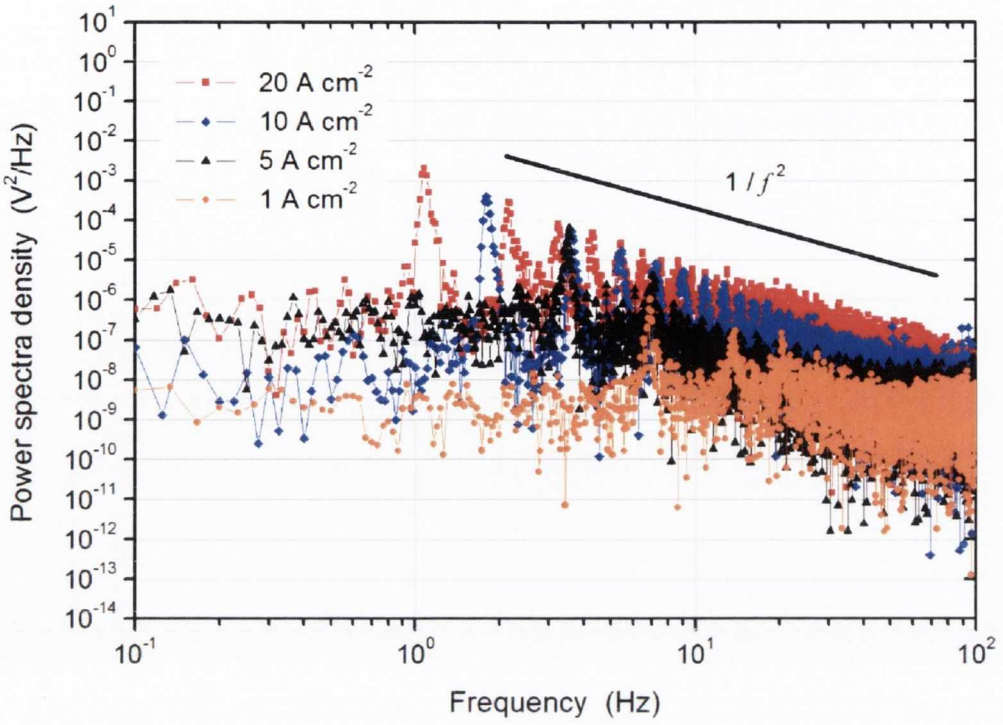

Figure 5.10: Power spectra density (PSD) for the overpotential signals taken at different applied current densities, and focusing in the range below 100 Hz, which shows relevant information. A plateau related to the IR contribution is followed by a main peak which marks the frequency of bubbles release, and a $1/f^2$ roll-off indicating a coalescence process. The plateau and main peak values are related to bubble size, and determined by current density. Higher current produce larger bubbles which produce larger ohmic resistance, observed as a higher plateau, and are released at longer $1/f$ periods.

In the previous section, the IR contribution to overpotential oscillations was related to a change in the reacting volume during the growth cycle of the bubble. The following elaboration on what occurs in the restricted reacting volume (at the rim of the bubble) aims to relate also coalescence evidenced by noise analysis. After the electrochemical reaction:

$$2H + + 2e- = H_{2\,diss} \tag{5.6}$$

molecular hydrogen gas is stored in dissolved form in the solution until a saturation point is reached. The solution can however store more gas without producing a bubble, reaching the super-saturated. Such solution eventually undergoes phase transformation, as:

$$Ssat\ solution\ = gas + solution \tag{5.7}$$

where a mixture transforms into 2 new phases by successive aggregation mechanisms. Firstly molecular aggregation (corresponding to nucleation of a bubble) followed by aggregation of molecules to the existing bubbles (corresponding to growth) and finally bubble-bubble aggregation. The latter corresponds to coalescence.

This may occur at small scales, since coalescence of hydrogen nanobubbles has been evidenced by AFM [77, 78]. This may also be the case at the rim of the bubble next to the 3-phase point, where a mixture of reaction products can be found. Figure 5.11 proposes a coalescence model at the inner rim of the bubble. Here, the smallest bubbles aggregate to the bigger ones progressively, incorporating into the big ("single") bubble observed during the experiments. The merge of small bubbles is sensed electrochemically and evidenced by noise analysis, but is not sensed optically in our setup.

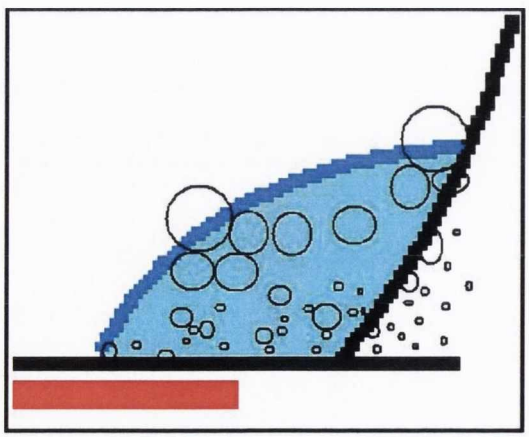

Figure 5.11: Scheme of proposed coalescing process at the inner rim of the bubble.

V.1.3. Summary

The results of this section show that, for hydrogen evolution at Cu and Pt microelectrodes from diluted solutions of sulfuric acid, single bubbles of gas can be produced periodically. The periodicity of the cycle of hydrogen bubble formation and release gives as a result a characteristic oscillation of the measured overpotential. The fluctuation corresponds with the ohmic contribution related to the screening effect of a bubble sitting on the electrode surface. The amplitude and frequency of the oscillation are determined by the detachment process, as well as by the mass flux or current density. In this system, higher current densities lead to higher bubble sizes.

The periodic fluctuations were related to bubble size by considering the frequency of release in galvanostatic conditions. The correlation between calculated and observed sizes of bubbles is above 90%. This corresponds to very high gas efficiencies, not reported previously in literature. However, our results agree with Vogt's model relating mass transport, electrode coverage, gas efficiency and current density via the Sherwood coefficient [63, 64].

Following simultaneously the bubble formation dynamics with high speed photography and electrochemically, the oscillation waveforms produced could be inferred in terms of the stages of bubble formation. Height and radial growth, stretching and necking stages were identified for each cycle. These were related to parameters of the waveforms such as η_{base}, η_{λ}, $t_{\theta_{max}}$, $t_{\phi_{max}}$ and $t_{detac\,h} = 1/f$. The time required for each stage determines characteristic oscillation waveforms.

Bubbles grown in the conditions studied cover at almost all times the entire microelectrode surface. Hence, the oscillation is interpreted in terms of changes of the primary current distribution in an already

resistive system. A model related the IR contribution with shape changes of the bubble and corresponding changes of the conducting volume.

The power spectra density of the measured signal shows the ohmic contributions of the single bubble at frequencies below 100 Hz. There, a plateau is seen, located higher as larger is the bubble size and correspondingly its ohmic contribution. This is directly proportional to the current density. A very sharp main peak, and its harmonics, shows the break off frequency of the single bubbles, which is lower for larger bubbles, due to their longer residence time before release.

The power density spectra follow a $1/f^{2}$ roll off, related to coalescence. No coalescence dynamics was detected by the high speed images, but the oscillation waveform shows sub-cycle fluctuations that may indicate the presence of coalescing bubbles at a much smaller scale at the base of the bubble, unresolved by the camera.

V.2 Physicochemical conditions and bubble size

The site of electrochemically produced hydrogen bubbles is affected by several factors related to the stability of the interfaces in the three-phase system (solid-liquid-gas). In this subsection, relevant factors related to the physicochemical nature of the system, such as substrate and electrolyte composition, are studied.

V.2.1 Substrate nature

The use of different materials as reaction substrate has an impact on the frequency and size of the released bubble. Figure 5.12 shows an example, where vertical copper and platinum microelectrodes of 125 mm in diameter host the hydrogen evolution reaction from electrolytes of the same composition.

A lower frequency of release is seen for platinum, which indicates that platinum tends to stabilize hydrogen better than copper on its surface. This is expected, as copper is a less catalytic material for the hydrogen reduction reaction. Platinum and copper exhibit different adsorption free energies for hydrogen [79]. Literature indicates that platinum is a good host of the reaction and that it adsorbs Hydrogen more strongly than copper. This has been proven by comparing the hydrogen evolution reaction produced on Pt and Cu-coated Pt microelectrodes, finding that hydrogen currents were lower for the case of copper [80].

Accordingly, Figure 5.12 demonstrates that, for a reaction occurring at the same current density and electrolyte, bubbles grow for shorter time on the copper electrode surface. Since bubbles are bigger for

the Pt electrode, this material is selected for most of the experiments regarding hydrogen bubbles in this study.

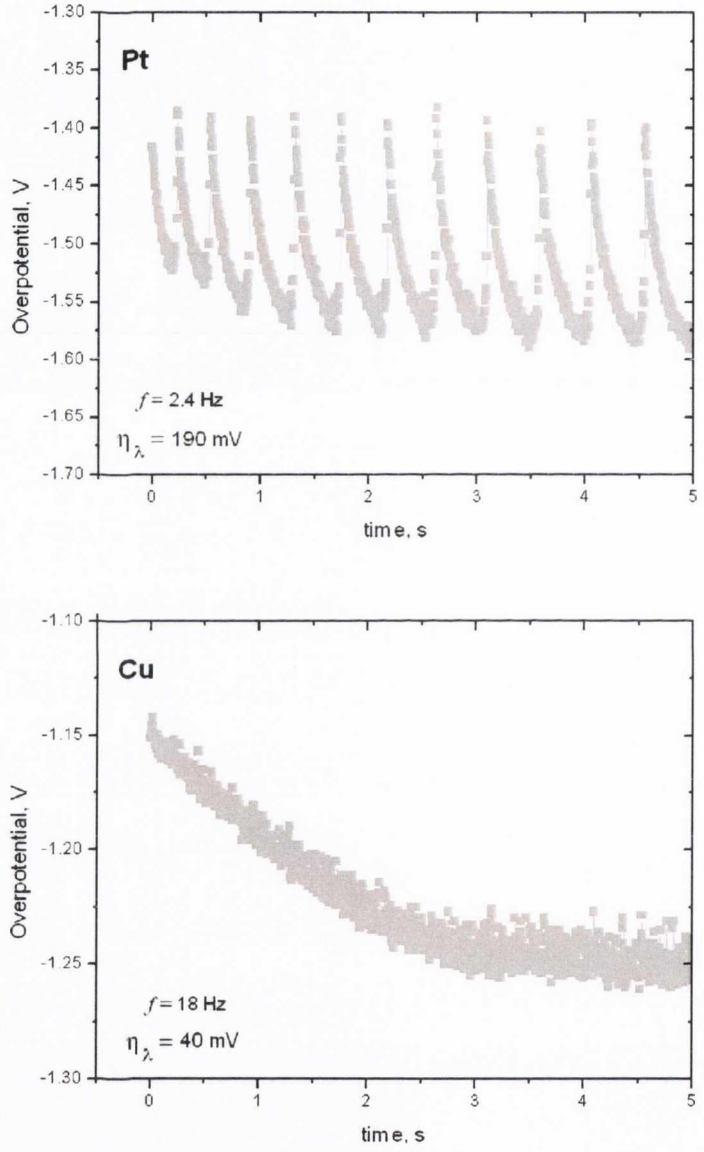

Figure 5.12: Effect of substrate materials Cu and Pt on the frequency of bubble release. Vertical ϕ = 125 mm electrodes under j = 10 A·cm^{-2}.

V.2.2 Concentration of surfactant sodium dodecyl sulphate, SDS

The use of sodium dodecyl sulphate (SDS) as surfactant to reduce the surface tension of liquids and also as a bubble stabilizer is well documented [81]. In order to test the effect of reducing the liquid/gas surface tension on the bubble size several doses of SDS were added to the 1.2 M H_2SO_4 solution.

As expected, hydrogen bubbles produced at the electrode were reduced in size by increasing the SDS additions. Together with the reduction in size a disruption of periodicity is observed. This is seen clearly in figure 5.13. The average size goes down as 580 -> 150 -> 100-> 80 ->60 -> 50. The transition of bubbling dynamics to a non-periodic regime is observed already with 0.03 g/L SDS.

The average size of bubbles is dramatically reduced with increased SDS additions. Together with this, a fluctuation in the size range is observed around the transition concentration. The variation in size is very narrow towards both extremes 0 and 4 g/L SDS, but wide around 0.12 g/L SDS. From the videos, it is clear that the larger bubbles are produced by coalescence around the edges or by collision after break off. The images in figure 5.13 attempt to show this.

A plot of the average bubble size as a function of SDS concentration is shown in Figure 5.14(a). A steep change in size is evident in the presence of the surfactant. At first sight is apparent that a critical concentration value might be in action. However, the interfacial area produced per time unit, calculated considering spherical shaped bubbles and a constant gas flux (volume per time unit), increases progressively with SDS concentration, as shown in (b). Panel (c) shows the corresponding gas/liquid surface tension of the solutions, reduced monotonically and without any critical value regarding SDS content.

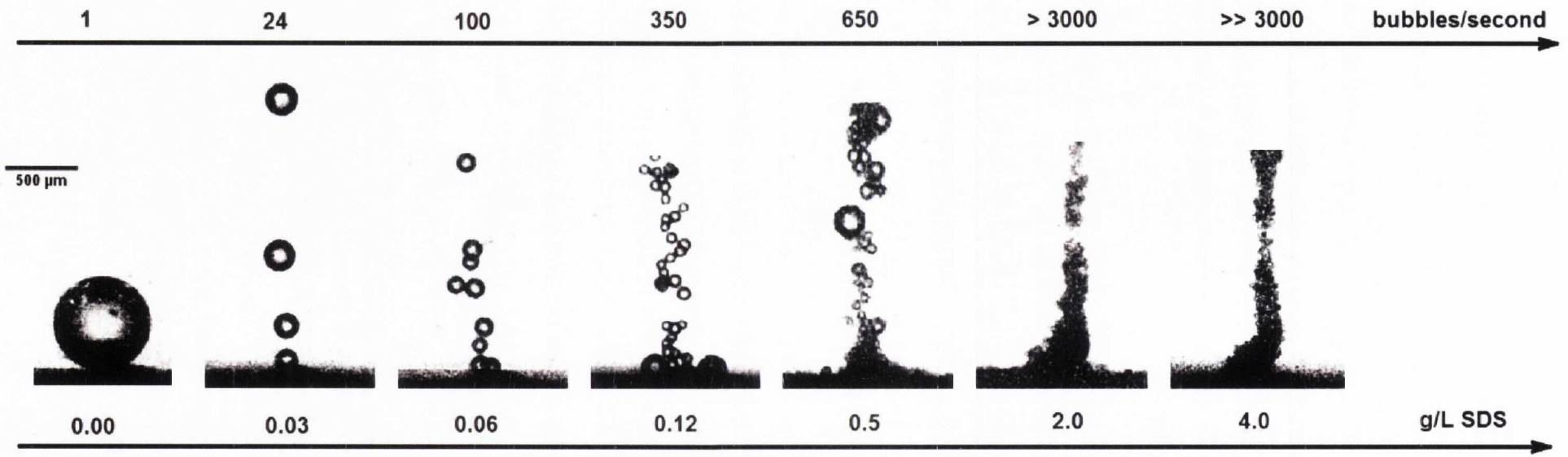

Figure 5.13: Variation of frequency of release with change of surface tension, by additions of sodium dodecyl sulphate.

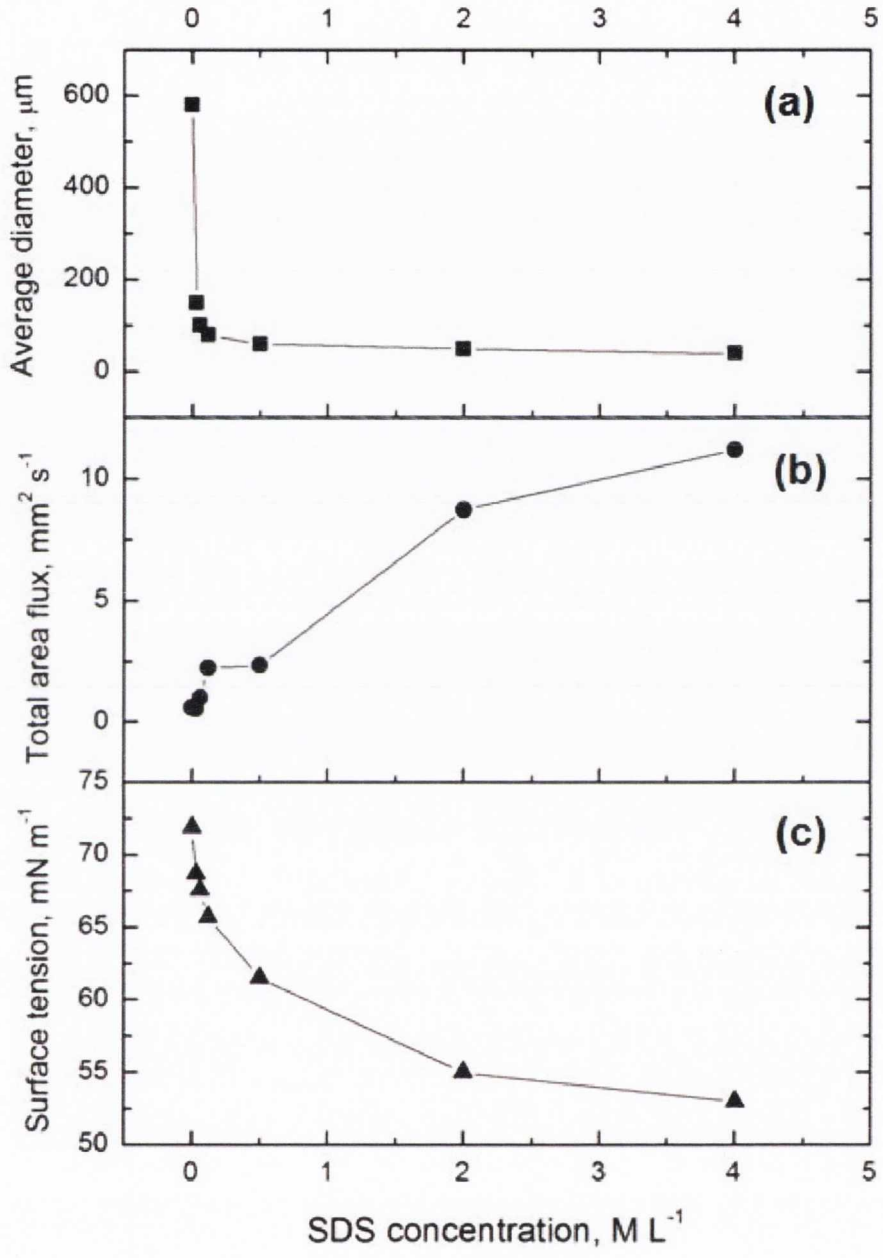

Figure 5.14: (a) Changes of average bubble size as a function of SDS concentration. (b) Interfacial area per unit time produced in relation to the surface tension of the solution. (c) Corresponding gas/liquid surface tension.

V.2.3 Ionic strength

The concentration of ions in solution was changed in order to observe the effect of ionic strength on bubble size. Since bubbles growth contributes to the overpotential with ohmic drop, the changes in conductivity associated with the ionic strength of solutions was analyzed. The composition of the four electrolytes tested is shown in table 5.1, associated with their corresponding ionic strength, conductivity and surface tension. The ionic strength is calculated as:

$$I = \frac{1}{2} \sum_{i=1}^{n} c_i z_i^2 \tag{5.8}$$

It is seen from the table that addition of sodium sulphate produces a strong reduction of surface tension. It is expected that surface tension for multicomponent solutions is the sum of the increments produced by each solute when alone in the same solvent, according to:

$$\Delta\sigma = \sigma_{solution} - \sigma_{solvent} \cong \sum_i \Delta\, \sigma_i \tag{5.9}$$

However this equation fails when a second species of positive ions are present in sulphuric acid solutions, as has been explained by Young [82]. Thus, this solution presents an interesting property, since although ionic strength and conductivity are increased by sodium sulphate addition the surface tension is strongly reduced.

Solution composition	Ionic strength, M	Conductivity, $mS \cdot cm^{-1}$	Surface tension, $mN \cdot m^{-1}$
0.1 M H_2SO_4	0.25	46	71
1.2 M H_2SO_4	3.	300	72
1.2 M H_2SO_4 + 0.1 M Na_2SO_4	3.75	350	60
4.0 M H_2SO_4	10	400	75

Table 5.1: Properties of electrolytes used to test the effect of ionic strength on bubbles formation.

Figure 5.15 summarizes the effects found. Increments in bubble size were obtained for both less conductive and higher conductive electrolytes, provided that surface tension was also increased. When conductivity increased but surface tension was reduced, periodicity of the signal was disrupted and the bubble size dropped to an average value of ϕ = 200 μm. A very similar experiment was conducted in copper microelectrodes immersed in diluted sulphuric acid by Kristof and co-workers [83], however the oscillations they reported were not associated with ohmic contribution of bubbles. Sodium was also added to the solution and a "salting-out effect" where oscillations were disrupted, however no explanation was provided.

The reduced conductivity produces an effect in bubble production. Yang and co-workers found that less current was used to produce bubbles potentiostatically [78]. Accordingly, an increase of voltage was observed in our galvanostatic experiments. Since here the flux is fixed, bubble size is not expected to change unless surface tension is modified. In effect, the change in ionic compositions has a corresponding change in surface tension which agrees with shift in bubble size. The same is valid for all other cases.

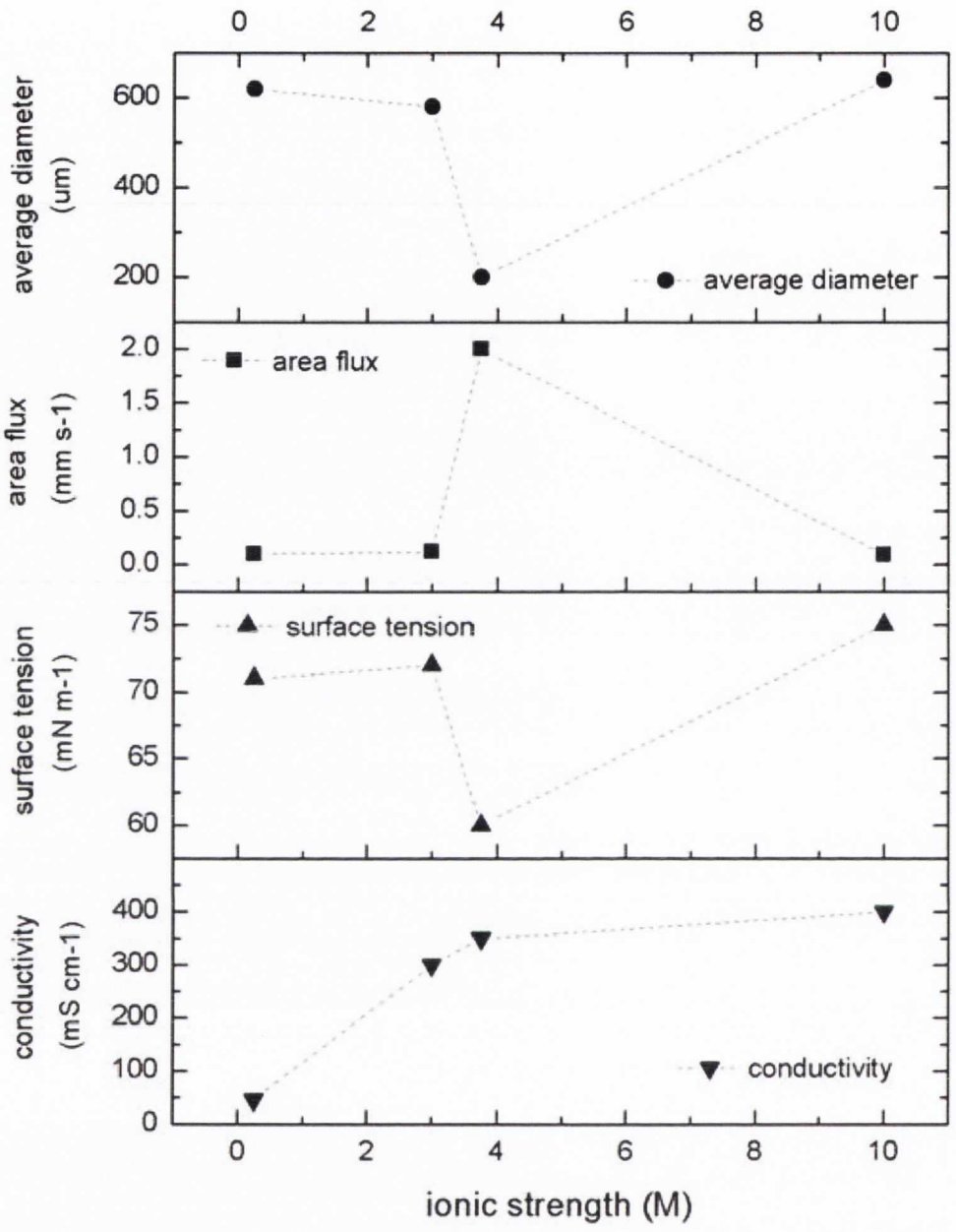

Figure 5.15: Changes of average bubble size for electrolytes of different composition. The average size of bubbles and the corresponding interfacial area produced per time unit is plotted as a function of the ionic strength of each electrolyte, according to Table 5.1. The associated properties of surface tension and conductivity are also plotted. Clearly, conductivity has little or no effect on bubble size compared to surface tension.

V.2.4 Concentration of ethylene glycol, EG.

The electrolyte viscosity was changed in order to observe its effect on growth of bubbles. Ethylene glycol (EG) up to 13% in weight was added to the 1.2 M H_2SO_4 solution. The associated change in viscosity has been estimated from tabulated data for water + ethylene glycol mixtures [84] and for water + sulphuric acid mixtures [85]. An increase of electrolyte viscosity from 1 to 2 mPa·s was estimated for solutions containing up to 13% in weight of EG, with a reduction of surface tension from 74 to 62 $mN \cdot m^{-1}$.

Figure 5.16 shows images of bubble production obtained for a system producing bubbles at a current density of 10 $A \cdot cm^{-2}$, with different concentrations of EG added to the solution. It is seen that not only the average size of the bubbles is strongly reduced from 500 to 50 μm in the presence of EG. Also, the characteristic single-bubble production was disrupted in its presence. With 0.375 % EG, the bubbles grow as small as 70 μm and as big as 400 μm, with no periodicity in their release, as the images clearly show. For higher EG contents the bubble size range is narrowed again, with a lower average value.

Also, a stream regime is fully established upon higher ethylene glycol additions. Images in 5.16 show the transition clearly. It is evident that with EG additions above 0.75% many bubbles of approximately 50-70 μm sit at the same time on the electrode surface. The EG effect is similar to that found with surfactant SDS.

Ethylene glycol changes both viscosity and surface tension progressively. Both are considered to explain the bubble regime transition. Figure 5.17 shows the average bubble size, total area produced and the associated liquid properties of surface tension and viscosity, as a function of EG content. Surface tension is reduced by EG additions, which allows higher area production, i.e. higher number of

bubbles per time unit. There is a consistent relation between surface tension and area flux for both EG and SDS case, indicating that it determines bubble size. However, with EG area flux values are slightly lower. There is a sustained increase of viscosity, which hinders bubble detachment. This probably affects coalescence process, since a higher contact time between multiple bubbles would promote their association into one. From the pictures is seen that coalescence is already present for the first EG aliquot, and that bubble swarms are in any case less numerous for EG-containing solutions.

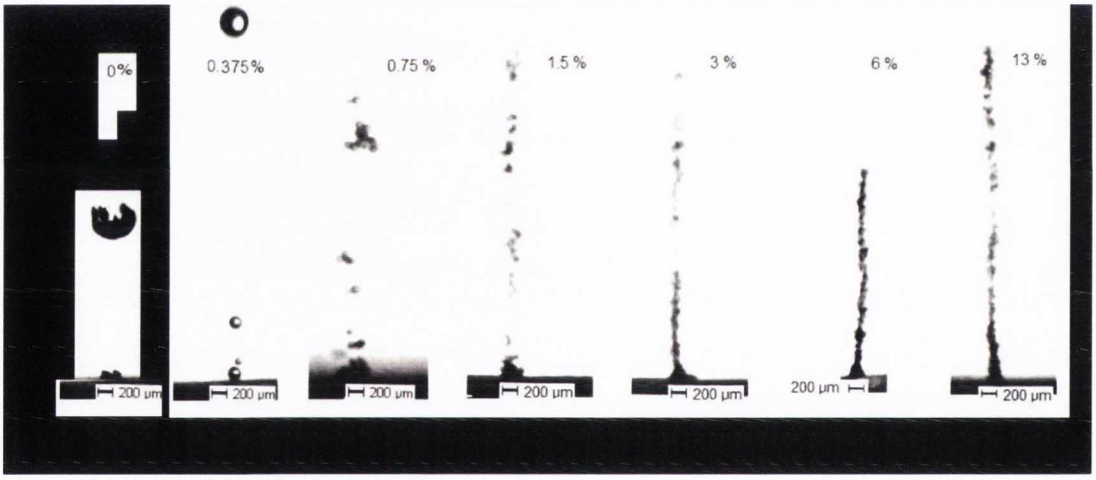

Figure 5.16: Transition from evolution of single-bubbles to streams by addition of ethylene glycol to the electrolyte.

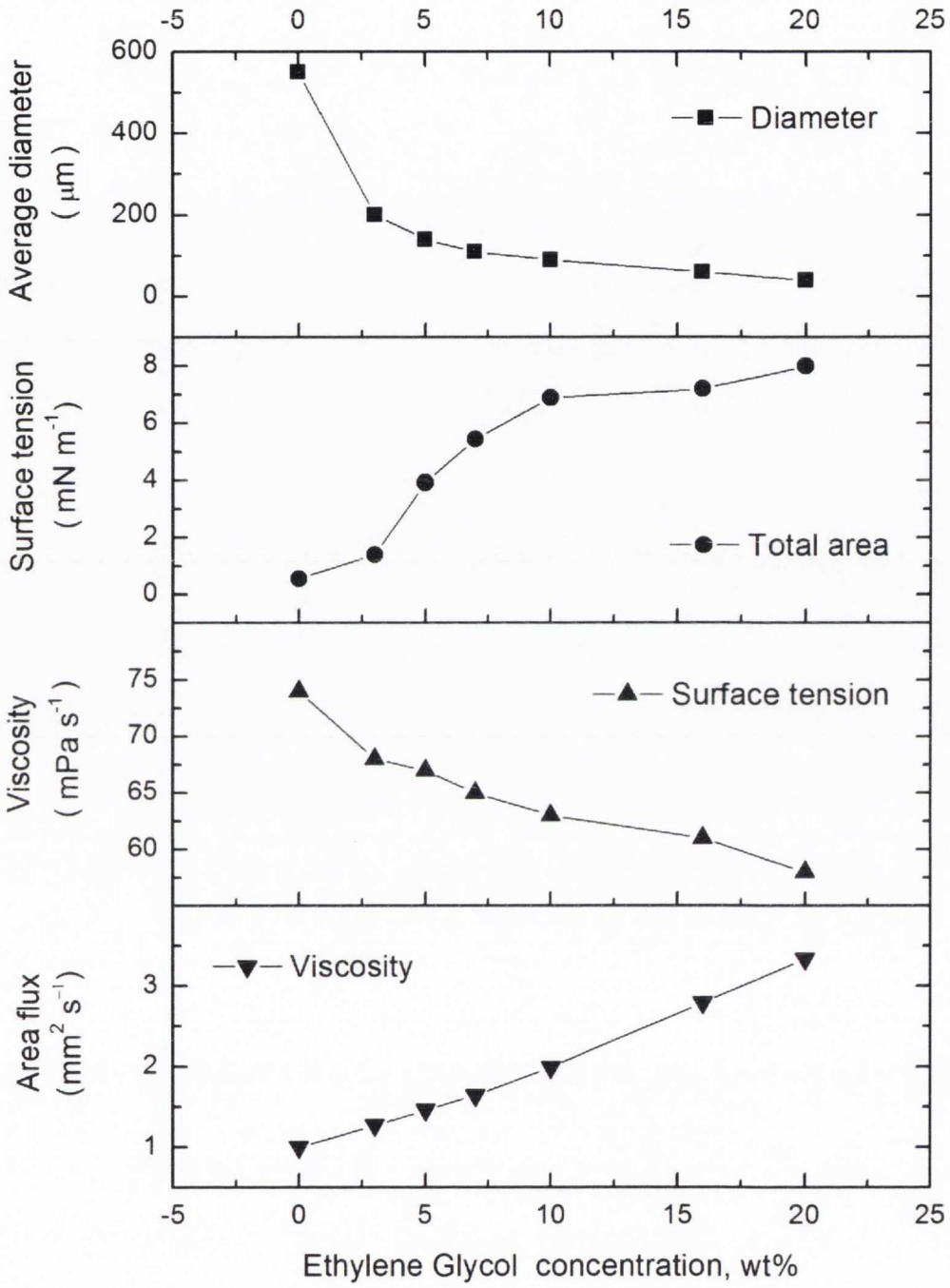

Figure 5.17: Changes in bubble formation due to additions of ethylene glycol (EG). The upper panels show the changes in average bubble size and interfacial area produced per unit time as a function of EG concentration. The lower panels show the corresponding gas/liquid surface tension and viscosity.

V.2.5 Summary

In this section, the physicochemical conditions of the system have been considered. The substrate material, content of surfactant, ionic strength, conductivity and viscosity have been studied. Their role on the production of single bubbles or swarms has been investigated considering both their main-related effect, such as changing viscosity or conductivity, but also taking into account their influence on the interfacial properties.

Copper substrates produced smaller bubbles with respect to those evolved from platinum electrodes, as expected from their catalytic properties for hydrogen evolution reactions.

For current densities of 10 $A \cdot cm^{-2}$, single bubbles were in all cases produced provided that the liquid-gas surface tension σ was around 70 $mN \cdot m^{-1}$. This was accompanied by a single characteristic bubble size and by periodicity of release. Bubbles could in some cases be counted by eye, as their sizes were above 0.5 mm in diameter.

On a totally opposite behavior, clouds of very small bubbles whose sizes were only observable with a high speed camera and magnification lenses, were released from the electrode with no periodicity. In all these cases surface tension was lower, around 60 $mN \cdot m^{-1}$. A particular characteristic of these swarms is that size distribution here was also uniformly small. They presented bubbles around 50 μm in diameter and no presence of larger bubbles was observed. This indicates that coalescence didn't occur at such low values of σ, suggesting a stabilizing effect of the surfactant.

A third, intermediate regime was found for solutions with surface tension around 65 $mN \cdot m^{-1}$. In these cases, a wide size distribution is observed, with small, medium and large bubbles simultaneously seen.

The electrochemical signal showed smaller and more ample oscillations, with no periodicity.

These observations suggest that solutions around 60 mN m^{-1}, allowed the production of high interfacial area. No coalescence occurs even though the bubbles remain in close contact over the electrode surface and upon break-off. This leads to the formation of froth, where bubble's surface is stabilized via additives [86], which also reduce surface tension.

The progressive widening of current distribution when surface tension increases, around 65 mN m^{-1}, indicates that a transition occurs. The videos showed bubbles joining to form bigger ones. The coalescence happens both at the surface and after breaking-off. This suggests that the higher tension value introduces certain instability which inhibits area production. Upon further increase of surface tension, area formation is even more inhibited, leading to an extreme reduction observed as the formation of single bubbles of 5 times larger diameters.

The different variables tested proved to have little effect on bubble size, compared with that of surface tension. A chart relating the bubbling regime with electrolyte properties and the corresponding tension is shown in Figure 5.18. It is clear that coalescence is inhibited at lower values of σ, changing through a transition regime to a favored state at the highest σ values.

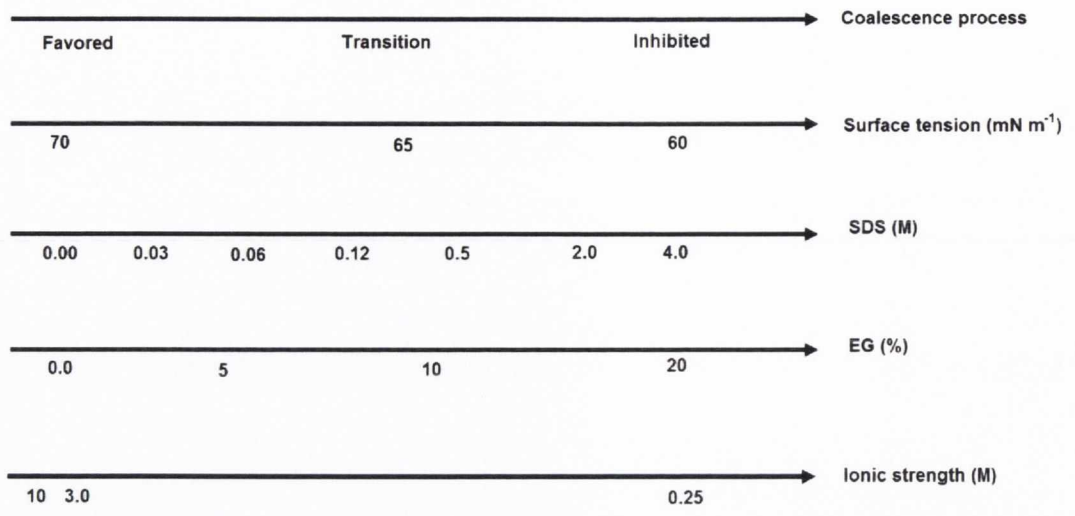

Figure 5.18: Chart showing the degree of bubble coalescence in relation to surface tension values, for different compositions of the electrolyte. The ionic strength, content of ethylene glycol and sodium dodecyl sulfate were considered, and are aligned in relation to their corresponding values of interfacial tension.

V.3 Magnetic field effect on growth of single hydrogen bubbles

In this section, the effect of electrode position relative to both magnetic fields and gravity is studied. The simultaneous effect of the three factors has usually been ignored, and most times only the relative position of the electrode surface with respect to the magnetic field is considered. Here all possible configurations of the electric and magnetic fields with respect to gravity are analysed, and we describe not only the effect of field intensity but also of field polarity.

V.3.1 Lorentz and upthrust forces

Figure 5.19 show that there are five possible combinations of mutual orientation of field to electrode surface to gravity that can be used to study the bubble formation from the electrode. The magnetic fields are applied either horizontally (B_H) or vertically (B_V) to electrode surfaces located vertically (S_V) or horizontally facing up (S_H). Since the action of gravity through the upthrust force F_{UP} is taken into account for the analysis, electrodes facing downwards are not considered.

It can be seen that, working out the field polarity and the sense of current lines on such configurations, Lorentz forces F_L acting in three different ways are expected. In a first group, F_L acts horizontally, i.e. perpendicular to F_{UP}. This occurs in some combinations of fields parallel ($\parallel$) to the electrode surface, namely $B_V \parallel S_V$ and $B_H \parallel S_H$. A second group includes F_L acting vertically, i.e. parallel to F_{UP}. This is the case of configuration $B_H \parallel S_V$. In a third group, F_L acts azimuthally either in a horizontal or vertical plane. This is the case where fields are perpendicular to the electrode surface, namely $B_H \perp S_V$ and $B_V \perp S_H$.

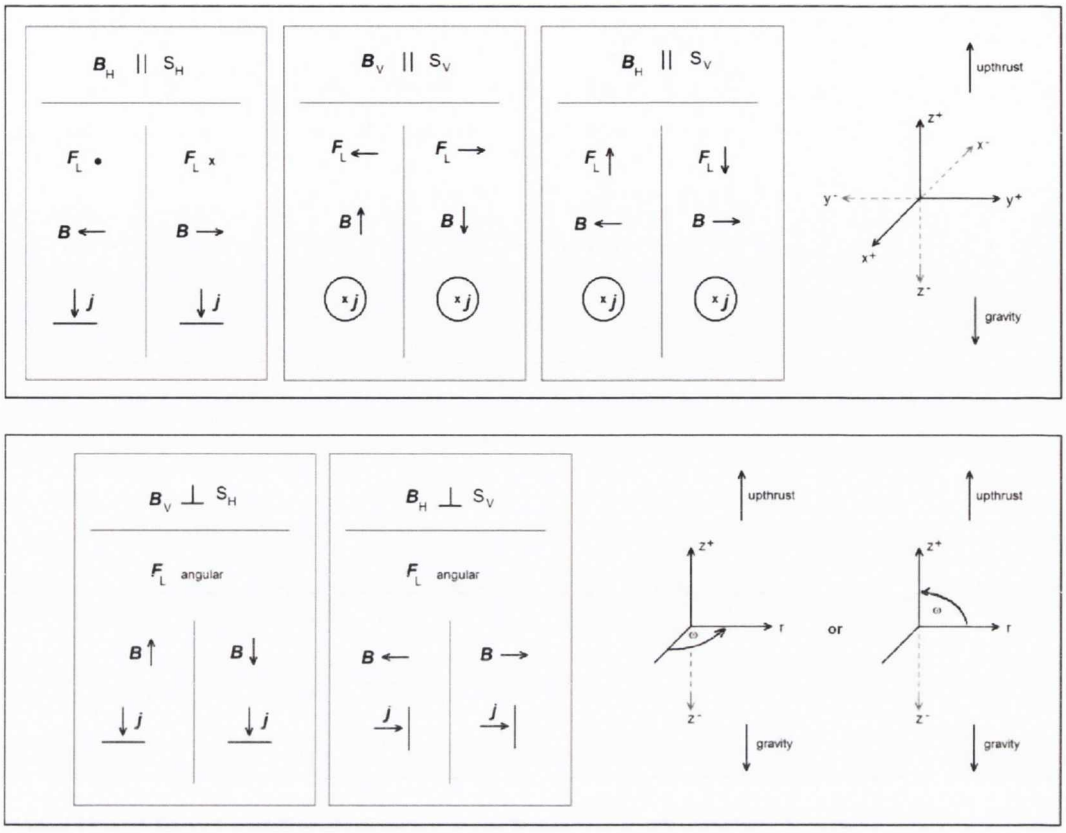

Figure 5.19: Possible position combinations of magnetic field and electrode surface for freely-evolving bubbles.

V.3.2 Lorentz force acting horizontally

The first case is the $B_H \parallel S_H$ configuration. The effects found here were found independent of field polarity.

Figure 5.20 shows the changes in overpotential oscillations when a horizontal magnetic field of 1.5 T is applied to the Pt microelectrode, at a fixed current density j = 10 A cm^{-2}. The oscillation frequency changes f from ~2 Hz at 0 T to ~35 Hz at 1.5 T, indicating that the bubbles are released faster under field influence in this configuration. Also the waveform baseline shifts upwards, to lower overpotentials, when the fields are applied. This indicates a lower coverage under field.

Figure 5.21 shows the relation between bubble size and direction of departure in relation to field intensity. Progressive steps of 500 mT change the bubble size and sweep the bubbles off the electrode surface in the direction of the Lorentz force. The stream bends, accordingly, and then regains verticality, following the cylindrical cell geometry.

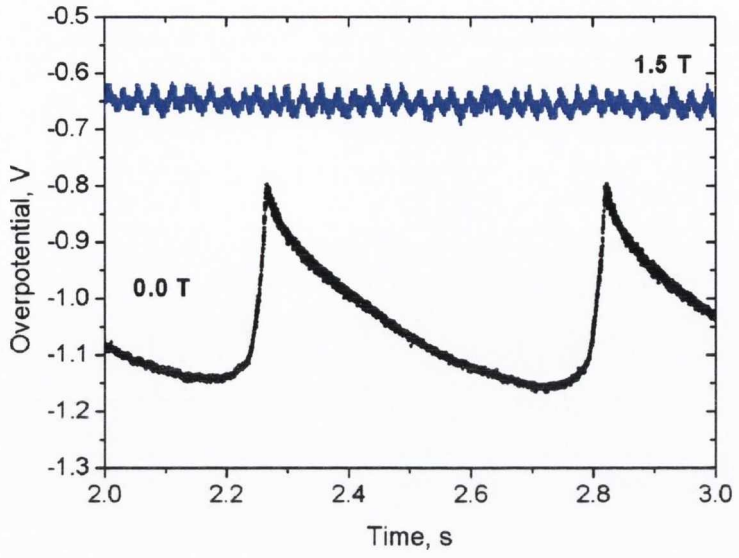

Figure 5.20: The field effect on overpotential oscillations indicating reduction of bubble size for the configuration $B_H \parallel S_H$. Pt microelectrode, 1.2 M H_2SO_4 electrolyte.

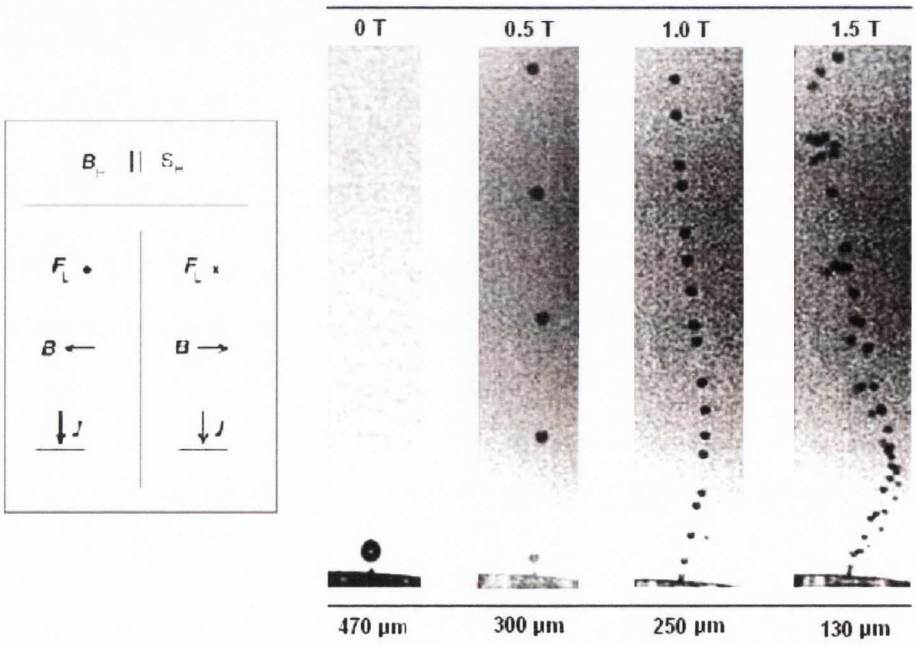

Figure 5.21: Reduction of bubble size by effect of a magnetic field in configuration $B_H \parallel S_H$, same as in Figure 5.20. This effect is independent of field polarity.

Results obtained with a $B_V \parallel S_V$ configuration are shown in Figures 5.22 and 5.23. In this case a copper microelectrode is used, located vertically in the bore of the superconducting magnet. Fields up to 5 T are applied. The time sequences in figure 5.22 correspond to the overpotential oscillations measured when a current density of j= 10 A cm^{-2} was applied and the PSD in figure 5.23 to the corresponding frequency spectra of the measured signal.

The release frequency, seen from the oscillations in figure 5.22 is increased from 2 Hz at 0 T to 2.5 Hz at 1.5 T, which corresponds with the PSD of panels (a) and (b) whose main peak indicates the periodic nature of the bubbling regime in these cases.

The time sequences at 3 and 4 T show a transitional regime, where single big bubbles are only sporadically released, and loosing periodicity among swarms of smaller bubbles. With 5 T, big bubbles were no longer observed. The corresponding noise spectra are shown in panels (d), (e) and (f). The former main peaks progressively widen and flatten, indicating total loss of periodicity. The results obtained for both $B_H \parallel S_H$ and $B_V \parallel S_V$ configurations were found independent of field polarity.

In is then clear that, in configurations where F_L acts horizontally, the magnetically-induced convection sweeps the bubbles off and as a consequence shortens their time for growth. Although this was expected from reports in literature [87, 88] quantifications of the size change have not been made for single bubbles, neither a transition on the bubbling dynamics due to the field has been previously quantified.

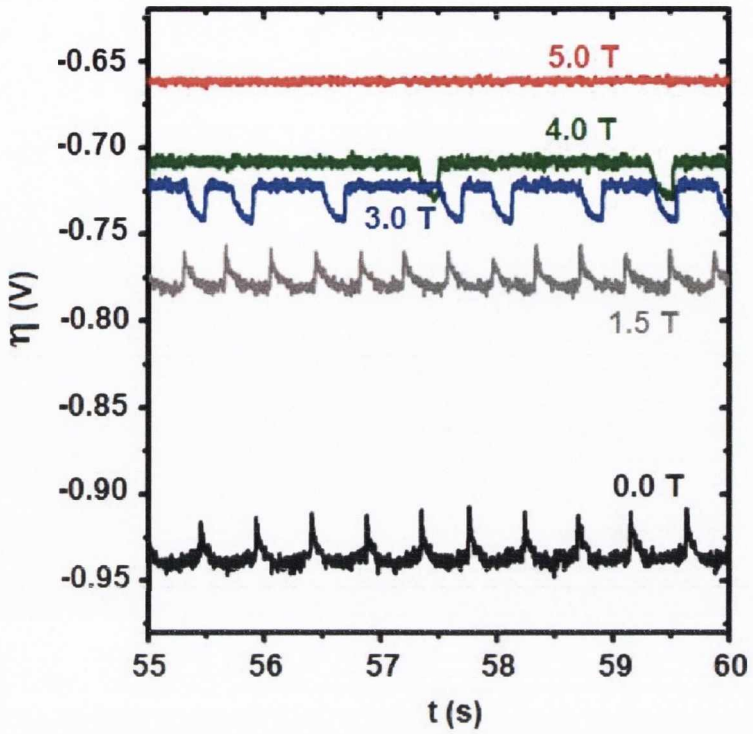

Figure 5.22: Transition from periodic single bubbling to aperiodic regime in the $B_V \parallel S_V$ configuration. A copper 125 μm microelectrode was maintained at j = 3.5 A cm^{-2}. Periodicity of bubbles release is found up to 1.5 T; at 3 and 4 T small streams of bubbles evolve, with sporadic release of one big bubble. At 5 T only streams of small bubbles are released with no periodicity.

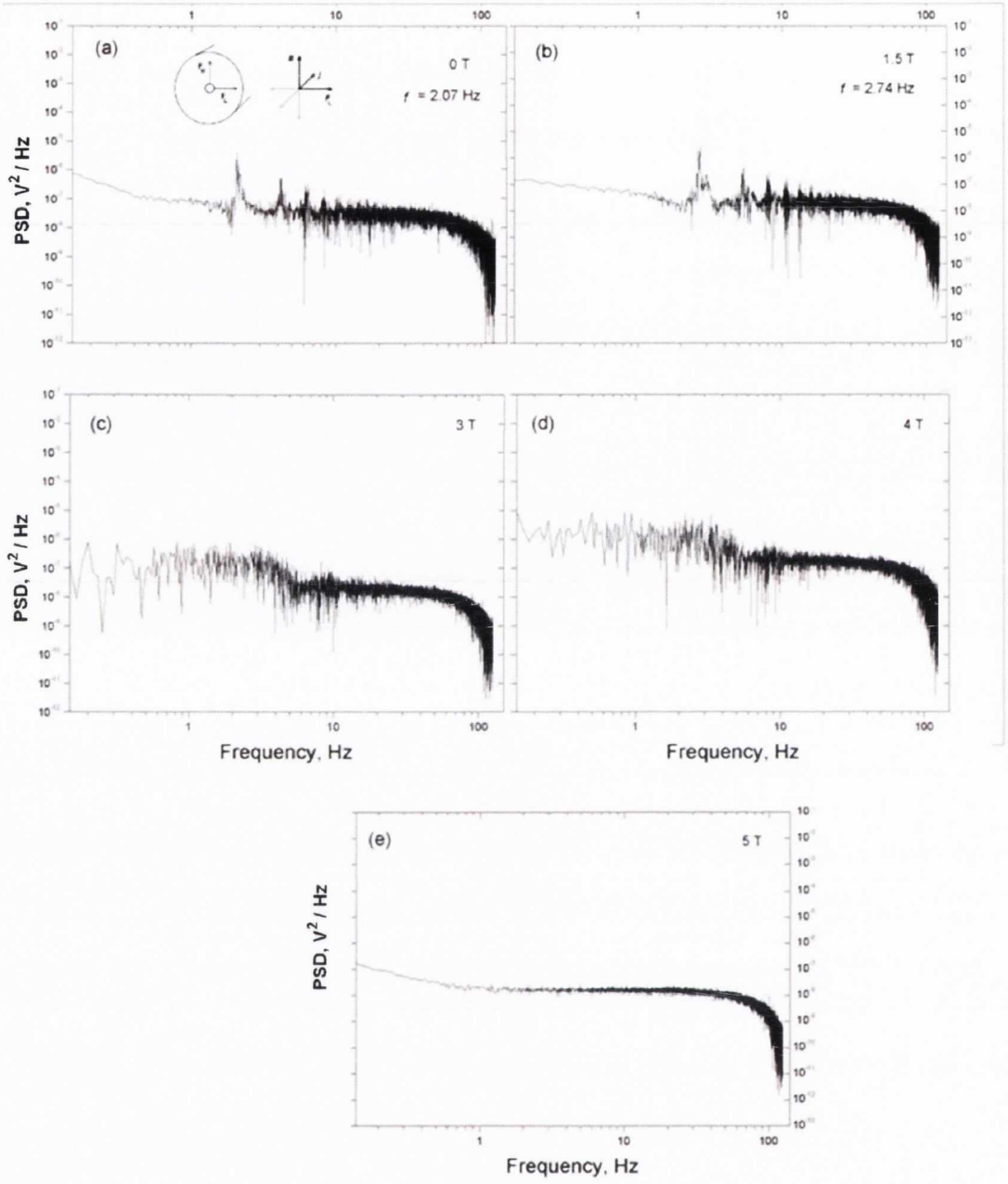

Figure 5.23: Electrochemical noise spectra at low frequency range for the conditions of figure 5.22, with $B_V \parallel S_V$ configuration, showing transition from periodic to aperiodic bubbling. The periodicity in (a) and (b) is indicated by the main peak, which broadens progressively in (c) and (d) until it the spectrum is flattened in (e)

V.3.3 Lorentz force acting vertically

When F_L is parallel to gravity $B_H \parallel S_V$ configuration, contrary to all other cases, the polarity of the resulting vector makes a difference. In other words, it depends on the sense of Lorenz force. Figure 5.24 shows this clearly. When F_L, acts upwards, the bubble size becomes smaller than for zero field, and aperiodic. In this case the bubbles are moved off the electrode surface with help of both Lorentz force and upthrust. This is seen on the images and confirmed by the flat signal at the low frequency range of the power spectrum density in (b).

For the same $B_H \parallel S_V$ configuration but when the field is reversed and F_L acts downwards, the oscillations are less frequent and with bigger amplitude. Further evidence of the opposition of Lorentz force to bubbles release when directed downwards is seen in figure 5.25. At a constant current density of 3.5 A cm-2, progressive increments of field intensity lead to a frequency reduction from 17 Hz at 0 T to nearly 6 Hz at 1.5 T.

Figure 5.26 summarizes the effect on frequency for both cases j constant or B constant, in terms of the jB product. It is seen that the higher this product, i.e. the Lorentz force magnitude, the slower the bubble release is. According to the previous analysis and correlation with bubble observations, this implies an increase in bubble size with increasing intensity of the applied magnetic fields.

In this case bubbles are stabilized for longer times over the electrode surface, allowing them to grow until upthrust forces them up. This is periodic, as confirmed by the main peak in the noise spectra. This shows clearly that not only does the mutual orientation of B and E have to be considered to understand the effect; also their orientation relative to gravity is crucial.

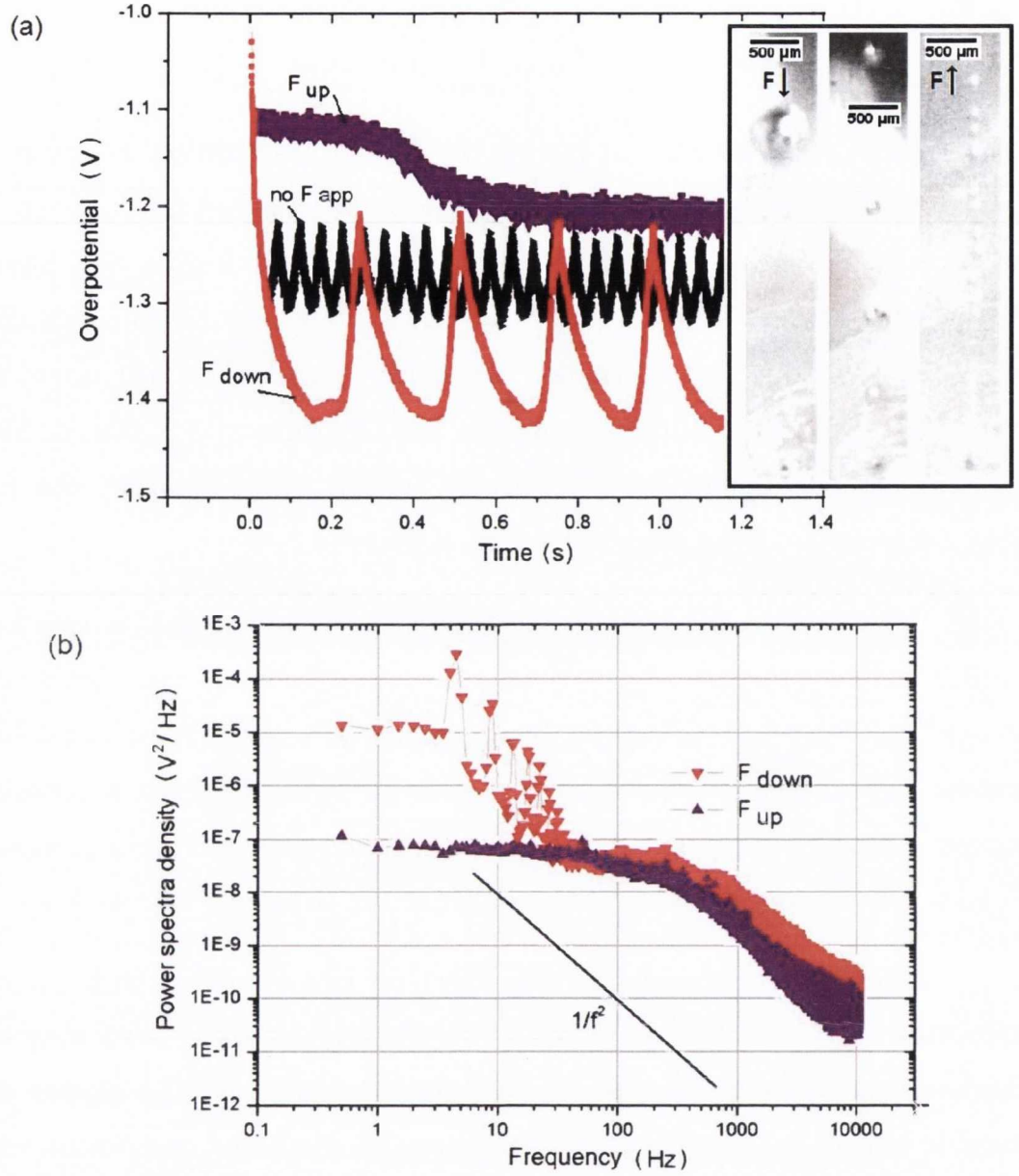

Figure 5.24: Reduction or increase of bubble size depending on field polarity, for $B_H \parallel S_V$ configuration showing (a) the overpotential oscillations and images of the bubbles release, and (b) corresponding changes in power spectra density for both polarities of the field. A current density of 20 A cm^{-2} was applied to a Cu vertical microelectrode, the fields applied were 0 and ± 1.5 T.The residence time is modified by the action a convective force pointing up or downwards. The oscillation patterns change accordingly, and the PSD structure varies in the low frequency range, exhibiting a two-step plateau when IR component prevails.

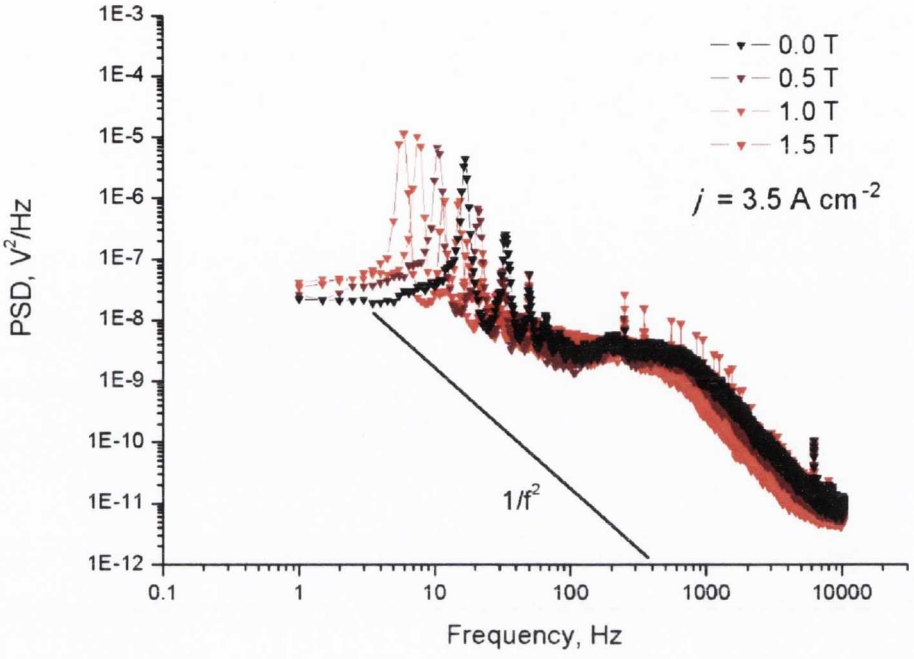

Figure 5.25: Field effect on electrochemical noise spectra, for the $B_H \parallel S_V$ configuration with Lorentz force acting downwards. A copper microelectrode of 125 μm in diameter was used at constant current density of 3.5 A cm^{-2}.

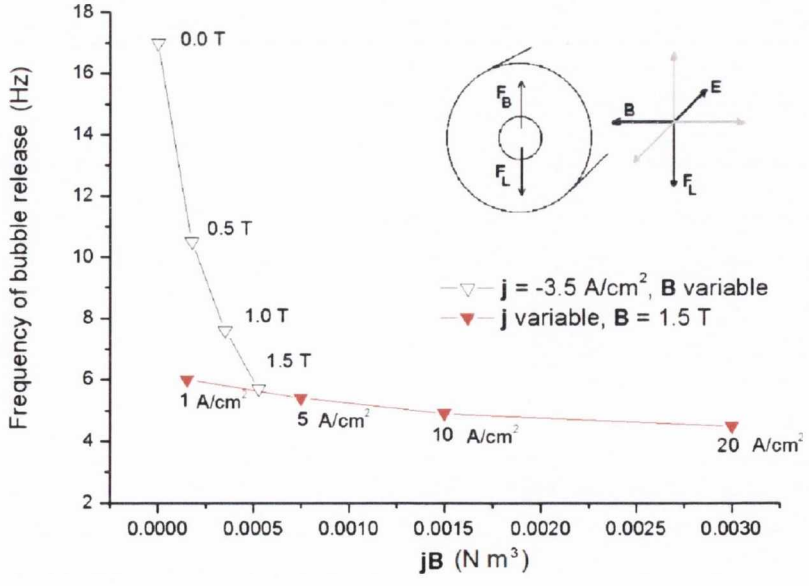

Figure 5.26: Dependence of the frequency of bubble release with Lorentz force magnitude (jB product) for $B_H \parallel S_V$ configuration, when it opposes gravity.

V.3.4 Lorentz force acting azimuthally

Vertical magnetic fields (B_V) were applied to the cell, such that they were orientated perpendicular to the horizontal surface (S_H) of the electrode ($B_V \perp S_H$ configuration). Figure 5.27(a) and (b) show results for a Cu microelectrode. In (a) the time sequences for j = 5 A·cm^{-2} and fields up to 5 T are shown. It is seen that overpotential oscillations become less frequent when fields are applied. By analogy to the effect of applying higher current densities, which reduces release frequency and thus produces bigger bubbles, here higher fields also reduce f. Calculation of the corresponding bubble size using Eq. (5.3) is shown in Figure 5.27(b) for different current densities and fields. The release frequency seems determined by the field intensity rather than the current density. The bubble diameter increases by 60% from 0 to 1.5 T and is doubled with 5 T.

Figures 5.28(a) and (b) show results for the same configuration, using a Pt microelectrode. A similar effect on the oscillations is seen in the time sequence, where j = 20 A·cm^{-2} and fields of up to 5 T were used. The calculated bubble size is shown in (b) for a wider current range than that used for the copper substrate. Here, the release frequency depends on both field and current density. The bubbles diameter increase with a 5 T field by 27%, 34%, 45% and 64% for current densities of 1, 5, 10 and 20 A·cm^{-2}, respectively. A uniform enhancement of 12-13% in diameter is achieved in all cases with 1.5 T.

Figure 5.29 shows the effect for $B_H \perp S_V$ configurations. Clearly, the bubbles produced also take longer time to release under field influence. For the example shown, where a Pt microelectrode is subject to j = 20 A·cm^{-2}, a field of 1.5 T promotes an increase in bubble diameter from 840 to 967 μm. This is higher than the size calculated with Eq. (5.3), which predicts 698 and 913 μm with 0 and 1.5 T, respectively. In the case

of vertical electrodes the residence time is shorter than for the horizontal ones at 0 T, and the same trend is maintained under fields.

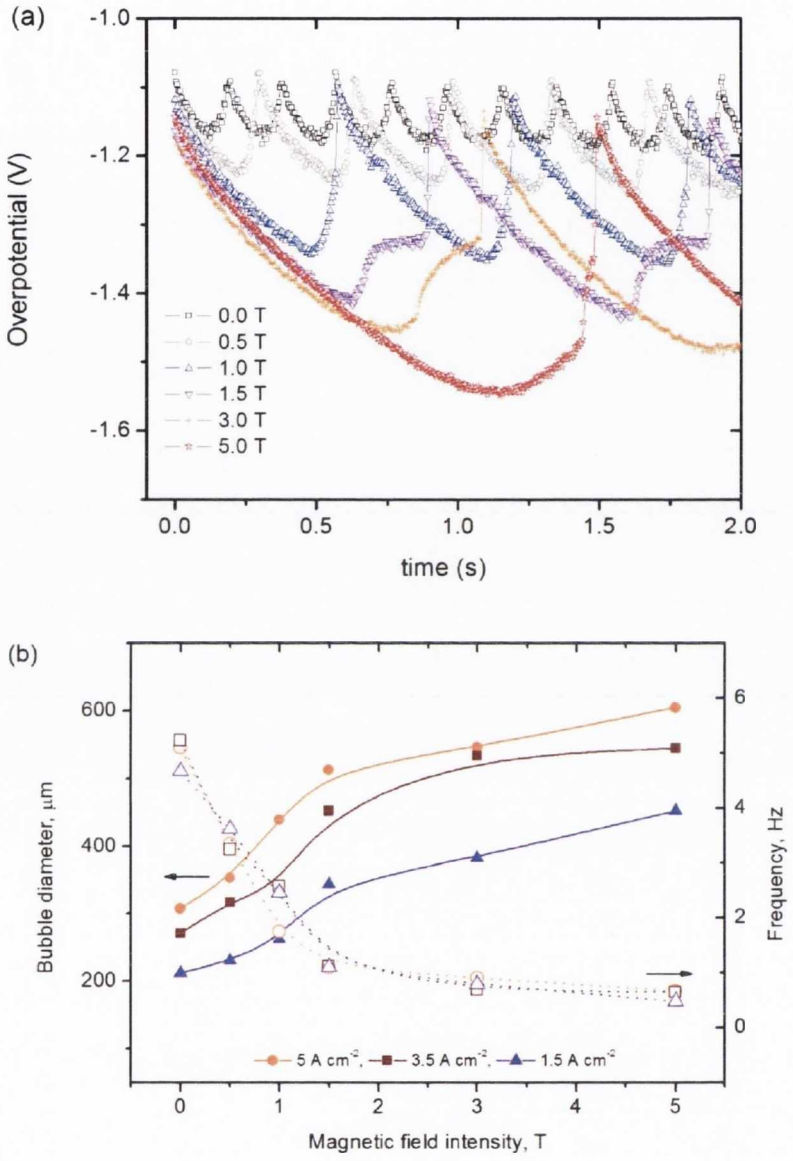

Figure 5.27: Overpotential oscillations and its relation to bubble size for fields directed perpendicular to the electrode surface for B ⊥ S configurations. (a) Time sequences for fields up to 5 T with $B_V \perp S_H$ configurations are shown for Cu microelectrode. The corresponding bubble size and release frequency are plotted in (b). $j = 5$ Acm^{-2}.

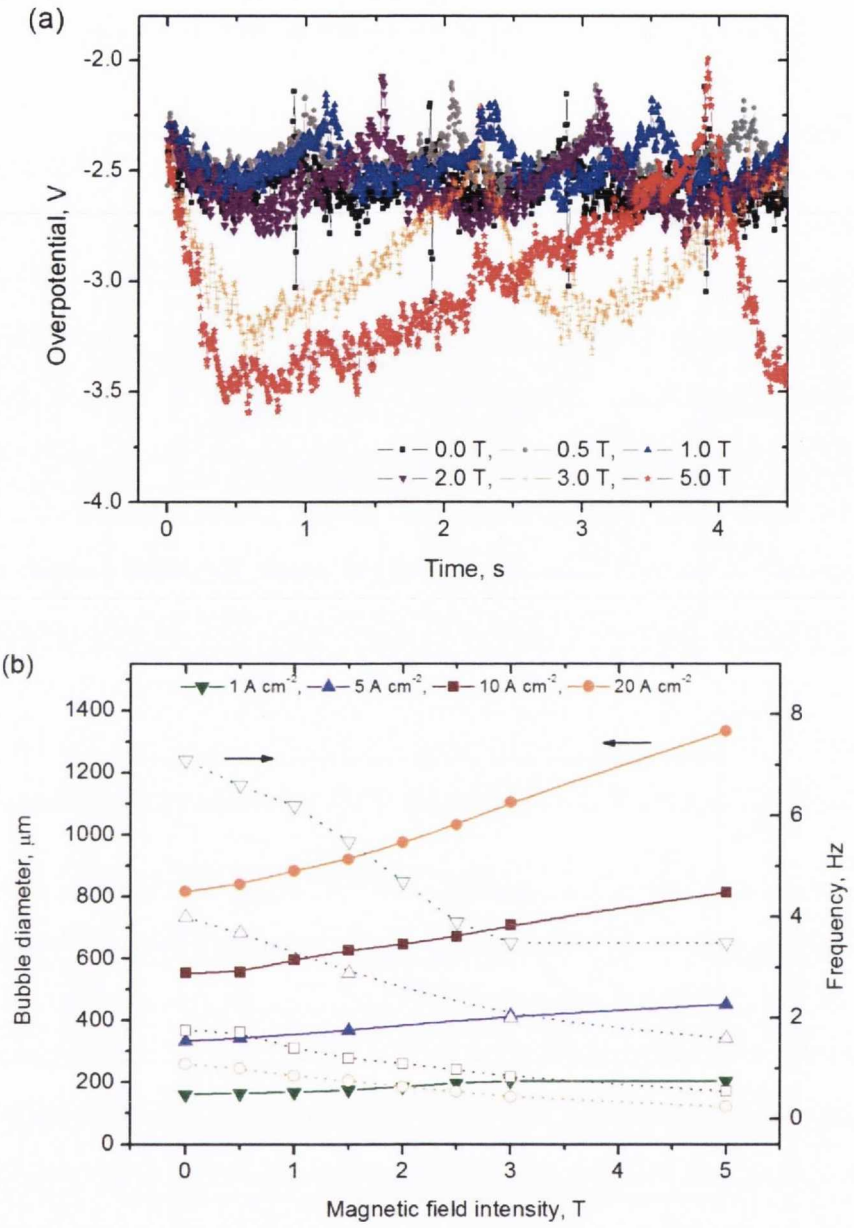

Figure 5.28: Overpotential oscillations and its relation to bubble size for fields directed perpendicular to the electrode surface for B ⊥ S configurations. (a) Time sequences for fields up to 5 T with $B_V \perp S_H$ configurations are shown for a Pt microelectrode. The corresponding bubble size and release frequency are plotted in (b). $j = 20$ Acm^{-2}.

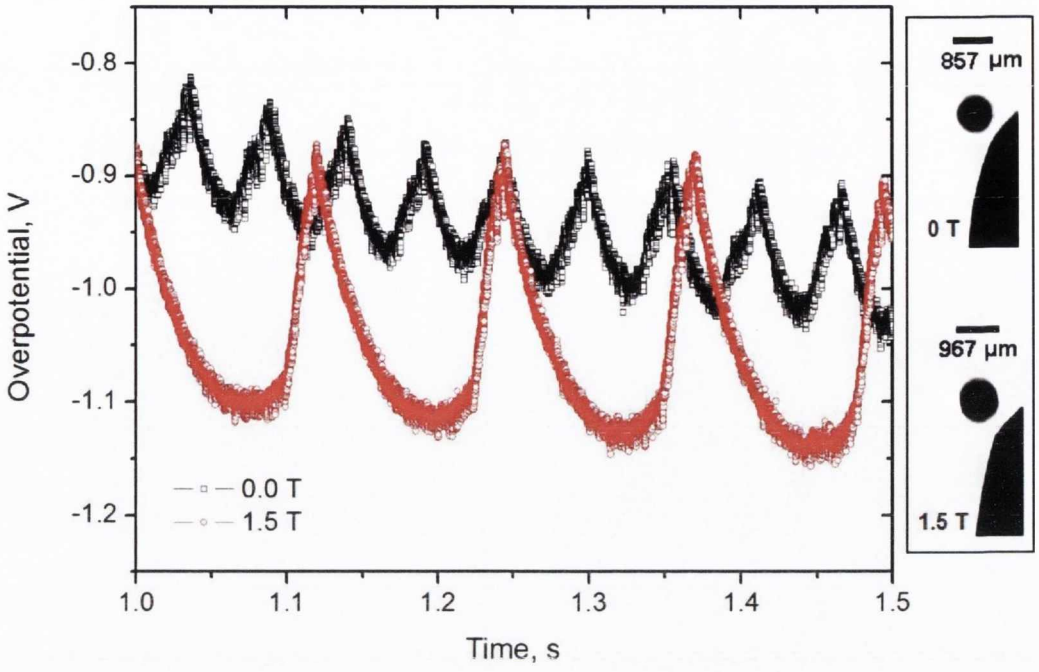

Figure 5.29: Time sequences at 0 and 1.5 T with $B_H \perp S_V$ configurations for a Pt microelectrode. The corresponding images indicating bubble size are seen on the right panel.

In order to follow the flow around a growing bubble, PVC particles have been added to the solution, and the process has been followed with a high speed video camera. Motion tracking images are shown in Figure 5.30 for the $B_V \perp S_H$ configuration. They show the changes of hydrodynamic pattern when the vertical field is applied to the horizontal facing up gas evolving electrode. In this case, the side view was obtained by using a circular Halbach array to apply a uniform vertical field of 0.44 T. The images, calculated by considering the standard deviation of the grayscale point by point, show the track of each PVC particle suspended in the fluid and of the released bubbles. At 0 T particles are settling straight down due to gravity and a few of them are slightly dragged upwards by the motion of released bubbles. When the field is applied, a clear rotational motion is induced around the bubble. The upward movement of the bubbles does not affect the rotational particles' trajectory.

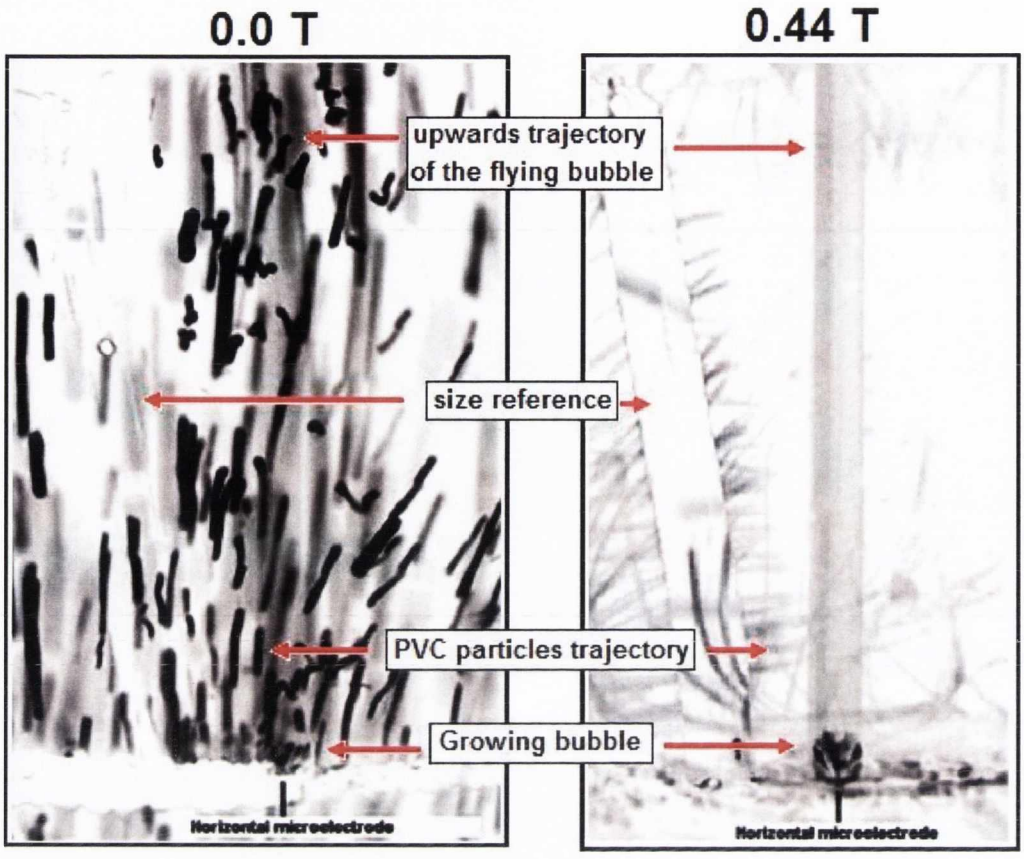

Figure 5.30: Motion track images showing rotational flow for the $B_V \perp S_H$ configuration. PVC particles are used to track the flow. Vertical field applied is 0.44 T.

Figure 5.31 shows motion tracking images for the $B_H \perp S_V$ configuration. Again, at 0 T the particles move only due to gravity or bubbles flying up. The hydrodynamic pattern changes dramatically under the horizontal field. In front of the electrode, toroidal motion is set; particles in the bulk solution move towards it and integrate in. The swirl revolves around a horizontal axis and moves away of the electrode. Particles located at the central axis are directed in a perfectly horizontal line towards the bubble. The trajectory of a particle that hits a bubble is tracked following numbers 1 to 9. After release, bubbles fly up following a 7° angle with respect to the vertical, dragged by fluid motion.

Clearly the tracked flow shown is independent of any gravity or geometrical effect. This type of flow, where an outer swirling-away motion around a central axis feeds an inner flow backwards is known in hydrodynamics as *two-celled vortex* [89, 90]. This corresponds with the observed flow. It is apparent that the two-celled vortex is a secondary flow caused by the magnetically-induced rotation of fluid around the single bubble.

The Lorentz-induced flow around a bubble sitting at the electrode surface was expected to facilitate its departure via a "twist-off" action [75, 87, 88, 91] which would explain the size reduction of hydrogen bubbles in $B \perp S$ configurations. That is however contrary to the observations shown here. The main difference is that in our work one single bubble is formed at a time.

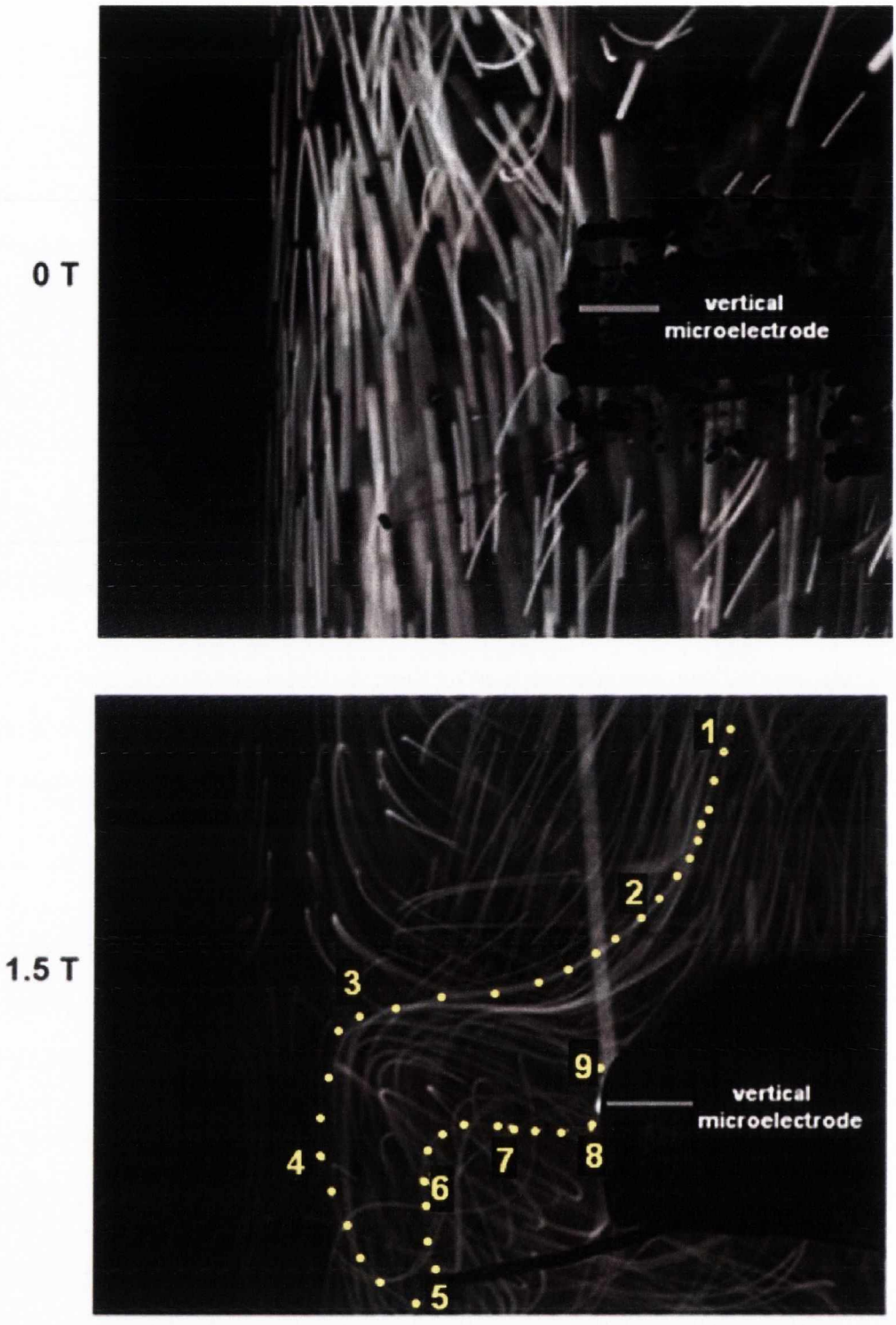

Figure 5.31: Motion tracking image showing rotational for the $B_H \perp S_V$ configuration. Horizontal field applied is 1.5 T. PVC particles are used to track the flow. A two-cell vortex is identified, with an outer swirling away motion feeding an inlet flow backwards to the electrode. The inlet flow is tracked by following numbers 1 to 9.

The evidence suggests that in B $\perp$ S configurations, the Lorentz-induced flow around ***one single bubble*** results in its stabilization on the electrode surface. This occurs not by the action of the rotational flow itself but due to a consequent secondary motion directed axially towards the bubble. Figure 5.32 schematizes this. The inlet flow pushes the bubble against the electrode surface. The balance of forces must consider upthrust, hence the electrode position relative to gravity is relevant. In the case of configurations where $B_V \perp S_H$, the inlet force F_I acts vertically opposing upthrust, while for $B_H \perp S_V$ configurations F_I acts horizontally and upthrust must overcome tangential forces.

For cases where ***several bubbles*** are simultaneously produced at the electrode surface, each bubble can be considered as a singular convective cell with a two-celled vortex structure. If the bubbles are sufficiently far apart so their corresponding flow fields do not interact, they can be considered as isolated two-celled vortexes producing bigger bubbles. However, if the bubbles are situated such that their convective cells can interact, more complex hydrodynamics patterns form. These patterns would have a stochastic nature, influenced by size and distribution of bubbles as well as by the magnitude and trajectory of the flow, which in turn interact and influence each other. Hence, quantitative description of a resulting "sweeping-off" effect may be difficult. Nevertheless, particle image velocimetry and numerical simulations may clarify the resulting hydrodynamics. For this, it is apparent that overlap of the flow fields of multiple two-celled vortexes (the convective cell of each bubble) should be considered.

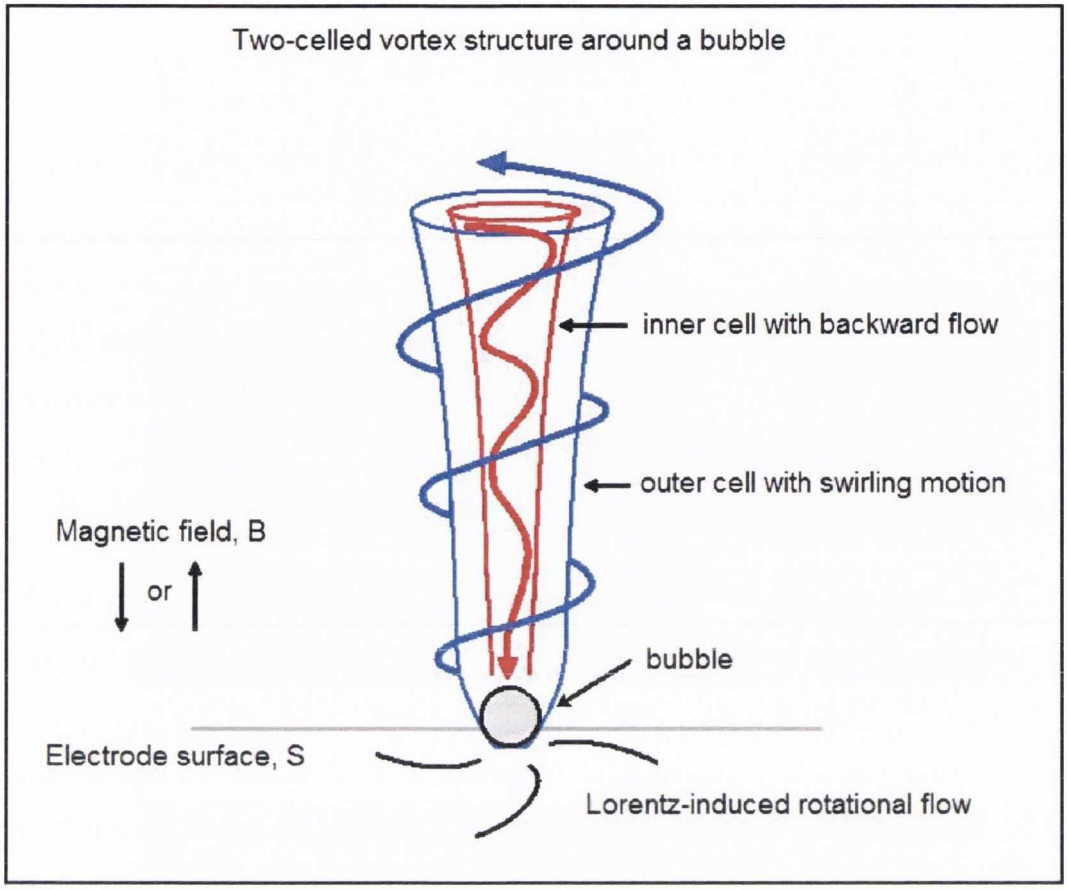

Figure 5.32: Scheme of a two-celled vortex structure due to the Lorentz-induced rotational motion around one single bubble for $B \perp S$ configurations

V.3.5 Summary

The effect of fields on the formation of a single bubble have been clearly related to the interaction between Lorentz and upthrust forces. The convective motion induced by of both affects the time residence of the bubble forming from the interspersed gas molecules close to the electrode area. In consequence, bubbles experience a degree of supersaturation in their surroundings that determines their size.

The electrolytes used to study the field effect were those promoting coalescence, hence the only explanation for the change to aperiodic release of bubble swarms is the inhibition of coalescence by reduction of the contact time, due to the addition of surfactants or via magneto-stirring. Liu established that at least 1 ms was necessary to produce the breakage of the film between adjacent bubbles [92]. This would be around 1000 Hz in the PSD. In the cases studied here, Lorentz forces acting sideways have demonstrated such capacity, especially above 3 T. Similar effect of flow was found by Nguyen [93].

When current densities are below 5 A cm^{-2}, bubble size is lower and is possible to produce the transition more easily. Although the cases with higher current densities were used for the main explanations here, we also found that aperiodic regimes were easily obtained with the lower currents. This agrees with Matsushima who indicates that the supersaturation degree is affected by the field [94], and Kikuchi who has related convection with the concentration of dissolved gas in solution [95]. It is through this value that magnetoconvection and upthrust effects are observable. If there is a high degree of supersaturation, convection sets in faster to promote bubbles formation.

Since supersaturation is directly proportional to current density, higher currents would promote coalescence. In this case, a flow that opposes to bubble break-off increases contact time and thus coalescence

is favoured, while flow that promotes break-off reduces contact time and coalescence is inhibited. The effects are schematized in figure 5.33.

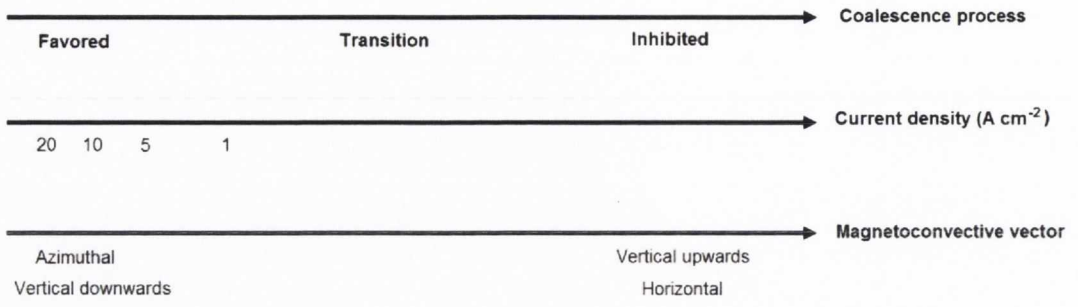

Figure 5.33: Chart summarizing the field and current effect on the transition from single to multiple bubbles. Conditions which determine coalescence in these cases are related to the residence time and solute (dissolved gas) redistribution.

V.4 Discussion and Summary of the chapter

As regards the **field to electrode configuration** and its effect on bubbling, it has been proven experimentally that uniform magnetic fields applied parallel to the surface during the formation of one single bubble promote bubbles sweep-off from the electrode, resulting in change of bubbling dynamics from single-sized to swarms of bubbles released with no periodicity. This is true for the case when Lorentz force acts horizontally, and the effect is independent of field polarity.

When Lorentz force acts vertically, the effect is polarity-dependent and may either increase or decrease bubble size. This depends of the Lorentz and upthrust forces summoning or opposing each other.

It has been proven experimentally that uniform magnetic fields applied perpendicularly to the surface during the formation of one single

bubble promote bigger sizes of bubbles. This occurs due to the azimuthal Lorentz force which produces a rotational flow, inducing a swirling motion which in turn produces a two-celled vortex with inner flow redirected backwards to the electrode along a central axis. This flow pushes the bubble against the electrode, holding it there until upthrust prevails.

In $B_V \perp S_H$ configurations the inner flow acts downwards, opposing upthrust. In $B_H \perp S_V$ configurations the inner flow acts horizontally and upthrust has to overcome the tangential forces of the swirl.

It is apparent hence that there is no "twist-off" effect of a magnetic field for this type of configurations. When multiple bubbles are growing on the same surface it is likely that the flow fields of each bubble repel, giving as a result a "sweep-off" effect that would remove bubbles earlier than at zero field.

As regards the **transition from single, periodic bubble formation to aperiodic evolution of swarms**, the effect seems related to the degree of inhibition of coalescence processes. Although coalescence is evident at the transition stage because it can be visually followed, at the limiting case of single bubble production a more drastic coalescencing process may be occurring.

Nguyen et al studied bubble formation in microfluidics, and the relation of σ and f. They found that high surface tension values lead to lower frequency of bubble production. [93]. This is also the case of our study. Moreover, the electrochemical noise measurements in section V.1 showed a $\alpha = 2$ value of the $1/f^{\alpha}$ relation in the single bubbles regime; according to literature this exponent value indicates that coalescence is taking place [73]. Although unresolved by the images, it is likely that coalescence occurs at a very small scale at the base of the bubble.

Liu et al studied bubble formation and coalescence. They found that coalescence requires a critical contact time between adjacent

bubbles, in which the film of liquid between them thins until it breaks. They found this time is approximately 1 ms, and higher in the presence of surfactants. They also reported that, above certain surfactant concentrations, coalescence was inhibited [92]. Our results agree, since production of bubbles at rates above 3000 bubbles per second (with a residence time of $\leq$ 3 ms) showed no coalescence. The residence time of bubbles on the other extreme of the chart is 3 orders of magnitude higher, allowing plenty of chances for coalescence to occur.

It is probable that the scale range where the inferred coalescence would occur is very small. Evidence of nanoscale coalescence of bubbles was not been claimed, however AFM studies have shown height/width plots where initial states of one single nanobubble resemble 3 smaller spread bubbles [78]. It might be possible that here something similar happens in the case of single bubble formation.

Another related observation is the diameter of the single bubbles. Remarkably, it equals and even exceeds the reacting area during most of the bubbling cycle. This seems to contradict the explanation for the overpotential fluctuation associated with a progressive coverage of electrode area [62, 72, 75, 76].

We proposed a model where coalescing, very small bubbles are constantly joining the big single bubble, from the lower part at its rim. This would explain the coalescing noise, the bubble size exceeding the microelectrode area yet allowing the reaction to occur, and the images showing a transition of size distribution from uniform (single, periodic bubbling, to wide to again uniform swarms, aperiodic bubbling) when surface tension changed.

As regards the **convective action of the field**, in combination with upthrust, determines bubble size in gas evolving electrodes. Bubble size can be reduced or increased by proper combination of convective forces

acting on it. This is achieved by setting the electrode to field position but necessarily also the position of them with respect to gravity.

Interesting observations are those indicating that bubble size was sometimes so small that made the solution cloudy. In those cases, the solution took long time to clear, resembling a colloidal suspension. Also, it was noticeable that the velocity of bubbles swept horizontally off the electrode showed particularly high velocities. Iida and coworkers reported a similar effect under magnetic fields [94].

These observations suggest that, for the case of bubbles swept off the electrode, bubble size is not only be determined by their shorter residence time on the reacting surface. The strong motion around the bubble transports dissolved gas towards the bulk solution. As a consequence, the local concentration of dissolved gas is reduced while the average concentration throughout the whole cell volume is homogenized. A reduced local concentration of dissolved gas near the electrode decreases the driving force for phase transformation. Hence, bubble growth is inhibited due to a change in the composition of the liquid near the electrode.

Similar effects of convection on bubble production have been observed in other systems. Kikuchi et al studied bubbles below 300 nm in diameter produced by water electrolysis, determining that their size is inversely proportional to the hydrogen content of the solution [95]. Tanaka reported that this ratio (H_{diss} / $H_{bubbles}$) increases with flow, indicating that higher flow rates reduce bubble size and recombination, hence the concentration of dissolved hydrogen increases.

Measurements of IR contribution of gas produced during water electrolysis under magnetic fields up to 5 T were performed by Iida, who observed that measured resistance diminished by the magnetoconvective action, explained by a change in the supersaturation degree of the solution [94].

An increase of release frequency was observed by Nguyen when the flow rate was increased [93]. Diminished population of bubbles with increased flow was reported by Eigeldinger and co-workers [96]. Strong reductions in bubble coverage, by 80-90%, were obtained when a flow of 0.5 m/s passed the electrode surfaces.

The effect of convection absence also informs on bubble coalescence. Studies under microgravity have shown that hydrogen tends to coalesce more in microgravity than in terrestrial conditions [97]. Also, that residence time is shorter at 1 G, indicating that upthrust plays an important role in bubble detachment. Bubbles grown in microgravity from a solution having $\sigma = 77$ mN·m^{-1} showed increased coalescence, with a wide size distribution. On the other hand, hydrogen froth was promoted in microgravity when formed from a solution having $\sigma = 70$ mN·m^{-1} [98]. In other words, at conditions where no upthrust lifted bubbles off the electrode, solutions with higher surface tension produced less interface area by coalescence, while solutions with lower surface tension produced more interface by generating a greater number of small bubbles. Since there was no upthrust, the swarms remained attached on the electrode in the form of froth. These observations show, by absence, the effect of convection on bubble size and its relation to the liquid-gas surface tension.

It is thus apparent that magnetoconvection has a two-fold effect on the bubble size. It acts indirectly, by changing the concentration of dissolved gas around the bubble and also directly, by applying a force over the bubble surface.

In the first case, magnetoconvection reduces local supersaturation near the bubble while increases the concentration of gas in the bulk. This produces growth inhibition. As a result, changes in the microscale can be expected. In the second case, magnetoconvective action can also reach the meso and macroscales. The forces on the bubble surface may act

upwards, summoning to upthrust; horizontally, reducing adhesion; or downwards, damping upthrust.

As regards **the effect of current density on the formation of single bubbles,** it was observed that higher current densities increased bubble size and promoted single bubble formation. Studies have reported similar observations in microfluidics [57-59] and electroflotation [60]; in all these cases, the substrate area in micro-sized. Oppositely, other studies –using large electrodes– indicate that higher current densities lead to smaller bubbles [99, 100]. The effect of current density, of flux, is probably related to the local supersaturation conditions. Following the model proposed, the processes taking place at the inner rim of the bubble are faster for higher fluxes, i.e. molecular gas is produced at higher rate and thus the concentration gradient is larger. Homogenization via solute redistribution is not achieved and thus, coalescence takes place as the scheme suggests, promoting single bubbling regimes.

The closeness between bubble size measurement and calculation from the release frequency obeys probably to the high current densities used. The term gas efficiency describes the conversion degree of passed current into bubbles. Although it is usually low, our experiments indicate gas efficiency above 90%, in agreement with Vogt's model, which indicates that in our conditions mass transfer by microconvection prevails.

Chapter VI

Magnetic field effect on growth of metallic copper with secondary gas phase reaction

When different species are dissolved in the electrolyte they may undergo simultaneous electrochemical phase transformation at certain overpotential ranges. The acid copper system presents such situation when dissolved oxygen and water reduce as secondary reactions during copper metallization. These cases are analysed here. Potentiostatic and galvanostatic techniques are used to produce the deposits at the chosen conditions. Electrochemical noise is used to analyze the signal. Deposits are characterized in terms of morphology, roughness and thickness. Current efficiency is studied.

VI.1 Copper and dissolved oxygen

Oxygen gas is almost inevitably present in any solution open to the atmosphere. As it was seen in Chapter I, oxygen gas dissolved in aqueous solutions can be reduced to form water at the cathode according to Eq. (1.2). The equilibrium reaction is about 0.9 V above that for copper reduction, Eq. (1.1). As a consequence, the oxygen reduction reaction (ORR) has a high driving force during copper metallization.

The current ranges observed for ORR are of the order of hundreds of $\mu A\ cm^{-2}$ [101] and are usually negligible with respect to the currents used to produce copper deposits. However at very low overpotentials, copper currents are of the order of 0.5-15 $mA\ cm^{-2}$. Hence, for these magnitudes of the current, the possible interference of the ORR currents must be considered.

Considering the possible effects of presence of oxygen, the magneto-convective influence on copper growth at low overpotential (η = -0.04 V) is analysed here. Different copper concentrations were used to study the chronoamperometry response under fields in the presence and absence of dissolved oxygen. It was found, in agreement with O'Reilly [39], that fields may increase or decrease current values with respect to those measured under no field. A typical response for the case of a 0.1 M $CuSO_4$ naturally-aerated solution is shown in Figure 6.1(a), where a 1.5 T field increases the cathodic current by a factor of 2, in the range of a few hundreds of microamperes per square centimetre. According to Vukmirovic [101] the diffusion-limited current of dissolved oxygen in aerated solutions on copper surface is in this range, with increasing values as convection is stronger. This agrees with a higher current being obtained under magnetoconvective action.

When oxygen was removed from the solution by Argon bubbling, not only were the measured currents dramatically reduced by two orders

of magnitude, also the field influence on them was strongly suppressed, as can be seen in figure 6.1(b). This clearly indicates that the field-enhanced current corresponded to oxygen only, and suggests that it obeys to the enhancement of transport conditions due to magnetoconvection. This is explained as the oxygen reduction reaction, given by Eq. (1.2), is mass-transport limited. When dissolved oxygen is present, the corresponding currents are enhanced by magnetoconvection. When oxygen is removed, magnetoconvection makes no difference on the measured current at this low overpotential.

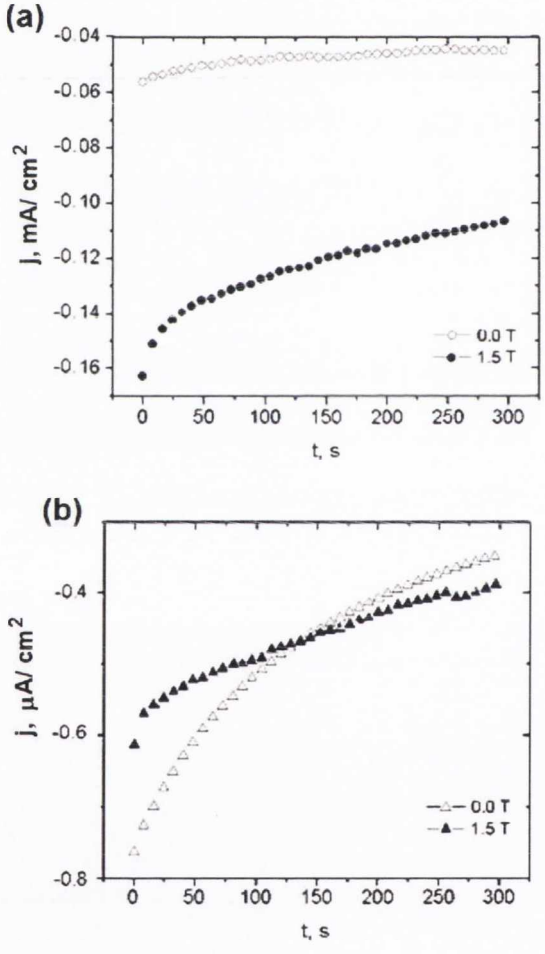

Figure 6.1: Variation on current density during copper electrodeposition at overpotential η = -40 mV, corresponding to the activation control zone for copper reduction, when a field of 1.5 Tesla is applied. Electrolyte corresponds to 0.1 M $CuSO_4$ electrolyte (a) naturally aerated, or (b) argon bubbled.

Fricoteaux observed that certain textures of copper deposits obtained at low j/j_L ratios were changed by convection – either mechanical or magnetically induced. The explanation was related to the presence of oxygen in solution [52]. Following his work, the experiments shown here relate the field effect on the secondary ORR, to the coverage obtained when copper deposits are produced magnetoelectrochemically at low overpotentials.

Copper deposits were grown from a 0.3 M $CuSO_4$, naturally aerated solution at different field intensities from 0 to 4 T, and their thicknesses were measured with a profilometer. Figure 6.2 shows changes in coverage θ and thickness τ as a function of field intensity and direction relative to the Lorentz and natural convection forces. The optical views (magnification 10x) at the right column show that the electrode area recedes with increasing fields, in the direction of the Lorentz force. The horizontal and vertical profiles show that deposit thickness is progressively reduced with increasing field, as follows:

The upper panel shows the profiles in the plane (xy), where magnetoconvection acts along the (x) direction through the Lorentz force, while gravity acts in the (z) direction. Opposite to the case shown in Chapter IV, thickness is inversely proportional to the flux density, i.e. when the field is applied, lower thickness is obtained. Moreover, the edge facing the flow exhibits a bald zone, totally opposite of the previous case where material build-up was seen. Gravity, acting along (z) is not expected to exert any observable effect, nor it does.

Next, gravity-induced convection is taken into account. The profiles in the lower panel correspond to the plane (yz), showing changes of deposit thickness along the direction of natural convection for different field intensities. There is no evidence of an effect of gravity. However, in this case magnetoconvection, acting in the (x) direction, does indeed change the profiles, which recede with the field. The optical views show clearly how the coverage is reduced by the field action. From the profiles

and optical views it is thus clear that inhibition of copper growth was promoted by the magneto-convective flow, because of the ORR.

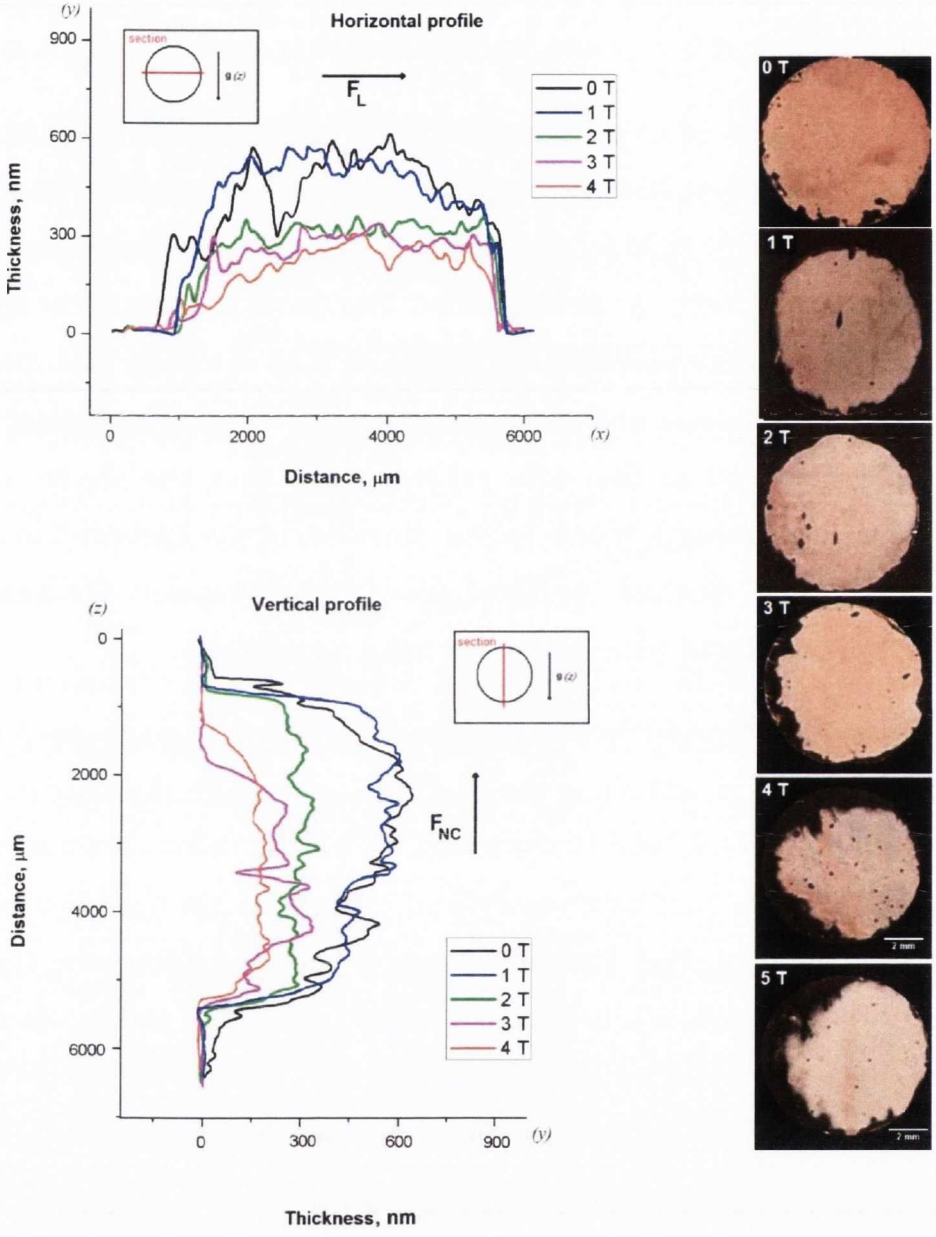

Figure 6.2: Profiles and morphology of samples grown from a 0.3 M $CuSO_4$ electrolyte, at η = -40 mV during 300 seconds, under magnetic fields up to 4 Tesla. The upper panel shows the profiles in the (*yx*) plane, showing the action of the Lorentz force. The lower panel shows the vertical profiles in the (*zy*) plane. Optical views (10x) are shown on the right column.

SEM-EDS characterization was also carried out on thin deposits where pores were formed at η = -40 mV. Figure 6.3 shows that, under no field, sharp copper crystals project into a pore, while smooth edges are formed under a field. According to the concept of tertiary current distribution, crystal projections are typical in stagnant conditions of the electrolyte, where fast growing sites consume preferentially the ions from their surroundings and thus overgrow the adjacent crystals. Following this reasoning, rounded edges indicate a more uniform access of ions towards all the crystals, hence a more homogeneous distribution of species, which may be attributed to the magnetically-induced convection.

The insets of figure 6.3 show area plots of the copper and oxygen presence. The lower panel shows the EDS linear scan indicated by the yellow arrows. No variation of the O:Cu ratio is expected for the area of the pore unless either copper or oxygen content changes at the zone due to the field. Since at the pore the copper content is fixed, corresponding only to the initial substrate, the higher O:Cu ratio obtained at 4 T indicates that the oxygen content increases under magnetic influence in this area.

Of course, the EDS chamber operates in vacuum; hence the oxygen in the sample must be in the form of a copper oxide favoured by enhanced adsorption of reduced oxygen gas from the electrolyte. according to Eq. (1.2). According to the Pourbaix diagram of figure 1.2 in Chapter I, the phase Cu_2O can be formed at such low overpotential in acid solutions from pH 3. This is close to our system's pH.

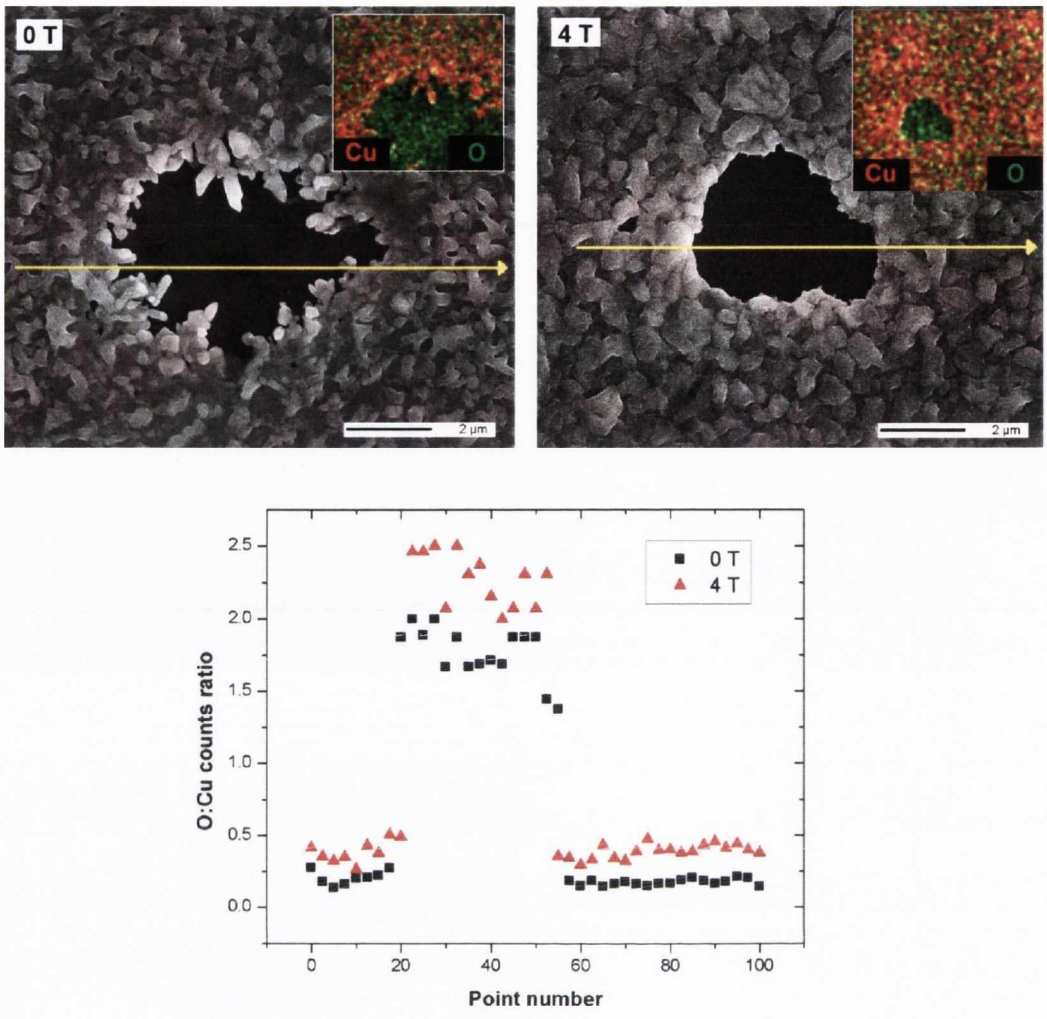

Figure 6.3: SEM images of copper deposits around a pore at 0 and 4 T for deposits grown under activation control at η = -40 mV, showing effect of the field on growth and a higher presence of oxygen when deposition was performed under field. Lower panel: ratio of oxygen to copper counts, along the line scans, indicating that the field increases oxygen content in the sample.

VI.2 Copper and hydrogen

The second side reaction considered in this system corresponds to hydrogen production from protons in water during the cathodic metallization, usually referred as Hydrogen Evolution Reaction (HER). This occurs at high overpotentials, as was shown in Chapter I. An efficient use of current to produce copper deposits requires that secondary reactions involving hydrogen are avoided or suppressed. This is usually achieved by keeping the system below the limiting current, i.e. at $j/j_L < 1$. However, requirements of industrial production call for an increase of this ratio. As the value approaches to 1, geometric configurations may result in localized concentration of current such that, in these areas, $j/j_L > 1$. For the case of copper metallization, that means that hydrogen can, locally, be co-reduced as a secondary reaction.

In this section, the field effect in such conditions is studied. In the first part, the co-reduction is studied without field and then it is analysed with the presence of fields.

VI.2.1.Cu-H co-reduction under no field

The deposit morphology obtained as a result of hydrogen evolution during copper growth was characterized by scanning electron microscopy. Figure 6.4 shows samples grown on copper substrates sputtered on silicon, of 5 mm in diameter, from a 0.3 M $CuSO_4$ solution. The deposits were grown for 25 s at $\eta = -1.0$ V at 0 T. Multiple pores of different sizes are seen in (a) and (b), indicating that bubbles of diverse sizes were produced. Sometimes the solid copper grows around bubble's walls and projects itself, towering into the solution, as seen in (c) where a copper

stockade surrounding a pore is shown. It is evident that hydrogen evolution strongly affects the morphology of deposits.

Figures 6.4 (d) and (e) show, for the same conditions, the cross-section view of copper growth at the walls of pores caused by adjacent hydrogen bubbles. It is seen that the site which was occluded by the bubbles exhibits the flat surface of the initial substrate, indicating that no copper ions had access to that portion of the electrode. This constitutes another aspect avoided by industrial processing. Since bubbles of gas occlude the surface, the electrode reactivity is reduced, and a resistive component of the cell voltage, the IR drop, sets in.

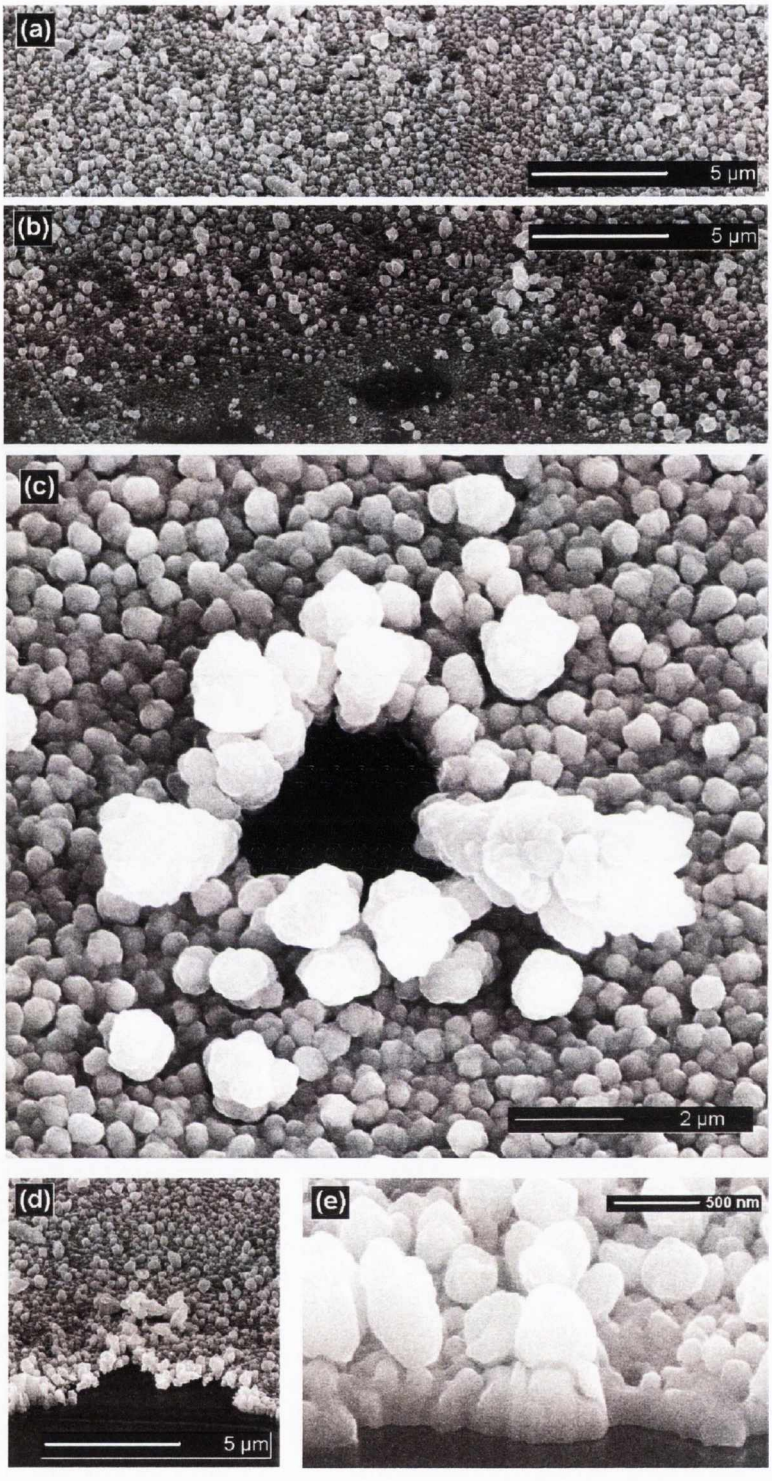

Figure 6.4: Scanning electron microscope images showing copper deposits obtained in co-reduction with hydrogen during 25 seconds, from a 0.3 M $CuSO_4$ solution. No field is applied.

VI.2.2.Cu-H co-reduction under magnetic fields

In this section, the effect of vertical fields up to 5 Tesla is analyzed. The system is controlled in two ways. Firstly forcing it to remain at overpotentials where HER occurs, i.e. $j/j_L > 1$, and secondly, allowing it to change this ratio. This is achieved by applying potentiostatic control in the first case and galvanostatic in the second. The field effect is analyzed in terms of growth mode, current efficiency and roughness.

VI.2.2.1 System forced to maintain $j/j_L > 1$

In this case, potentiostatic control of the system, at η = -1.0 V allowed keeping the current above the mass transport limited current. Figure 6.5 shows SEM images of samples grown at the initial stages of deposition, which illustrates the field effect in growth mode. In figure (a) deposits formed at $j/j_{L1\ (B=0)} > 1$ exhibit typical formations like the copper stockade seen in figure 6.4(c), formed as copper grows around the site where hydrogen bubbles evolve.

When a field is applied in conditions that the system is forced to $j/j_{L2\ (B\neq0)} > 1$, figure 6.5(b), morphology looks smoother. However the grown features of copper and the distribution of pores indicate that hydrogen continues to be produced at a smaller bubble size. Moreover, the shape of copper particles is the same as in figure (a), indicating that no change in copper growth mode is attained. This is consistent with the fact that the overpotential is kept within the HER region, above the limiting value of current density.

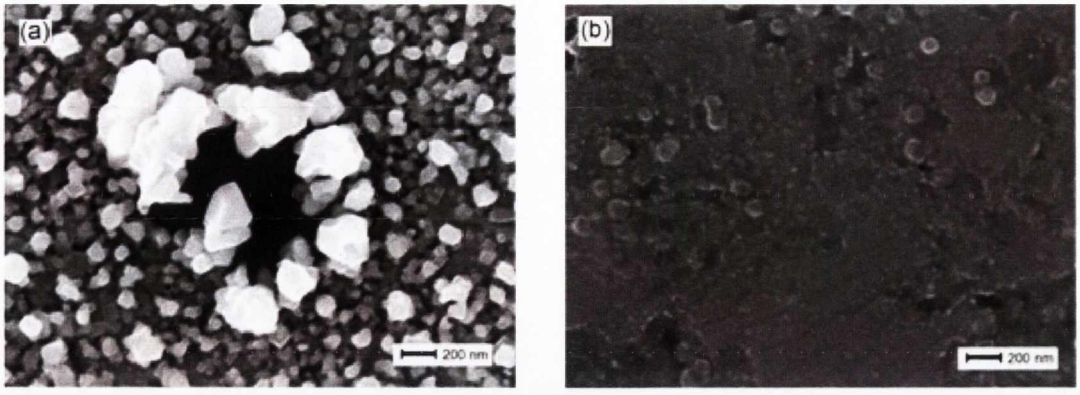

Figure 6.5: Scanning electron microscope images showing the effect of fields in morphology in relation with hydrogen co-reduction with copper for deposits grown during 5 seconds at (a) $j / j_{L1} > 1$, B = 0 T and (b) $j / j_{L2} > 1$, B = 4 T, where $j_{L1} < j_{L2}$.

Figure 6.6 shows SEM images of a sample grown at the same conditions, for 25 seconds, under a 4 T field. The bubble size distribution seen here is quite interesting. The sequence zooms out, starting by showing pores as small as 50 nm, formed when copper simultaneously grew with the hydrogen bubbles. Elongated features correspond to copper growth around two or three bubbles arranged in a row.

In the image, when zooming out to lower magnification, a gradient of thickness reveals a convex shape of the grown deposit. This suggests the volume occupied by a bubble of about 50 μm in diameter. This is three orders of magnitude bigger than the minimum size observed by Matsushima [102] but agrees with observations by Tanaka [103]. Further zoom out makes it clear that several big bubbles were growing at the surface along with copper.

In overall, SEM shows that magnetic fields change the size distribution of hydrogen bubbles and copper particles, in a system forced to produce both hydrogen and copper at $j/j_L > 1$.

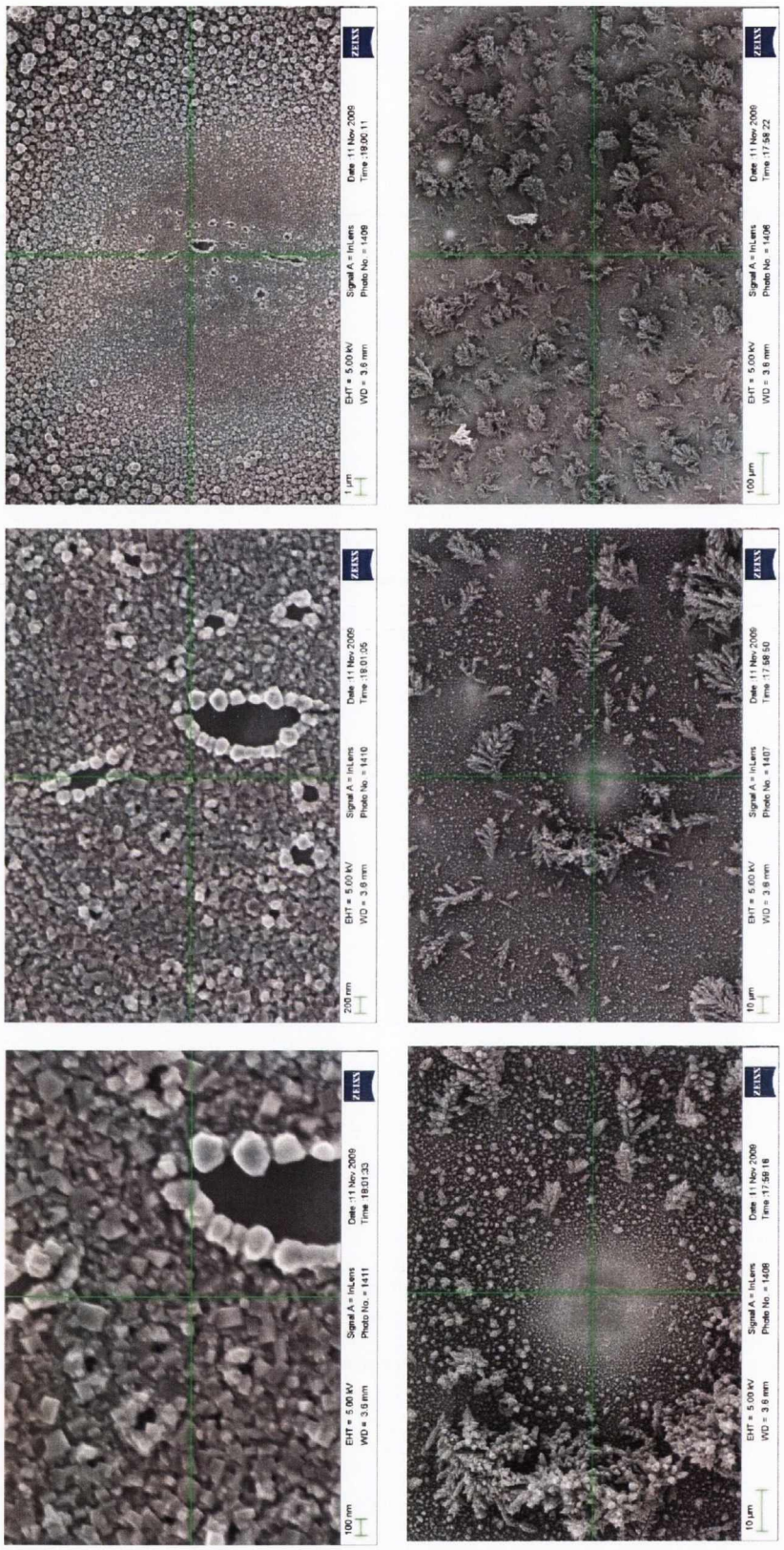

Figure 6.6: Zoom-in of site producing different sizes of hydrogen bubbles. Electrolyte 0.3 M $CuSO_4$, B = 4 T, deposition time: 25 s. Field applied vertically.

An electrochemical quartz crystal microbalance was used to calculate the hydrogen portion of the current used during Cu-H co-reduction, according to Eq. (2.1) in Chapter II [104]. Figure 6.7 shows examples of the effect of a 1.5 T field for the case of potentiostatic deposition at $\eta = -1.0$ V. In (a) and (b) the curves obtained for $\mathbf{B} = 0$ T and $\mathbf{B} = 1.5$ T are shown respectively. It can be seen from the data that the current efficiency of nearly 90% obtained after 15 s at 0 T is reduced to approximately 75% by the applied field, indicating that the field enhances the hydrogen current more than the copper current in potentiostatic conditions where hydrogen evolution reaction occurs.

Quantification of the field effect on the roughness has been addressed via topological (*xyz*) measurements with scanning white light interferometry. Figures 6.8 (a) and (b) show displays of the information obtained from this technique. The system is maintained at $j/j_L > 1$, by applying $\eta = -1.0$ V. In (a) no field is applied, and the corresponding rms roughness is 3 μm; the images clearly show dendritic growth with corresponding variations in height. When a 1.5 T field is applied (b) still in the co-reduction regime, i.e. forcing the system to HER overpotentials and currents above the mass transport limited value, rms roughness decreases to 1.3 μm. This shows that magnetoconvection changes the morphology of growth even for systems where co-reduction of hydrogen gas is forced.

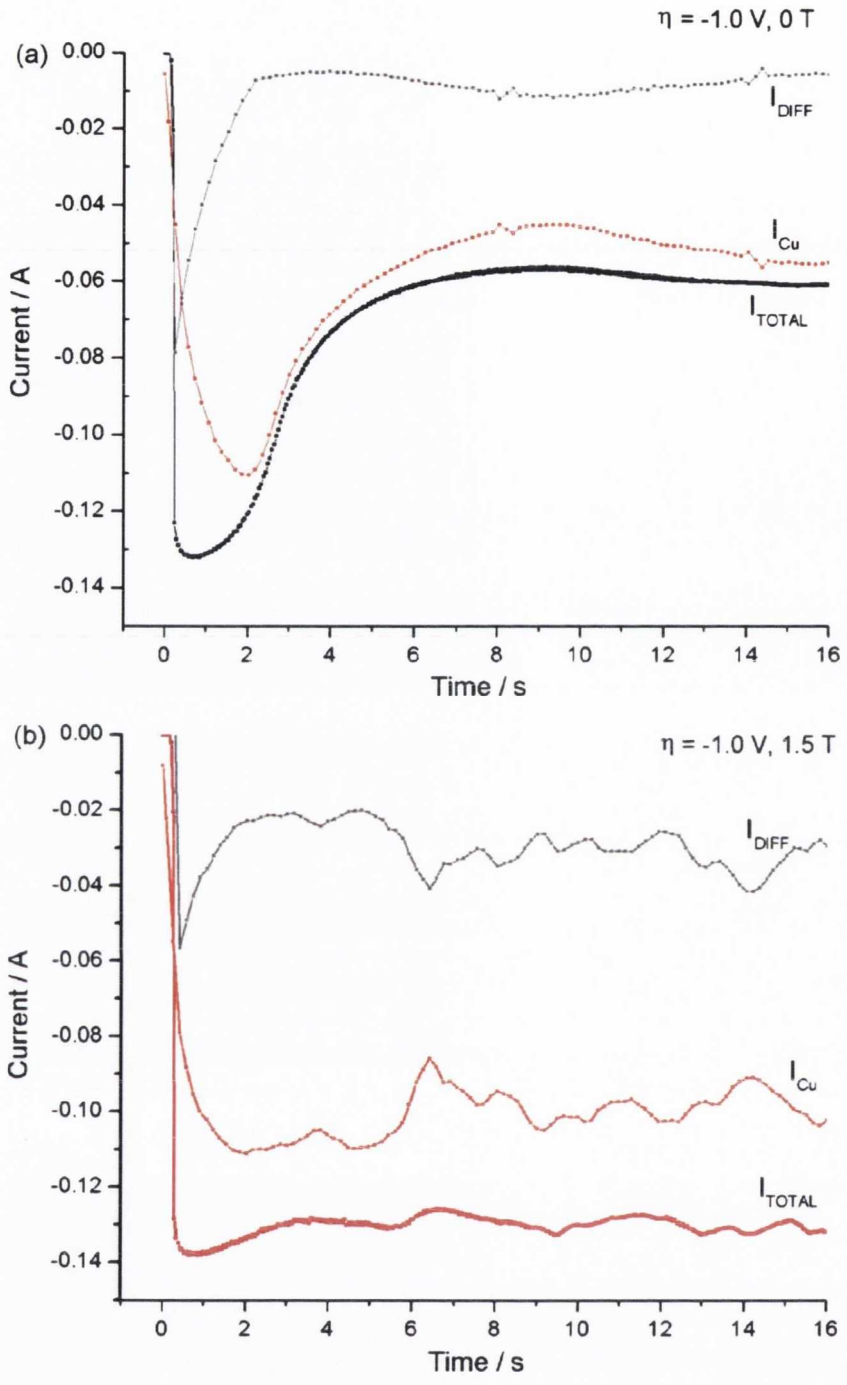

Figure 6.7: Current efficiency calculated from data obtained with an electrical quartz microbalance, for co-reduction of copper and hydrogen at η = 1.0 V, from a 0.3 M $CuSO_4$ solution. (a) 0 T, (b) 1.5 T.

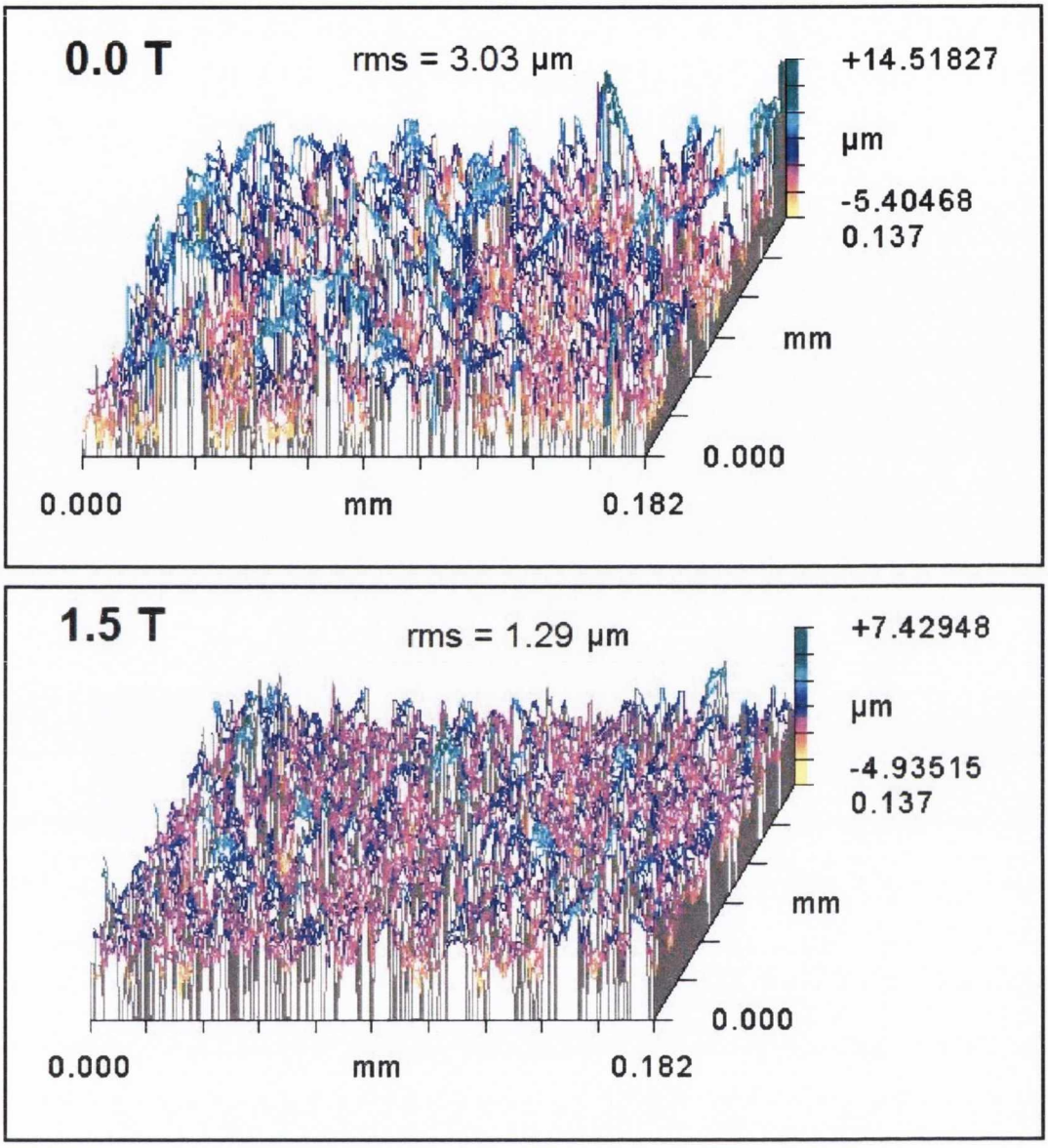

Figure 6.8: Magnetic field effect on roughness, obtained from scanning white light interferometry measurements on samples grown at the co-reduction regime. The system is forced to maintain $j/j_L > 1$.

VI.2.2.2 System changing the j/j_L ratio

When a magnetic field is applied during copper electrodeposition performed galvanostatically at current density values corresponding to hydrogen evolution reaction, the features observed in the deposit change. Figures 6.9(a) and (b) show SEM images of copper deposits obtained at 0 T and 4 T, respectively, after just 5 seconds of growth under galvanostatic conditions with a current density of j = 700 A·m^{-2}. The effect of the field on the morphology is drastic. Under no field, the growth is dendritic, accompanied by hydrogen evolution. When the field is applied the copper deposit exhibits a planar growth and does not project any tips into the solution. Facetted growth features appear as parallel successive steps in the deposit. Clearly, the copper deposit in this case grows differently and any hydrogen evolution is suppressed.

The growth mode shift is consistent with the obtained electrochemical responses. Together with a shift in measured voltage, high frequency sampling of the signals, during chronopotentiometry, shows a clear difference in the distribution of events (peaks) for each voltage range. An example is shown on the time sequences of figure 6.10, where the upper panel shows a typical response at $j/j_{L1\,(B=0)} > 1$ and the lower panel shows a typical response for the system when it shifts to $j/j_{L2\,(B\neq0)} < 1$. In consequence, each noise pattern can be associated with a different mode of growth.

This verifies the expected change in growth mode to a regime where mass transport does not control morphology. This shows that deposits formed when systems are allowed to shift the j/j_L ratio, from $j/j_{L1\,(B=0)} > 1$ to $j/j_{L2\,(B\neq0)} < 1$, changes in morphology are driven by a shift in growth mode.

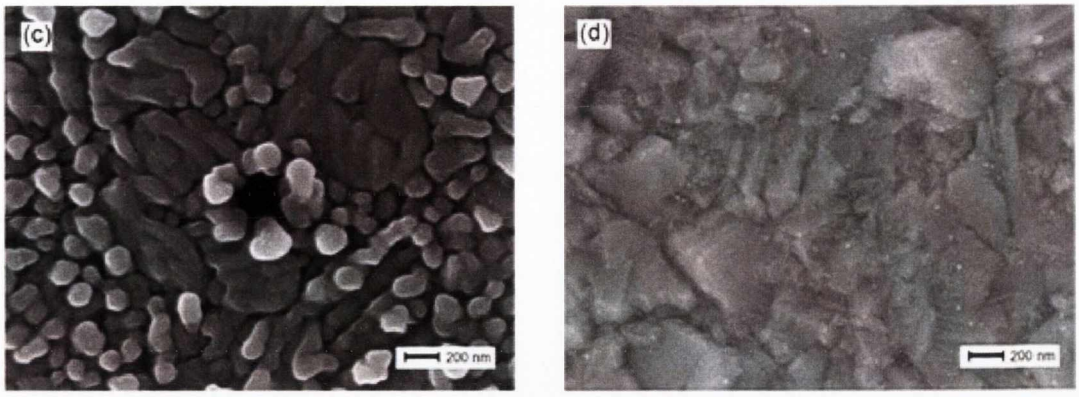

Figure 6.9: Scanning electron microscope images showing the effect of fields in morphology in relation with hydrogen co-reduction with copper. (c) $j/j_{L1\ (B\ =\ 0\ T)} > 1$, and (d) $j/j_{L2\ (B\ =\ 4\ T)} < 1$.

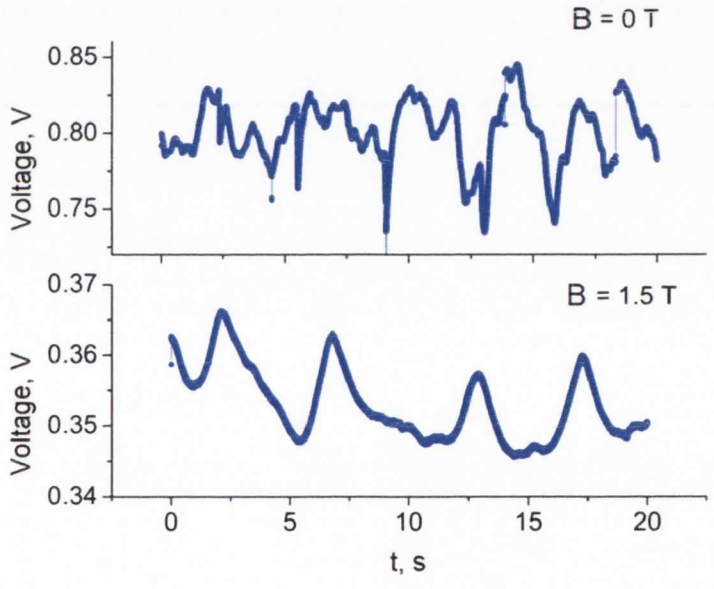

Figure 6.10: Time sequences sampled at high frequency (100 kHz), showing the field effect on voltage and distribution of growth events (peaks) when $j/j_{L1\ (B=0\ T)} > 1$ shifts to $j/j_{L2\ (B=1.5\ T)} < 1$.

The corresponding power spectral density of data shown in figure 6.10 is plotted as a function of frequency in figure 6.11(a). The two orders of magnitude reduction of low-frequency noise under the 1.5 T field is due to the lower overpotential obtained in the galvanostatic mode. The noise now follows a $1/f^{\alpha}$ relation with α larger than 2.

The noise spectra show characteristics which can be related to changes in the growth mode under field. The spectra in 6.11(a) obtained under 1.5 Tesla corresponds – as verified by SEM and voltage shift – to planar growth at overpotentials around 0.3 V, with no hydrogen evolution. The PSD exhibits no plateau or peaks at the low frequency range. This is consistent with the planar growth mode seen at $j/j_L < 1$ in figure 6.9(b). Alternatively, the noise spectrum in zero field corresponding to $j/j_L = 1$ shows an incipient plateau at the lowest frequency, and greater noise, which may be attributed due to dendritic growth and hydrogen bubble release.

In order to make this even clearer, a more extreme situation was chosen. By applying a current equivalent to 20 A cm^{-2} to a 130 μm diameter microelectrode a $j/j_L \sim 500$ was obtained. This certainly secures strong hydrogen production during the experiment, even if the current ratio changes. The effect of Lorentz force direction was also examined for this system.

The results are shown in figure 6.11(b). The low frequency plot in zero field shows a low broad peak around 12 Hz, indicating that hydrogen bubbles are released at roughly this characteristic frequency. When 1.5 T is applied, the signal is flattened, and there is no longer a characteristic frequency for bubble release. Although this is valid whether when $\boldsymbol{F}_L$ acts up or down, the effect is more pronounced when it acts in the same sense as the buoyancy force, $\boldsymbol{F}_U$. The noise spectra show a plateau at low frequencies, resembling the shape associated with hydrogen bubbling found for the copper-free system. However, with copper growing, the extent of the plateau goes up to only about 20 Hz,

one order of magnitude less than that exhibited by the copper-free systems.

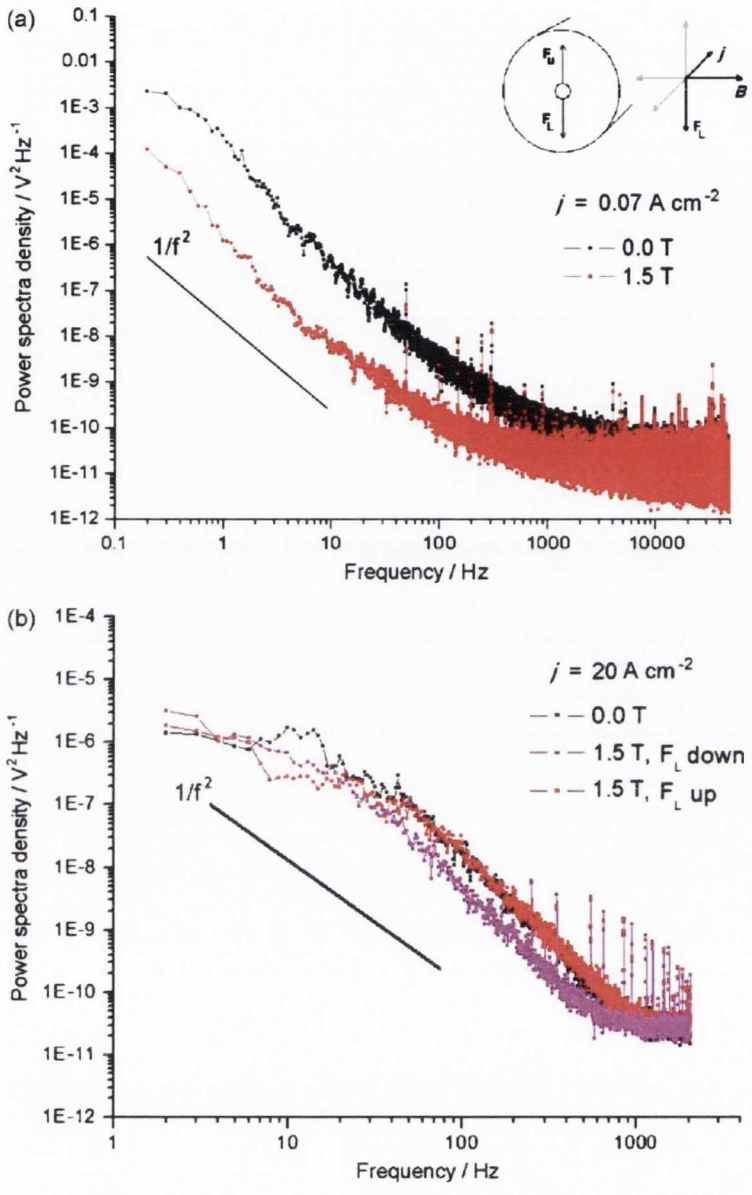

Figure 6.11: Electrochemical noise spectra of the working electrode potential during copper deposition under no field and 1.5 T under galvanostatic control. (a) When hydrogen evolution is suppressed, j = 700 A·m^{-2}, associated with figure 3.51. (b) When strong hydrogen co-reduction is produced at j = 20 Am^{-2}, using a microelectrode. We compare in the graph the effect of $\boldsymbol{F}_L$ orientation. The electrolyte is 0.3 M $CuSO_4$ + 1.2 M H_2SO_4. The black line shows $1/f^2$ slope. Data shown are undersampled to 1000 Hz from the 100 kHz raw data.

An electrochemical quartz crystal microbalance (EQCM) was used to study current efficiency for galvanostatic deposition under fields for a system forced to $j/j_L >> 1$. By applying a very high current, hydrogen production is not suppressed. Figure 6.12 shows a typical example, where copper-hydrogen co-reduction is monitored at different values of applied field.

Panel (a) shows again a shift in cell voltage when fields are applied. In this case, the shift corresponds to approximately 0.4 V. The high overpotential values are an indication that the system is set to produce hydrogen in co-reduction with copper. Panel (b) shows the proportion of the current corresponding to copper and (c) shows the calculated differential current, which is related to hydrogen evolution. Copper deposition improves tenfold, from a quite poor 4 % to 40 %, showing that even for adverse conditions of efficiency, magnetic fields can diminish the parasitic reaction in favour of currents corresponding to the metallization process.

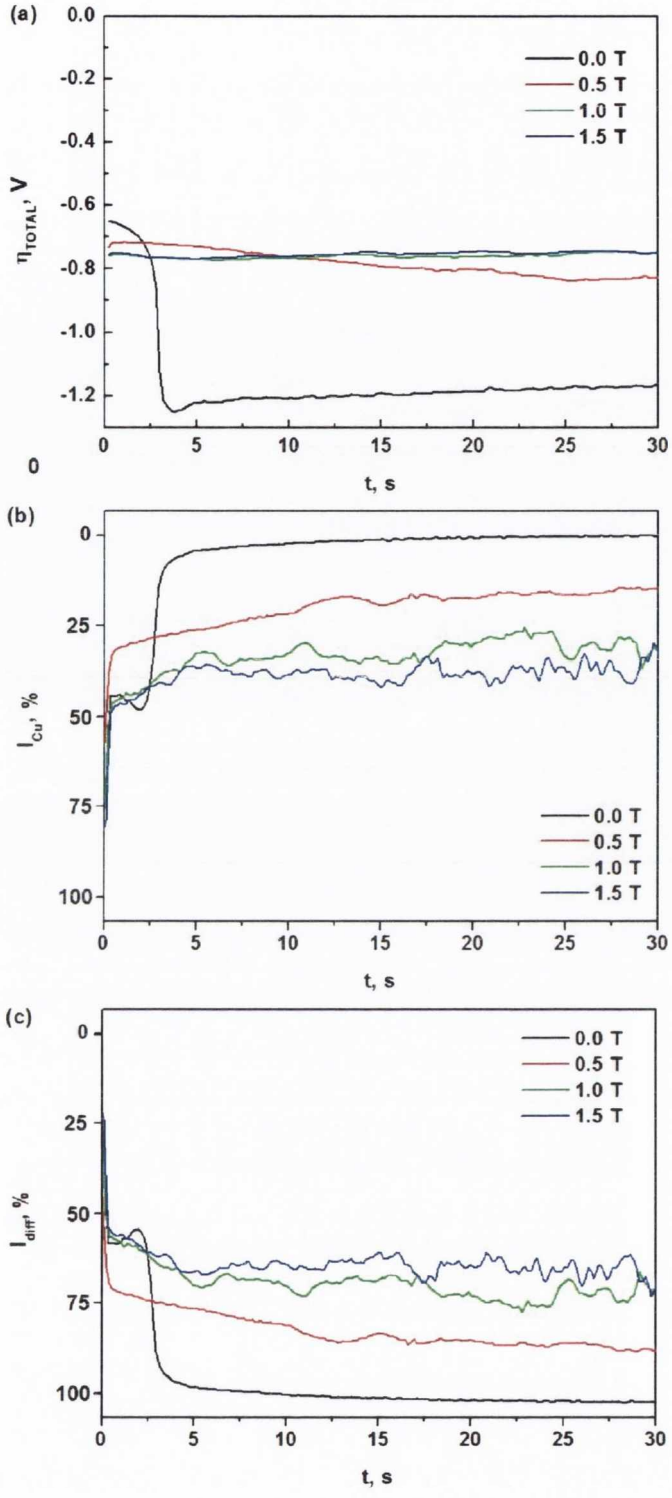

Figure 6.12: Electrochemical quartz crystal microbalance measurements taken for deposition set above the limiting current density. (a) Total change of overpotential, (b) copper current calculated from frequency variations related to changes of deposited mass, and (c) differential current, corresponding to evolved hydrogen gas.

VI.3 Summary

As regards Copper-Oxygen, it was found that cathodic currents are enhanced under field at low overpotentials, at the same time that area coverage and thickness were progressively reduced increasing fields. The receding areas were found aligned with Lorentz force; the zones facing the flow presented less copper deposition. This is opposite to that found in Chapter III where material build-up occurred at the leading edge of the flow.

Convective patterns were identified in this zone from crystals surrounding pores for deposits grown under fields. No such patterns were observed in deposits grown at zero field. The oxygen content, as measured from EDS, was increased under field, indicating that oxygen adsorption was enhanced by the field. The use of deareated solutions confirms that the current is enhanced only on oxygen presence. Since the oxygen reduction reaction is mass-transport limited, then magnetoconvection in this case enhances that reaction, affecting copper coverage at low current densities such as those produced at low overpotentials in the activation zone.

As regards copper-hydrogen, under potentiostatic control it was found that SEM images show that copper growth mode is not changed under field. They show that under field there are still pores attributed to hydrogen bubbles. However these pores are changed in size: Bubbles as small as 50 um were observed, well below values referred to in literature. Also big bubbles were observed, likely due to coalescence processes, as the pore patterns seen from SEM images show. EQCM measurements showed that hydrogen currents were *reduced* under potentiostatic control. Nevertheless, rms roughness values are reduced even for higher proportion of the current corresponding to hydrogen.

At galvanostatic control, SEM shows that the growth mode of copper changes from dendritic to planar.SEM shows that hydrogen evaluation is suppressed. High sampling frequency during chronopotentiometry shows a change of number of "events" (peaks) together with voltage shift, indicating that a change in growth mode occurs. This corresponds with the morphology analysis of Chapter III.

Electrochemical noise analysis with PSD shows that $1/f^{\alpha}$, with $\alpha > 2$, and changes were observed at low frequency range (<100 Hz): an incipient plateau at 0 T but no plateau under field. For very high *j*, where HER still occurs under field a plateau is observed, and a characteristic peak is seen only without fields. The plateaus, if present, extend up to 20 Hz, one order of magnitude less than those observed for a Cu-free solution (~200 Hz)

EQCM measurements at high currents still present a voltage shift towards lower values under fields.

The shift in growth mode and the corresponding EQCM measurements indicate that magnetic fields promote enhancement of deposit quality for systems working at high current densities. This is a key factor for industrial systems where space yield and quality of the product define the operation parameters, balanced by the limitations imposed by mass-transport limitation of the reactions involved. Similar observations have been reported by Popov and co-workers for other types of convection [105, 106].

Chapter VII

Conclusions and further work

VII.1 Conclusions

In this work, the influence of uniform magnetic fields on the cathodic reactions taking place in aqueous acid sulphate and acid copper sulphate systems was studied. The electrochemical conditions chosen for the analysis are based on industrial copper electrowinning and are also general enough to be extrapolated to other industrial settings.

Magnetic fields are known to generate flow during electrochemical reactions, so conditions where mass transport limitation plays a role were chosen. Here it was expected to observe changes due to the field imposition.

Gravity also generates convection, so the interplay between magnetoconvective forces and those due to gravity were considered.

In a first approach, the electrochemical response obtained during magnetoelectrolysis was studied. Potentiodynamic techniques were used for copper concentrations in a wide spectrum covering a 3-order of magnitude range. The field effect in deposition current corresponds to the expected values for solutions up to 0.3 M $CuSO_4$, but a resistive behaviour was observed for higher concentrations. This behaviour is observed only under fields and was overcome by the use of small area electrodes. This suggests that there is a role of the absolute current magnitude involved. Similarly, via potentiostatic techniques, it was found that increases of the real electrode area promoted signal instability.

The analysis of deposits shed light on the role of gravity, concentration and current on the obtained effect. It was seen that growth mode is determined by the overpotential. Hence systems potentiostatically controlled maintain their growth mode with or without field imposition. When the system is kept under mass transport limitation, magnetoconvection enhances morphology within diffusion-limited growth modes. In other words, it changes from dendritic to nodular but remains in 3D growth.

When the system is not 100% diffusion-limited (as in mixed control), the growth mode does not change; however there is evidence of the convective flow on the profile shape.

In aerated systems, where oxygen reduction is a side reaction, its current is enhanced by the fields. If copper currents are comparatively low, then oxygen reduction affects copper growth and area coverage of the deposit.

Galvanostatic growth allows changing the cell overpotential towards much lower values. Shifts around 0.5 V were achieved for fields from 0.5 to 5 T. Power consumption can be reduced from ~2 kWh/kg to 1.4 kWh/kg of produced cathode. Considering that copper production

world-wide yields 15 million tonnes per year, then power saving for this process is certainly economically and environmentally relevant.

Associated with the overpotential shift, a change in growth mode to planar deposits is achieved. Current distribution, inferred from profiles and roughness, is affected by the fields, being more homogeneous as higher is the field intensity. However, there is the chance of a possible decay of the effect on time. Since rough, growing systems naturally increase their area to overcome mass-transport limitation, the field effect changes accordingly. This must be considered and studied further.

In conditions where local concentration of current is high, hydrogen can co-reduce with copper. In such conditions, the hydrogen reaction is affected by the field in different manners depending on the system's ability to change the j/j_L ratio. For galvanostatic conditions, cell overpotential is reduced and hydrogen side reaction is inhibited. This is a relevant aspect regarding industrial applications, since it promises to lower 'yield space' and power consumption for current densities much higher than currently used. It is possible to change from 200-300 $A \cdot m^{-2}$ up to 500 -700 $A \cdot m^{-2}$.

The hydrogen evolution reaction alone also presents an interesting and unexpected behaviour under magnetic fields when microelectrodes are used. The field influences the rate and direction of the evolving bubble stream depending on the field intensity and direction relative to gravity. Also, single bubbles can be produced, with sizes higher or lower than those obtained under no field.

Water containing large amounts of colloidal bubbles can be produced when Lorentz force acts perpendicular to upthrust. There is a similar effect when Lorentz force adds to upthrust. Single hydrogen bubbles as big as 900 μm in diameter can be produced when Lorentz force opposes upthrust. Secondary flow due to vortex around single bubbles stabilize them, allowing control of their size.

Possible applications of these principles are multiple. Enhanced electroflotation and water electrolysis, design of bubble-controlled actuators in microchip systems, as well as corrosion control may be possible by using magnetic devices during hydrogen production. Permanent magnets are a convenient and compact method of producing the chosen fields. Also, these principles may be applied to anodic systems where oxygen bubbles are produced, as is the case of the counter reaction on many types of electrowinning cells.

VII.2 Further work

The analysis outlined in the previous section indicates further areas where the effects found in this work head to.

On scientific grounds, the scaling of current density with electrode size during magnoelectrodeposition is relevant. This deals with real electrode area as well as with high ion concentration. Growing systems under mass-transport conditions are beyond equilibrium conditions and their evolution in time accordingly changes the field effect. This should be studied further, and the analysis of the Stefan problem for growing systems may be applied as a criteria.

The combined field and gravity effect on the gas evolution is clear after this investigation. Their role in promotion or inhibition of coalescence at the nano and micro scale remains to be clarified. This can be done by use of in situ STM (AFM and MFM) techniques.

On the industrial ground, building prototypes which include magnetic devices to control the direction and mode of growth of the reaction product appears as a very interesting pathway for future work.

For the case of copper deposition, the, development of cells with magnetically modified cathodes where power consumption is reduced while making production faster and maintaining good deposit quality will be pursued in the following months, as part of an SFI TIDA project.

For the case of bubble control via magnetoelectrolysis, scaling the laboratory conditions for industrial applications such as water electrolysis and electroflotation is the future step of this work.

References

[1] W.G. Davenport, M. King, M. Schlesinger and A.S. Biswas, *"Extractive metallurgy of copper"*. Pergamon, Netherlands, 2002, 432 pp.

[2] M. Pourbaix, *"Atlas of electrochemical equilibria in aqueous solutions"*. Pergamon Press. England, 1966, 644 pp.

[3] M. Schlesinger and M. Paunovic, *"Fundamentals of electrochemical deposition"*, Wiley Interscience, USA, 1998, 301 pp.

[4] E. Budevski, G. Staikov and W.L. Lorentz, *"Electrochemical phase formation and growth", VCH Publishers*, USA, 1996, 410 pp.

[5] A. Milchev, *"Electrocrystallization. Fundamentals of nucleation and growth"*, Kluwer Academic Press, USA, 2002, 232 pp.

[6] J.O'M. Bockris and G.A. Razumney, *"Fundamental aspects of electrodeposition"*. Plenum Press. USA, 1967, 155 pp.

[7] Southampton Electrochemistry Group. "*Instrumental methods in electrochemistry*". Ellis Horwood, England, 2001. 443 pp.

[8] E. Gileadi, Electrode kinetics for chemists, chemical engineers and material scientists. Wiley-VCH Publishers. USA, 1993, 597 pp.

[9] D. Pletcher and F. Walsh, Industrial electrochemistry, Kluwer, 1990, 676 pp.

[10] R. Winand, "*Contribution to the study of copper electrocrystallization in view of industrial applications - submicroscopic and macroscopic considerations*", Electrochimica Acta 43 (1998) 2925.

[11] R. Winand, "*Electrocrystallization - theory and applications*", Hydrometallurgy 29 (1992) 567.

[12] K. Zheng and D. Zhang, *"Recent progress in alkaline water electrolysis for hydrogen production and applications"*, Progress in Energy and Combustion Science 36 (2010) 307.

[13] H. Vogt, Ö. Aras and R. J. Balzer, *"The limits of the analogy between boiling and gas evolution at electrodes"*, International Journal of Heat and Mass Transfer 47 (2004) 787.

[14] K. Kikuchi, H. Takeda, B. Rabolt, T. Okaya, Z. Ogumi, Y. Saihara and H. Noguchi, *"Hydrogen particles and supersaturation in alkaline water from an Alkali–Ion–Water electrolyzer"*, Journal of Electroanalytical Chemistry 506 (2001) 22.

[15] N. Kanani, *"Electroplating: basic principles, processes and practice"*. Elsevier, 2004, 354 pp.

[16] Romankiw and O'Sullivan, in: P. Rai-Choudhury (Ed.), *"Handbook of microlithography, micromachining and microfabrication"*, vol. I, IEE, London, 1997, pp. 227-237.

[17] W. Schwarzacher, "*Kinetic roughening of electrodeposited films*". Journal of Physics: Condensed Matter 16 (2004) R859.

[18] R.N. O'Brien and K.S.V. Santhanam, *"Magnetic field assisted convection in an electrolyte of nonuniform magnetic susceptibility"*. Journal of Applied Electrochemistry 27 (1997) 573.

[19] S. Kawai, Y. Fukunaka and S. Kida, *"Numerical calculation of transient current densit distribution along vertical plane electrode in $CuSO_4$–H_2SO_4 electrolyte solution"*. Journal of the Electrochemical Society, 157 (2010) F40.

[20] G. Marshall, E. Mocskos F.V. Molina and S. Dengra, *"Three-dimensional nature of ion transport in thin-layer electrodeposition"*, Physical Review E 68 (2003) 021607.

[21] T.R. Ní Mhíocháin, G. Hinds, A. Martin, E. Chang Z.Y., A. Lai, L. Costiner and J.M.D. Coey, *"Influence of magnetic field and gravity on the morphology of zinc fractal electrodeposits"*, Electrochimica Acta 49 (2004) 4813.

[22] R T.Z. Fahidy, *"Magnetoelectrolysis"*, Journal of Applied Electrochemistry 13 (1983) 553.

[23] A. Tacken and L.J.J. Janssen, *"Applications of magnetoelectrolysis"*, Journal of Applied Electrochemistry 25 (1995) 1.

[24] T.Z. Fahidy, *"Characteristics of surfaces produced via magnetoelectrolytic deposition"*, Progress in Surface Science 68 (2001) 155.

[25] G. Hinds and J.M.D. Coey, *"Influence of magnetic forces on electrochemical mass transport"*, Electrochemistry Communications 2001.

[26] J.M.D. Coey, FMF Rhen and P. Dunne, *"The magnetic concentration gradient force—Is it real?"*, Journal of Solid State Electrochemistry 11 (2007) 711.

[27] M.C. Weston, M. D. Gerner and I. Fritsch, *"Magnetic Fields for Fluid Motion"*, Analytical Chemistry 82 (2010) 3411.

[28] G. Mutschke and A. Bund, *"On the 3D character of the magnetohydrodynamic effect during metal electrodeposition in cuboid cells"*, Electrochemistry Communications 10 (2008) 597.

[29] G. Mutschke, A. Hess, A. Bund and J. Fröhlich, *"On the origin of horizontal counter-rotating electrolyte flow during copper magnetoelectrolysis"*, Electrochimica Acta 55 (2010) 1543.

[30] R. Aogaki, R. Morimoto and M. Asanuma, *"Nonequilibrium fluctuations in micro-MHD effects on electrodeposition"*, Journal of Magnetism and Magnetic Materials 322 (2010) 1664.

[31] M. Asanuma, A. Yamada and R. Aogaki, *"Self-Organization Process of Secondary Crystal Nodules from Individual Nuclei in Electrodeposition"*, Japanese Journal of Applied Physics 44 (2005) 5137.

[32] R. Aogaki, K. Fueki, T. Mukaibo, Denki Kagaku 43 (1975) 509.

[33] J.P. Chopart, O. Aaboubi, E. Merienne, A. Olivier and J. Amblard, *"MHD-control on limiting Faradaic currents"*, Energy Conversion and Management, 43 (2002) 365.

[34] S. Legeai, M. Chatelut, O. Vittori, J.P. Chopart and O. Aaboubi, *"Magnetic field influence on mass transport phenomena"* Electrochimica Acta, 50 (2004) 51.

[35] M. Uhlemann, H. Schlörb, K. Msellak and J.P. Chopart, *"Electrochemical deposition of Cu under superimposition of high magnetic fields"*, Journal of the Electrochemical Society, 151 (2004) C598.

[36] P. Fricoteaux, B. Jonvel and J.P. Chopart, *"Magnetic Effect during Copper Electrodeposition: Diffusion Process Considerations"*, Journal of Physical Chemistry B, 107 (2003) 9459.

[37] G. Hinds, F.E. Spada, J.M.D. Coey, T.R. Ní Mhíocháin and M.E.G. Lyons, *"Magnetic Field Effects on Copper Electrolysis"*, Journal of Physical Chemistry B 105 (2001) 9487.

[38] H. Matsushima, A. Bund, W. Plieth, S. Kikuchi and Y. Fukunaka, *"Copper electrodeposition in a magnetic field"*, Electrochimica Acta 53 (2007) 161.

[39] C. O'Reilly, G. Hinds and J.M.D. Coey, *"Effect of a Magnetic Field on Electrodeposition. Chronoamperometry of Ag, Cu, Zn, and Bi"*, Journal of the Electrochemical Society. 148 (2001) C674.

[40] A. Krause, J. Koza, A. Ispas, M. Uhlemann, A. Gebert and A. Bund, *"Magnetic field induced micro-convective phenomena inside the diffusionlayer during the electrodeposition of Co, Ni and Cu"*, Electrochimica Acta 52 (2007) 6338.

[41] K. Tschulik, J. Koza, M. Uhlemann, A. Gebert and L. Schultz, *"Effects of well-defined magnetic field gradients on the electrodeposition of copper and bismuth"*, Electrochemistry Communications. 11 (2009) 2241.

[42] D. Fernández and J.M.D. Coey, *"Inhomogeneous electrodeposition of copper in a magnetic field"*, Electrochemistry Communications. 11 (2009) 379.

[43] H. Matsushima, D. Kiuchi and Y. Fukunaka, *"Measurement of dissolved hydrogen supersaturation during water electrolysis in a magnetic field"*, Electrochimica Acta 54 (2009) 5858.

[44] Z. Diao, P.A. Dunne, G. Zangari and J.M.D. Coey, *"Electrochemical noise analysis of the effects of a magnetic field on cathodic hydrogen evolution"*, Electrochemistry Communications 11 (2009) 740.

[45] H.C. Shin, J. Dong and M. Liu, *"Nanoporous structures prepared by an electrochemical deposition process"*, Adv. Mater. 15 (2003) 1610.

[46] S. Li, R. Furberg, M.S. Toprak, B. Palm and M. Muhammed, *"Nature-inspired boiling enhancement by novel nanostructured macroporous surfaces"*, Advanced Functional Materials 18 (2008) 2215.

[47] W. Huang, M. Wang, J. Zheng and Z. Li, *"Facile fabrication of multifunctional three-dimensional hierarchical porous Gold films via surface rebuilding"*, Journal of Physical Chemistry C 113 (2009) 1800.

[48] A. Bund and A. Ispas, *"Influence of a static magnetic field on nickel electrodeposition studied using an electrochemical quartz crystal microbalance, atomic force microscopy and vibrating sample magnetometry"*, Journal of Electroanalytical Chemistry. 575 (2005) 221.

[49] M. Uhlemann, A. Krause and A. Gebert, *"Effect of a magnetic field on the local pH value in front of the electrode surface during electrodeposition of Co"*, Journal of Electroanalytical Chemistry. 577 (2005) 19.

[50] A. Krause, M. Uhlemann, A. Gebert and L. Schultz, *"The effect of magnetic fields on the electrodeposition of cobalt"*, Electrochimica Acta 49 (2004) 4127.

[51] J. A. Koza, M. Uhlemann, A. Gebert and L. Schultz, *"The effect of magnetic fields on the electrodeposition of CoFe alloys"*, Electrochimica Acta 53 (2008) 5344.

[52] P. Fricoteaux and J. Douglade, *"Texture evolution of electroplated copper under various modes of convection. Effect of dissolved oxygen"*, Journal of Materials Science Letters 21 (2002) 1485.

[53] S.R. Ragsdale and H.S. White, *"Imaging microscopic magneto-hydrodynamic flows"*, Analytical Chemistry 71 (1999) 1923.

[54] S. Huo and W. Schwarzacher, *"Anomalous scaling of the surface width during Cu electrodeposition"*, Physical Review Letters 86 (2001) 256.

[55] M. C. Lafouresse, P. J. Heard, W. Schwarzacher, "*Anomalous Scaling for Thick Electrodeposited Films*", Physical Review Letters 98 (2007) 236101.

[56] K. Zeng, D. Zhang, "*Recent progress in alkaline water electrolysis for hydrogen production and applications*", Progress in Energy and Combustion Science 36 (2010) 307–326

[57] A. Volanschi et al. *"Gas bubbles electrolytically generated at microcavity electrodes used for the measurement of the dynamic surface tension in liquids*", Sensors and Actuators A 52 (1996) 18-22

[58] W. Olthius, A. Volanschi, P. Bergveld, "*Dynamic surface tension measured with an integrated sensor-actuator device using electrolytically generated gas bubbles*". Transducers (1997) 1059.

[59] W. Olthius, A. Volanschi, P. Bergveld, "*Dynamic surface tension measured with an integrated sensor–actuator using electrolytically generated gas bubbles*", Sensors and Actuators B 49 (1998) 126.

[60] S.K.A. Sarkar, G.M. Evans, S.W. Donne, "*Bubble size measurement in electroflotation*", Minerals Engineering 23 (2010) 1058.

[61] J. Eigeldinger, H. Vogt, "*The bubble coverage of gas-evolving electrodes in a flowing electrolyte*", Electrochimica Acta 45 (2000) 4449.

[62] C. Gabrielli, F. Huet, M. Kedam, "*Real time measurement of electrolyte resistance fluctuations*", Journal of the Electrochemical Society., 138 (1991) L82.

[63] H. Vogt, *"On the gas-evolution efficiency of electrodes I – Theoretical"*, Electrochimica Acta 56 (2011) 2404.

[64] H. Vogt, *"On the gas-evolution efficiency of electrodes. II – Numerical analysis"*, Electrochimica Acta 56 (2011) 1409.

[65] C. Gabrielli, F. Huet, R.P. Nogueira, *"Fluctuations of concentration overpotential generated at gas-evolving electrodes*", Electrochimica Acta 50 (2005) 3726.

[66] J. Fransaer, V. Bouet, J.-P. Celis, C. Gabrielli, E Huet, G. Maurin, *"Perturbation of the Flow of Current to a Disk Electrode by an Insulating Sphere*", Journal of the Electrochemical Society, 142 (1995) 4181.

[67] H. Matsushima, D. Kiuchi, Y. Fukunaka, K. Kuribayashi, *"Single bubble growth during water electrolysis under microgravity"*, Electrochemistry Communications 11 (2009) 1721.

[68] J. M. Silva, R. P. Nogueira, L. Miranda, F. Huet, "*Hydrogen Absorption Estimation on Pd Electrodes from Electrochemical Noise Measurements in Single-Compartment Cells*" Journal of the Electrochemical Society, 148 (2001) E241.

[69] K. Kikuchi, H. Takeda, B. Rabolt, T. Okaya, Z. Ogumi, Y. Saihara, H. Noguchi, *"Hydrogen particles and supersaturation in alkaline water from an Alkali–Ion–Water electrolyzer"*, Journal of Electroanalytical Chemistry 506 (2001) 22.

[70] Y. Tanaka, S. Uchinashi, Y. Saihara, K. Kikuchi, T. Okaya, Z. Ogumi, *"Dissolution of hydrogen and the ratio of the dissolved hydrogen content to the produced hydrogen in electrolyzed water using SPE water electrolyzer"*, Electrochimica Acta 48 (2003) 4013.

[71] U. Bertocci,t J. Frydman, C. GabrieIIi, F. Huet, M. Keddam, "*Analysis of Electrochemical Noise by Power Spectral Density Applied to Corrosion Studies*", Journal of the Electrochemical Society, 145 (1998) 2780.

[72] C. Gabrielli, F. Huet, R. P. Nogueira, "*Electrochemical Noise Measurements of Coalescence and Gas-Oscillator Phenomena on Gas-Evolving Electrodes*", Journal of the Electrochemical Society, 149 (2002) E71.

[73] A. Steyer, P. Guenon, D. Beysens, "Coalescence-induced $1/f^2$ noise" Physical Review Letters 68 (1992) 1869.

[74] I. Szenes, G. Meszaros, B. Lengyel, "*Noise study of hydrogen evolution process on Cu and Ag microelectrodes in sulphuric acid solution*", Electrochimica Acta 52 (2007) 4752.

[75] Z. Diao, P.A. Dunne, G. Zangari, J.M.D. Coey, "*Electrochemical noise analysis of the effects of a magnetic field on cathodic hydrogen evolution*", Electrochemistry Communications 11 (2009) 740.

[76] D. Fernández, Z. Diao, P. Dunne, J.M.D. Coey, "*Influence of magnetic field on hydrogen reduction and co-reduction in the Cu/CuSO4 system*", Electrochimica Acta 55 (2010) 8664.

[77] L. Zhang, Y. Zhang, X. Zhang, Z. Li, G. Shen, M. Ye, Ch. Fan, H. Fang, J. Hu, "*Electrochemically Controlled Formation and Growth of Hydrogen Nanobubbles*", Langmuir 22 (2006) 8109.

[78] S. Yang, P. Tsai, E. S. Kooij, A. Prosperetti, H. J. W. Zandvliet and D. Lohse, "*Electrolytically Generated Nanobubbles on Highly Orientated Pyrolytic Graphite Surfaces*", Langmuir 25 (2009) 1466.

[79] M.C. Tavares, S.A.S. Machado, L.H. Mazo, "*Study of hydrogen evolution reaction in acid medium on Pt microelectrodes*", Electrochimica Acta 46 (2001) 4359.

[80] J. K. Nørskov, T. Bligaard, A. Logadottir, J. R. Kitchin, J. G. Chen, S. Pandelov, U. Stimming, "*Trends in the Exchange Current for Hydrogen Evolution*", J. Electrochem. Soc., 152 (2005) J23.

[81] A.J. Prosser, E.I. Franses, "*Adsorption and surface tension of ionic surfactants at the air–water interface: review and evaluation of equilibrium models*", Colloids and Surfaces A: Physicochemical and Engineering Aspects 178 (2001) 1.

[82] T.R. Young, S. R. Grinstead, "*The surface tension of aqueous solutions*", Annals of the New York Academy of Sciences, 51 (1949) 765.

[83] P. Kristof, M. Pritzker, "*Effect of electrolyte composition on the dynamics of hydrogen gas bubble evolution at copper microelectrodes*", Journal of Applied Electrochemistry 27 (1997) 255-265.

[84] N.G. Tsierkezos, I.E. Molinou, *"Thermodynamic properties of water plus ethylene glycol at 283.15, 293.15, 303.15, and 313.15 K"*, Journal of Chemical and Engineering Data 43 (1998) 989.

[85] T.F. Yang, "*The surface tension of aqueous sulphuric acid solutions*" Annals Ney York Academy of Sciences (1962) 765-780.

[86] J. Hanwright, J. Zhou, G. M. Evans, K.P. Galvin, "*Influence of Surfactant on Gas Bubble Stability*", Langmuir 21 (2005) 4912.

[87] J.A. Koza, M. Uhlemann, A. Gebert, L. Schultz, "*Desorption of hydrogen from the electrode surface under influence of an external magnetic field*", Electrochemistry Communications 10 (2008) 1330.

[88] J.A. Koza, S. Mühlenhoff, M. Uhlemann, K. Eckert, A. Gebert, L. Schultz, "*Desorption of hydrogen from an electrode surface under influence of an external magnetic field – In-situ microscopic observations*", Electrochemistry Communications 11 (2009) 425.

[89] F.L. Haan Jr,, P.P. Sarkara, W.A. Gallus, "*Design, construction and performance of a large tornado simulator for wind engineering applications*", Engineering Structures 30 (2008) 1146.

[90] S.L. Huang, H.C. Chen, C.C. Chu, C.C. Chang, "*On the transition process of a swirling vortex generated in a rotating tank*" Experiments in Fluids 45 (2008) 267.

[91] J.A. Koza, S. Mühlenhoff, P. Zabinski, P.A. Nikrityukd, K. Eckert, M. Uhlemann, A. Gebert, T. Weier, L. Schultz, S. Odenbach, "*Hydrogen evolution under the influence of a magnetic field*", Electrochimica Acta 56 (2011) 2665.

[92] N.-T. Nguyen, S. Lassemono, F.A. Chollet, C. Yang, "*Microfluidic sensor for dynamic surface tension measurement*" IEE Proceedings Nanobiotechnology, 153 (2006) 102.

[93] Z. Liu, C. Herman, D. Mewes, "*Visualization of bubble detachment and coalescence under the influence of a nonuniform electric field*", Experimental Thermal and Fluid Science 31 (2006) 151.

[94] T. Iida, H. Matsushima, Y. Fukunaka, "*Water Electrolysis under a Magnetic Field*", Journal of the Electrochemical Society, 154 (2007) E112-E115.

[95] K. Kikuchi, H. Takeda, B. Rabolt, T. Okaya, Z. Ogumi, Y. Saihara, H. Noguchi, "*Hydrogen particles and supersaturation in alkaline water from an Alkali–Ion–Water electrolyzer*", Journal of Electroanalytical Chemistry 506 (2001) 22.

[96] J. Eigeldinger, H. Vogt, "*The bubble coverage of gas-evolving electrodes in a flowing electrolyte*" Electrochimica Acta 45 (2000) 4449.

[97] H. Matsushima, T. Nishida, Y. Konishi, Y. Fukunaka, Y. Ito, K. Kuribayashi, "*Water electrolysis under microgravity Part 1. Experimental technique*", Electrochimica Acta 48 (2003) 4119.

[98] D. Kiuchi, H. Matsushima, Y. Fukunaka, K. Kuribayashi, "*Ohmic Resistance Measurement of Bubble Froth Layer in Water*

Electrolysis under Microgravity", Journal of the Electrochemical Society, 153 (2006) E138.

[99] H. Vogt, O. Aras, R.J. Balzer, "*The limits of the analogy between boiling and gas evolution at electrodes*", International Journal of Heat and Mass Transfer 47 (2004) 787.

[100] H. Matsushima, Y. Fukunaka, K. Kuribayashi, "*Water electrolysis under microgravity Part II. Description of gas bubble evolution phenomena*" Electrochimica Acta 51 (2006) 4190.

[101] M. B. Vukmirovic, N. Vasiljevic, N. Dimitrov and K. Sieradzkia, *"Diffusion-limited current density of oxygen reduction on Copper"*, Journal of the Electrochemical Society, 150 (2003) B10.

[102] H. Matsushima, D. Kiuchi, Y. Fukunaka and K. Kuribayashi, *"Single bubble growth during water electrolysis under microgravity"*, Electrochemistry Communications 11 (2009) 1721.

[103] Y. Tanaka, S. Uchinashi, Y. Saihara, K. Kikuchi, T. Okaya and Z. Ogumi, *"Dissolution of hydrogen and the ratio of the dissolved hydrogen content to the produced hydrogen in electrolyzed water using SPE water electrolyzer"*, Electrochimica Acta 48 (2003) 4013.

[104] C.S. Lu and O. Lewis, *"Investigation of film-thickness determination by oscillating quartz resonators with large mass load"*, Journal of Applied Physics 43 (1972) 4385.

[105] -K.I. Popov, N.D. Nikolic, P.M. Zivkovic, G. Brankovic, "*The effect of the electrode surface roughness at low level of coarseness on the polarization characteristics of electrochemical processes*", Electrochimica Acta 55 (2010) 1919.

[106] N.D. Nikolic, K.I. Popov, Lj.J. Pavlovic, M.G. Pavlovic, "*The effect of hydrogen codeposition on the morphology of copper*

electrodeposits. 1. The concept of effective overpotential', Journal of Electroanalytical Chemistry, 588 (2006) 88.